Model Based Enhancement of an Autonomous System with a Piezoelectric Harvester

zur Erlangung des akademischen Grades eines

DOKTORS DER INGENIEURWISSENSCHAFTEN (DR.-ING.)

der Fakultät für Maschinenbau

der Universität Paderborn

genehmigte

DISSERTATION

von

M.Sc. Waleed Al-Ashtari

aus Bagdad, Irak

Tag des Kolloquiums: 16. September 2013

Referent: Prof. Dr.-Ing. habil. Walter Sextro

Korreferent: Prof. Dr.-Ing. Jörg Wallaschek

Preface

During the preparation of this dissertation at the chair of Mechatronics and Dynamics (MuD) at the University of Paderborn, I had the opportunity to work and interact with many people. For me, meeting them is the most rewarding part of my experience. Because I cannot individually thank each one of them by writing, I will try to acknowledge only the most important persons in the following few words.

Foremost, I would like to express my gratitude to my supervisor Prof. Dr.-Ing. habil. Walter Sextro and my team leader Dr.-Ing. Tobias Hemsel for guidance and support. Their noble spirits and characters make working in MuD full of wonderful experiences. Also, I express my gratitude to Prof. Dr.-Ing. Jörg Wallaschek and Prof. Dr.-Ing. habil. Mirko Schaper for being a part of my examination committee.

My gratitude extends to all my colleagues in MuD, especially Dipl.-Ing. Matthias Hunstig. Their friendship really provided me with many amazing memories that I will never forget.

I am gratefully acknowledging the support of the German Academic Exchange Service (DAAD) and the Iraqi Ministry of Higher Education and Scientific Research (MoHESR) for their support and for giving me the opportunity to achieve my doctorate degree.

I thank my parents who always provide me with the encouragement that I need to succeed in life. I especially thank my wife Zainab, her unwavering love and support over the years has allowed me to pursuit my goals. Thanks to my lovely children Ali, Melak and Hassan who bring the colors to my life and make it full of happiness.

Waleed Al-Ashtari, September 2013

Kurzfassung

„Energy Harvester“ wandeln Umgebungsenergie in nützliche elektrische Energie. Zur Berechnung der elektromechanischen Charakteristik eines piezoelektrischen „Energy Harvesters“ wird ein auf Materialeigenschaften, Geometrie und Randbedingungen basierendes analytisches Modell vorgestellt. Dieses dient als Basis für ein weiteres Modell, welches den Betrieb eines autonomen Systems beschreibt. Die theoretischen Arbeiten werden mit Laborversuchen validiert. Es zeigt sich, dass der piezoelektrische Harvester im eingeschwungenen Zustand durch den Gleichrichtungsvorgang zwei abwechselnde Lastzustände erfährt. Dies führt zu nichtlinearem Verhalten des Harvesters, besonders wenn die angeschlossene Last eine geringe Impedanz hat. Desweiteren zeigen die Ergebnisse, dass ein solches autonomes System effizient arbeitet, wenn es an eine Last mit hoher Impedanz angeschlossen ist und bei einer der Antiresonanzfrequenz des piezoelektrischen Harvesters entsprechenden Frequenz angeregt wird.

Das Modell des autonomen Systems wird auf ein System mit mehreren piezoelektrischen Wandlern erweitert. Zur praktischen Implementierung eines solchen Systems wird eine Technik zur Frequenzeinstellung eingeführt, da die optimalen Betriebsfrequenzen der einzelnen Wandler aufeinander abgestimmt werden müssen. Die Einstellung erfolgt, indem die Entfernung zwischen zwei Permanentmagneten und damit deren Anziehungskraft, welche die Steifigkeit des Harvesters beeinflusst, angepasst wird. Diese Technik zur Frequenzeinstellung wird modelliert und experimentell validiert. Die Ergebnisse zeigen, dass die Frequenzeinstellung mittels Permanentmagneten eine einfache und zugleich effektive Lösung für das Problem der Frequenzanpassung piezoelektrischer „Energy Harvester“ darstellt.

Abstract

Energy harvesters convert ambient energy into useful electrical energy. An analytical model for calculating the electromechanical characteristics of a piezoelectric harvester based on the material properties, geometry and boundary conditions is presented. This model is the basis for a further model which describes the operation of an autonomous system powered by a piezoelectric harvester. This theoretical work is validated by corresponding laboratory experiments. It is found that, in steady-state operation, the piezoelectric harvester experiences two alternating load conditions due to the rectification process. These load conditions make the system behave nonlinearly, especially if the connected electrical load is of low impedance. Furthermore, the results show that such an autonomous system works efficiently if it is connected to a high impedance load and excited at a frequency matching the anti-resonance frequency of the piezoelectric harvester.

The model of an autonomous system is extended to describe a system with multiple piezoelectric transducers. For implementing such a system, the optimum operation frequencies of the individual transducers must be adjusted. Therefore, a frequency tuning method is introduced. The tuning is accomplished by adjusting the distance between two permanent magnets and thus changing the attracting force between them in order to affect the structural stiffness of the harvester. This tuning method is modeled and validated experimentally. The results show that frequency tuning using permanent magnets is a simple and effective solution for the frequency adjustment of piezoelectric energy harvesters.

Liste der Vorveröffentlichungen

Al-Ashtari W., Hunstig M., Hemsel T., Sextro W. [2012] Frequency Tuning of Piezoelectric Energy Harvesters by Magnetic Force. *Smart Materials and Structures* 21: 035019.

Al-Ashtari W., Hunstig M., Hemsel T., Sextro W. [2012] Analytical Determination of Characteristic Frequencies and Equivalent Circuit Parameters of a Piezoelectric Bimorph. *Journal of Intelligent Material Systems and Structures*, 23(1): 15-23.

Al-Ashtari W., Hunstig M., Hemsel T., Sextro W. [2013] Enhanced Energy Harvesting Using Multiple Piezoelectric Elements: Theory and Experiments. *Sensors and Actuators A: Physical*, doi: 10.1016/j.sna.2013.01.008.

Hunstig M., Al-Ashtari W., Hemsel T., Sextro W. [2013] Leistungs- und Bandbreitensteigerung von Energy-Harvesting-Generatoren für energieautarke Systeme. In: 9. Paderborner Workshop Entwurf mechatronischer Systeme Paderborn 18. - 19.4.2013, HNI-Verlagsschriftenreihe, Band 310: 359-372.

Al-Ashtari W., Hunstig M., Hemsel T., Sextro W. [2013] Increasing the Power of Piezoelectric Harvesters by Magnetic Stiffening. *Journal of Intelligent Material Systems and Structures* 24(11): 1332-1342.

Contents

Nomenclature

A_b	Acceleration amplitude of the base excitation
A_i	Cross sectional area of the i^{th} layer of a compound beam
B	Equivalent mechanical damping of a piezoelectric device
B_r	Residual magnetic flux density
$B_y(y_M)$	Magnetic flux density at distance y_M from the magnet surface
C_m	Equivalent capacitance due to the effective stiffness of the piezoelectric device
C_p	Equivalent capacitance of the piezoelectric material
$C_{p,1}$	Equivalent capacitance of a single piezoelectric layer
C_R	Reservoir capacitor
D	Dielectric charge displacement tensor
E	Electrical field strength tensor
E_b	Modulus of elasticity of a beam
E_p	Modulus of elasticity of a piezoelectric layer
E_{poc}	Modulus of elasticity of a piezoelectric layer under open-circuit condition
E_{psc}	Modulus of elasticity of a piezoelectric layer under short-circuit condition
E_{sh}	Modulus of elasticity of the shim layer of the piezoelectric bimorph
$F(t)$	Excitation force
F_M	Magnetic attraction force between two permanent magnets
$F_{Mx}(t)$	Component of the magnetic force F_M in x-direction

$F_{My}(t)$	Component of the magnetic force F_M in y-direction
F_0	Amplitude of the excitation force
I_b	Moment of inertia of a beam
I_i	Moment of inertia of the i^{th} layer of a compound beam
I_{boc}	Moment of inertia of a beam under open-circuit condition
I_p	Moment of inertia of the piezoelectric layer of the bimorph
I_r	Moment of inertia of the reference layer
I_{bsc}	Moment of inertia of a beam under short-circuit condition
I_{Th}	Thevenin's current
K	Equivalent mechanical stiffness of a piezoelectric device
K_F	Equivalent stiffness representing the effect of axial force
K_M	Equivalent stiffness representing the effect of the magnetic stiffening F_M
K_{Mx1}	Equivalent stiffness representing the effect of the component $F_{My}(t)$
K_{Mx2}	Equivalent stiffness representing the effect of the component $F_{Mx}(t)$
K_{boc}	Equivalent stiffness of the a piezoelectric beam under open-circuit condition
K_{bsc}	Equivalent stiffness of a piezoelectric beam under short-circuit condition
L_m	Equivalent inductance due to the effective vibrating mass of the piezoelectric device
M	Total equivalent mass of a piezoelectric device
M_b	Mass of a vibrating beam
M_M	Mass of the permanent magnet attached to the free end of the beam
M_t	Tip mass attached to the free end of the vibrating beam

Q_M	Mechanical quality factor of the piezoelectric device
R_d	Bulk resistance of the diode
R_l	Connected Resistive load
R_{la}	Characteristic load resistance of the piezoelectric harvester (at anti-resonance frequency)
R_{lr}	Characteristic load resistance of the piezoelectric harvester (at resonance frequency)
R_m	Equivalent resistance due to the damping of the piezoelectric device
R_{Th}	Thevenin's resistance
S	Mechanical strain tensor
T	Mechanical stress tensor
U	Generated DC voltage during the transient conduction time interval
U_d	Barrier voltage of a diode
U_{dc}	Output DC voltage
U_i^{dc}	Generated DC voltage of the i^{th} piezoelectric element
U_i	Amplitude of the generated AC voltage of the i^{th} piezoelectric element
U_{max}	Amplitude of the maximum generated DC voltage of the piezoelectric harvester
U_{max}^d	Maximum generated DC voltage of harvester with multiple piezoelectric element directly connected in series
U_{max}^i	Maximum generated DC voltage of harvester with multiple piezoelectric element indirectly connected in series
$U_n(t)$	Net applied voltage into the load including the drops across the diodes
U_{oc}	Amplitude of the generated AC voltage under open-circuit condition
U_p^d	Generated DC voltage of a harvester with multiple piezoelectric elements directly connected in parallel
U_p^i	Generated DC voltage of a harvester with multiple piezoelectric elements indirectly connected in parallel

U_R	Amplitude of the generated AC voltage under resistive load condition
U_r	Magnitude of the ripple voltage
U_s^d	Generated DC voltage of a harvester with multiple piezoelectric elements directly connected in series
U_s^i	Generated DC voltage of a harvester with multiple piezoelectric elements indirectly connected in series
U_{Th}	Thevenin's voltage
U_s	Amplitude of the common generated voltage by each element of a harvester with multiple piezoelectric elements when they all have the same optimal frequency
U_t	Amplitude of the total generated voltage by a harvester with multiple piezoelectric elements
U_0	Amplitude of the generated voltage
X_{oc}	Amplitude of the deflection of the piezoelectric element under-open circuit condition
X_p	Reactance of the piezoelectric element
X_R	Amplitude of the deflection of the piezoelectric element under resistive load condition
$\hat{Y}_{el}(s)$	Electrical admittance of the piezoelectric device
Y_{el}^I	Imaginary part of the electrical admittance $\hat{Y}_{el}(s)$
Y_{el}^R	Real part of the electrical admittance $\hat{Y}_{el}(s)$
$\hat{Y}_m(s)$	Mechanical admittance of the piezoelectric device
Y_m^I	Imaginary part of the mechanical admittance $\hat{Y}_m(s)$
Y_m^R	Real part of the mechanical admittance $\hat{Y}_m(s)$
$a_b(t)$	Excitation acceleration of the base of the piezoelectric device
c	Empirical corrective exponent
$\mathbf{d}$	Charge constants tensor (direct effect)

d_{31}	Charge constants for a piezoelectric element operating in 31-mode
$\mathbf{d}_t$	Charge constants tensor (inverse effect)
f	Frequency of the excitation
$f(y_M)$	Empirical function describing the decay of the magnetic force F_M
f_a	Anti-Resonance frequency of the piezoelectric device
f_b	Natural frequency of the of the piezoelectric device
f_h	Frequency at which the harvester generates half the peak generated DC voltage
f_m	Frequency at which the piezoelectric device reaches maximum admittance
f_n	Frequency at which the piezoelectric device reaches minimum admittance
f_p	Parallel resonance frequency of the piezoelectric device
f_r	Resonance frequency of the piezoelectric device
f_s	Series resonance frequency of the piezoelectric device
$f_1$and f_2	Frequencies at which the maximum magnitude of the electrical admittance $\hat{Y}_{el}(s)$ decreases by 3db
h	Total thickness of the compound beam
h_i	Thickness of i^{th} layer of the compound beam
h_M	Thickness of the magnet
h_p	Thickness of the piezoelectric layer of the bimorph beam
h_{sh}	Thickness of the shim layer of the bimorph beam
i_d	Current across a diode
$i_u(t)$	Current due to applying external voltage
k_{31}	Electromechanical coupling coefficient of the piezoelectric material operating in 31-mode

l	Length of the vibrating beam
l_M	Length of the magnet
l_p	Length of the piezoelectric layer of the bimorph beam
n	Number of the piezoelectric elements used to construct a harvester
p	Number of the layers of a compound beam
$q(t)$	Generated electrical charge of a piezoelectric device
$q_{ch}(t)$	Electrical charge during the charging of the reservoir capacitor
$q_{dis}(t)$	Electrical charge during the discharging of the reservoir capacitor
$q_R(t)$	Generated electrical charge of a piezoelectric device under resistive load condition
r_{el}	Radius of the circle representing the frequency response of the electrical admittance $\hat{Y}_{el}(s)$ in the complex plane
r_m	Radius of the circle representing the frequency response of the mechanical admittance $\hat{Y}_m(s)$ in the complex plane
s	Laplace variable
s_{11}^D	Compliance of a piezoelectric material operating under open circuit condition in 31-mode
$\mathbf{s}^{\boldsymbol{E}}$	Compliance tensor under short-circuit condition
s_{11}^E	Compliance of a piezoelectric material operating under short-circuit condition in 31-mode
t	Time
t_{ch}	Charging time constant of the reservoir capacitor
t_{dis}	Discharging time constant of the reservoir capacitor
t_{op}	Open-circuit time interval of the piezoelectric harvester
t_p	Period of the vibration of the piezoelectric harvester
t_{ss}	Steady-state conduction time interval of the piezoelectric harvester

t_{tr}	Transient conduction time interval of the piezoelectric harvester
t_0	Dead zone time interval of the piezoelectric harvester
$u(t)$	Generated AC voltage of the piezoelectric harvester
$u_i(t)$	Generated AC voltage of the i^{th} piezoelectric element
$u_{max}(t)$	Maximum generated AC voltage of a harvester with multiple piezoelectric elements
$u_{oc}(t)$	Generated AC voltage of a piezoelectric harvester under open-circuit condition
$u_R(t)$	Generated AC voltage of a piezoelectric harvester under resistive load condition
$u_s(t)$	Common generated AC voltage by each element of a harvester with multiple piezoelectric elements when they all have the same optimal frequency
$u_t(t)$	Total generated voltage by a harvester with multiple piezoelectric elements
w	Width of the bimorph beam
w_e	Equivalent width of the shim layer of the bimorph beam
w_M	Width of the magnet
$x(t)$	Displacement of the equivalent mass M
$x_b(t)$	Excitation displacement at the cantilever base
x_i	Distance between the centroid of i^{th} layer and the centroid of the reference layer in a compound beam
$x_R(t)$	Displacement of the piezoelectric harvester under resistive load condition
$x_t(t)$	Displacement of the piezoelectric harvester at its free end (cantilever)
$x_u(t)$	Displacement of the equivalent mass M under applying external voltage
y_M	Separation distance between the two permanent magnets

y_{min}	Minimal separation distance y_M below which the vibrational mode shape of the harvester is changed due to the magnetic force effect
y_0	Empirical constant
α	Conversion factor between the mechanical and electrical domains of a piezoelectric device
β_1, β_2 and β_f	Constants
$\boldsymbol{\varepsilon^T}$	Tensor of the Permittivity of the piezoelectric material under constant stress condition
ε_{33}^T	Permittivity of a piezoelectric material operating under constant condition in 31-mode
ζ	Equivalent damping ratio of the piezoelectric device
θ	Angle of magnetic force vector with respect to the horizontal axis
ρ_p	Density of the piezoelectric layer of the bimorph beam
ρ_{sh}	Density of the shim layer of the bimorph beam
φ_i	Phase difference between the excitation force $F(t)$ and the generated AC voltage by the i^{th} piezoelectric element
φ_s	Phase difference of the common generated AC voltage by each element of a harvester with multiple piezoelectric elements when they all have the same optimal frequency
φ_t	Phase difference of the total generated AC voltage of a harvester with multiple piezoelectric elements
$\varphi_{u_{oc}}$	Phase difference between the excitation force $F(t)$ and the generated voltage under open-circuit condition $u_{oc}(t)$
φ_{u_R}	Phase difference between the excitation force and the generated voltage under resistive load condition
$\varphi_{x_{oc}}$	Phase difference between the excitation force $F(t)$ and the deflection under open-circuit condition $u_R(t)$

φ_{x_R}	Phase difference between the excitation force $F(t)$ and the deflection under resistive load condition $x_R(t)$
ω	Angular frequency of the excitation
ω_a	Angular anti-resonance frequency of the piezoelectric device
$\omega_{oc,opt}$	Optimal angular frequency of the piezoelectric harvester under open-circuit condition
ω_{oc}	Angular natural frequency of the piezoelectric device under open-circuit condition
$\omega_{R,opt}$	Optimal angular frequency of the piezoelectric harvester under resistive load condition
ω_r	Angular resonance frequency of the piezoelectric device
$\omega_{r,ax}$	Angular resonance frequency of a beam under applying an axial load
ω_{sc}	Angular natural frequency of the piezoelectric device under short-circuit condition

1 Introduction

Energy harvesting, or scavenging, are terms that commonly refer to the process of converting the available energy from the environment into electrical energy. The concept can be found in many real-life applications and on different scales. For example, wind turbines and solar panels are used for high amounts of energy conversion, and solar cells or piezoelectric harvesters are used for low amounts of electrical energy conversion.

The new challenge that has interested engineers since about a decade ago is how to exploit energy harvesting to design systems which have the ability to perform a task and, in addition, power themselves from the available types of ambient energy. Such systems are called autonomous systems, also known as stand-alone systems.

In the next few years, autonomous systems will pervade society and they will find their ways into different areas of application in health, security, comfort and entertainment. This is because such systems can reduce much of the cost, effort and pollution accompanying existing system operations. For example, Rabaey et al. [2000] has studied the feasibility of replacing the existing remote sensor networks, used to control and monitor the security, temperature, lighting, airflow etc. of large buildings, with autonomous systems. It has been concluded that this replacement can reduce the energy consumed by two quadrillion BTUs (approximately 2110×10^{15} joules) in the US alone. This can save roughly 55 billion dollars per year and reduce the emitted carbon by about 35 million metric tons. In this study, it has been stated as well that using autonomous systems can save the cost of wire installation, which costs on average 200 dollars for each of such sensors.

An autonomous system typically includes four components: energy harvester, power management, energy storage and electronic device (e.g. temperature sensor). The design and characteristics of each of these components depend on the type of the ambient energy and the characteristics of the other components.

Here, it is focused on studying autonomous systems with piezoelectric energy harvesters. Such systems typically contain three components in addition to the piezoelectric energy harvester: a full-wave rectifier, a reservoir capacitor and an electronic device which performs the primary task of the autonomous system. Therefore, analyzing and modeling each of these components are the primary objectives.

1.1 Motivation

It is concluded nowadays from the contributions related to autonomous system design and development that the modeling of the piezoelectric harvester is the essential step to develop and enhance the performance of such a system. A better understanding of the influence of material properties, geometrical design and the influence of the other components of the autonomous system on the generated voltage of the piezoelectric harvester helps in developing more efficient systems. Most of the existing models assume that the generated voltage has a harmonic shape. This assumption is valid only under certain electrical conditions. The electrical conditions depend on the architecture and operation of the circuit which is connected to the piezoelectric harvester. Generally, the literature on piezoelectric energy harvesting seldomly shows a clear analysis of the influence of these electrical conditions on the generated voltage of the piezoelectric harvester.

It also can be determined from literature that a major limitation of a piezoelectric harvester is that it only operates effectively at a single excitation frequency. This excitation frequency must match the optimal frequency of the piezoelectric harvester, which is defined as the frequency at which the harvester generates the maximum voltage. It is given by the electromechanical characteristics of the piezoelectric harvester and the electrical conditions. This optimal frequency might be changed due to manufacturing tolerances of the piezoelectric element or even due to operating conditions such as temperature or vibration amplitude. As well, ambient vibration may show fluctuation in frequency. Therefore, piezoelectric harvesters with tunable optimal frequency or being able to generate usable voltage across a range of exciting frequencies are required to make this technology commercially viable.

Generally, designing a harvester with multiple piezoelectric elements is one of the best techniques for expanding the harvester bandwidth or increasing its output voltage. Unfortunately, most of these harvesters are hard to implement in industrial applications. Each of these harvesters requires very accurate manufacturing processes and careful handling, and operates within an invariable range of excitation frequencies. If the frequency spectrum of the host changes, for example due to wear or changed operating conditions, then the previously used harvester can be useless.

1.2 Objectives

In order to give useful theoretical and experimental insight into understanding the operation of autonomous systems with piezoelectric harvesters, it is necessary to propose a system which includes only the basic components. These components are essential to convert the vibrational energy into a useful electrical energy in order to perform the main task of the autonomous system. This system is called as “Basic Autonomous System” (BAS) and it contains, in addition to the piezoelectric harvester, three other elements: a standard full-wave rectifier, a reservoir capacitor and a resistive load.

The aim here is to analyze and model the BAS in order to enhance its performance. Therefore, the following objectives are:

1. Modeling the characteristics of a piezoelectric harvester:
    - mechanical and electrical characteristics
    - structural deflection and corresponding generated voltage.
2. Addressing the effect of electrical conditions on the characteristics of the harvester:
    - effect of the rectification process
    - effect of the reservoir capacitor and connected load.
3. Modeling the harvester with multiple piezoelectric elements:
    - parallel and the series connections of the piezoelectric elements
    - frequency tuning scenarios required for desirable operation.

4. Designing a frequency tuning method based on using the magnetic attraction force between two permanent magnets:
    - modeling the tuning technique
    - determining the effect of the magnetic force on the harvester operation.
5. Using the frequency tuning method to design a harvester with multiple piezoelectric elements
    - setup for voltage increase
    - setup for frequency bandwidth expanding.

1.3 Outline

The chapters are arranged consequently in a way that each chapter builds upon the previous one. They contain state of the art, modeling, development, discussion and conclusion related to the autonomous systems which include piezoelectric harvesters.

Chapter 2 presents topics related to autonomous systems with piezoelectric harvesters. It provides a literature survey of current work related to the designs and the developments of such systems.

The next three chapters deal with systems containing multiple elements with different characteristics. Therefore, each chapter contains its own theoretical and experimental basis in order to eliminate conflict due to variation in the analytical approaches and implemented experimental setups used.

Chapter 3 introduces a model for calculating the mechanical and electrical characteristics of a piezoelectric device based on material properties, geometry and boundary conditions (mechanical and electrical). This chapter also contains experimental data that show the high accuracy of the derived model.

Chapter 4 introduces a comprehensive overview of the operational principle of the BAS. The model describing the operation of the BAS is derived. This theoretical work is supported by the corresponding experimental results.

Chapter 5 discusses the operation of a BAS including a harvester with multiple piezoelectric elements. Operational scenarios to achieve increased voltage or expanding bandwidth are given. As a practical requirement for implementing such a system, a frequency tuning method is introduced. The tuning is accomplished by adjusting the distance between two permanent magnets and thus changing the attracting force between them in order to affect the structural stiffness of the harvester. This tuning method is modeled in order to address the effect of the magnetic forces on the mode shape of the piezoelectric element. Finally, experimental results validate the model and prove the advantage of using multiple piezoelectric elements.

Chapter 6 summarizes the covered topics here and gives conclusions which can be used for future works related to the autonomous systems with piezoelectric harvesters

2 State of the Art

This chapter reviews current concepts of state-of-the-art autonomous systems. It introduces the typical configuration, the principle of operation and the key challenges of such systems.

In the last few years, the piezoelectric harvester has received the most attention as a power source for autonomous system; numerous related scientific journals and conferences have investigated this subject intensively. Most of those works are focused on enhancing the performance of such harvester and overcoming its inherent drawbacks which limit the amount of the generated voltage.

This chapter is arranged to give a brief overview of the piezoelectric devices, starting with the basis of piezoelectricity, via a discussion of the electromechanical characteristics and the equivalent systems of the piezoelectric devices and ending with a revision of most of the significant literature related to autonomous systems with piezoelectric harvesters.

2.1 Typical Autonomous Systems

An autonomous system is defined as that system which fulfills its task and power itself from the available ambient energy. A block diagram representing the general components of a typical autonomous system is shown in Figure 2-1. The design and characteristics of each of these components depend on the type of the ambient energy and the characteristics of the other components. In general, the harvester converts ambient energy into electrical energy, which is characterized by the voltage and current. Energy management components are required to manipulate these voltages and currents either to directly power the electronic device or to store energy for a certain period of time, depending on the nature of the ambient energy and the operation of the electronic device.

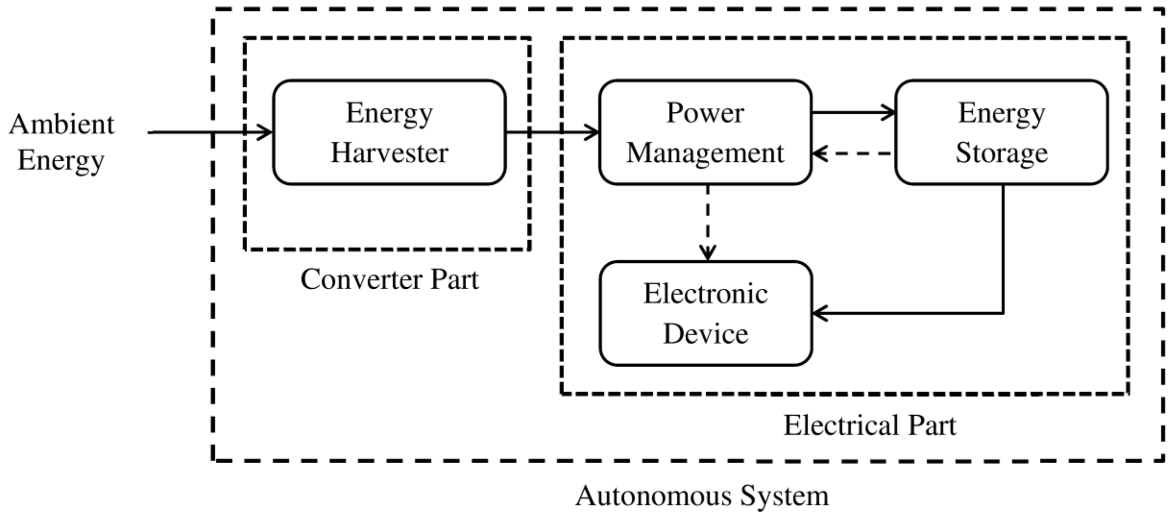

Figure 2-1 Typical block diagram of an autonomous system

The storage component is required when the ambient energy has a variable magnitude or other variable characteristics. For example, in outdoor solar energy harvesting, the sunlight orientation and the clarity of the sky have significant effects on the magnitude of the energy harvested throughout the day. In the case of energy harvesting using piezoelectric elements, not only the vibration energy magnitude but also the frequency of the vibration has an effect on the converted energy.

Also, the need for storage components is determined by the mode of operation of the electronic device. In real applications, the most commonly used mode for wireless sensor operation is based on long standby times; the sensor is waken up for a certain amount of time in order to sample data, to process and transmit it, and then go back to sleep again.

It should be observed that the components of the autonomous system can be categorized into two parts according to their characteristics: the converter part and the electrical part (as shown in Figure 2-1). The converter part can have a wide variety of characteristics based on the type of ambient energy that is captured to be converted into electrical energy, such as electromechanical, thermoelectric or photoelectric characteristics. While the electrical part can have any architecture related to the application requirement and designer preferences.

2.1.1 Types of Ambient Energy

There are many types of ambient energy which can be exploited to power electronic applications by using the proper type of energy harvester. Throughout the literature, descriptions can be found of energy harvesters where vibrations, solar and thermal energies have been used effectively to power autonomous systems because these types of energy can be easily captured in relatively large power densities. Table 2-1 shows comparisons between the electrical energy gained per day by using different harvesters and ambient energies [Ó. Mathúna et al. 2008].

Table 2-1 Typical data for various energy harvesting sources [Ó. Mathúna et al. 2008]

Ambient Energy Type	Input Conditions	Power Density	Area or Volume	Electrical Energy per Day
Mechanical Vibration	Input acceleration is 1.0 m/s^2	100 $\mu W/cm^3$	1 cm^3	8.64 J (continuous vibration)
Solar	Outdoors (illumination level is 500 W/m^2)	7500 $\mu W/cm^2$	1 cm^2	324.00 J (light is available for 50 % of the time)
Solar	Indoors (illumination level is 10 W/m^2)	100 $\mu W/cm^2$	1 cm^2	4.32 J (light is available for 50 % of the time)
Thermal	Temperature difference is 5°C	60 $\mu W/cm^2$	1 cm^2	2.59 J (heat is available for 50 % of the time)

Table 2-1 shows that the electrical energy gained from solar harvesters under outdoor conditions is much higher than those gained by the other harvesters; unfortunately, Table 2-1 also indicates that the same harvester at indoor conditions will harvest 98.67 % energy less than that harvested at outdoor conditions. Therefore, solar energy harvesters are not ideal for powering indoor or implanted sensors.

Ambient vibration energy, also known as ambient kinetic energy in many of the literature, has advantages over other ambient energies in that it can be found almost everywhere with different characteristics and on different scales. In addition Table 2-1 shows that the vibrational energy can be converted into electrical energy with good efficiency. These reasons cause that most of the researches related to the autonomous system topic preferring this energy to be the source for powering their systems. Table 2-2 shows the acceleration and frequency for some representative excitation sources available in our environment. The table shows that the excitation accelerations nominally range from 0.2 $\mathrm{m/s^2}$ to 12.0 $\mathrm{m/s^2}$, while the frequencies range from 1 Hz to 200 Hz.

Table 2-2 Acceleration and frequency for some representative excitation sources available in our environment [Cook-Chennault et al. 2008]

Vibration source	Frequency [Hz]	Amplitude $[\mathrm{m/s^2}]$
Person taping their heel	1	3.0
Car instrument panel	13	3.0
HVAC vents in office building	60	0.2 – 1.5
Base of 3-axis machine tool	70	10.0
CD on notebook computer	75	0.6
Windows next to a busy road	100	0.7
Second story floor of busy office	100	0.2
Blender casing	121	6.4
Clothes dryer	121	3.5
Small microwave oven	121	2.5
Door frame just after door closes	125	3.0
Car engine compartment	200	12.0

2.1.2 Energy Harvesters

An energy harvester is a transducer consisting of a special material that has the ability to convert ambient energy (vibration, solar, thermal, etc.) into purely electrical energy for powering an electronic device. Examples of such materials are piezoelectric, photoelectric and thermoelectric materials.

Ó. Mathúna et al. [2008] have shown that using batteries to power a wireless sensor node is not feasible nowadays. In this study, typical wireless sensor nodes, which have low energy consumption and long periods in sleep mode, were used. The study claims that, in many cases, the self-discharge rate of the battery in sleep mode exceeded the power expenditure from system consumption. As an alternative, the use of rechargeable batteries has been suggested. The lifetimes of such batteries are measured in charge cycles; however, it has been found that if a battery which recharges using a solar cell is used, and a charge cycle is completed in a day, then the life of the battery cannot exceed 18 months because most commercially available batteries will only operate for ca. 300-500 charge cycles. In addition, the service life of the battery is strongly affected by variations in ambient temperature, and in most cases, battery replacement costs time and money. Replacement is frequently difficult to accomplish, especially when the batteries are located in places which have no possibility of access, such as implanted medical devices.

As stated previously, the ambient vibration energy is the best source for obtaining the required electrical energy to power an autonomous system. Generally, vibration energy is easy to capture and there are three basic transductions to convert it into electrical energy [Williams and Yates, 1996]. These transductions are electromagnetic, electrostatic and piezoelectric. In the last few years, piezoelectric transduction has received the most attention regarding its potential to power electronic circuits.

Priya [2007] stated that the energy density of piezoelectric transduction is three times higher than the other two types of transduction. Therefore, designing a piezoelectric harvester as a power source for the proposed autonomous system is the best choice, as it has higher energy conversion than the alternatives.

2.2 Piezoelectric Devices

Piezoelectric devices are devices which utilize piezoelectric materials to convert mechanical deformation into electrical charge or vice versa. These devices are classified in three main categories: sensors, actuators and harvesters. Generally, sensors and actuators have different operation principles and tasks; sensors and harvesters have the same operation principles, but with different tasks, i.e. both sensors and harvesters convert mechanical energy into electrical energy, but the former is used for sensing or measuring purposes while the latter is used for powering electronic devices.

Piezoelectric material has the ability to produce an electric charge when subjected to a mechanical stress (direct piezoelectric effect); inversely, it is also able to convert an applied electric field into mechanical deformation (inverse piezoelectric effect).

The direct piezoelectric effect was discovered in 1880 by the brothers Curie, Pierre and Jacques. The brothers noticed that when tourmaline or quartz crystal was stressed along a particular direction, electrical charges, which are proportional to the stress and of opposite polarities, appeared on the opposite crystal surfaces. At that time, the brothers Curie called this effect “polar-electricity”. Later in 1881, Gabriel Lippmann deduced mathematically, based on the principles of thermodynamics, the inverse piezoelectric effect. The brothers Curie immediately confirmed this effect experimentally and published the first quantitative measurements of the inverse effect in quartz and in tourmaline. Meanwhile, Wilhelm Gottlieb Hankel observed similar results in 1881 and proposed the name “piezoelectricity”, based on the Greek word “πιέζειν”, meaning to press, as a technical term to refer to both of these effects. This term was promptly accepted by the scientific society of that time and is still used today [Tichý et al., 2010].

Piezoelectric material is material which displays the piezoelectric effect. They can be natural materials, for example tourmaline and quartz, or can be manufactured ceramics or polymers, for example lead zirconate titanate (PZT) or polyvinylidene fluoride (PVDF). The linear constitutive equations of piezoelectric materials are expressed as [IEEE, 1988]

$$\begin{Bmatrix} \mathbf{S} \\ \mathbf{D} \end{Bmatrix} = \begin{bmatrix} \mathbf{s^E} & \mathbf{d} \\ \mathbf{d_t} & \boldsymbol{\varepsilon}^{\mathbf{T}} \end{bmatrix} \begin{Bmatrix} \mathbf{T} \\ \mathbf{E} \end{Bmatrix}, \tag{2-1}$$

where **S** is the mechanical strain tensor**,** **T** is the mechanical stress tensor, **D** is the dielectric charge displacement tensor, and **E** is the electrical field strength. $\boldsymbol{s^E}$ is the compliance tensor under short-circuit conditions and $\boldsymbol{\varepsilon^T}$ is the permittivity tensor under constant stress conditions. Finally, $\mathbf{d}$ and $\mathbf{d}_t$ represent the charge constants tensors for the direct and inverse piezoelectric effects, respectively.

The standard piezoelectric material axes system is represented by the axes 1, 2, and 3. The shear about each one of these axes is represented by 4, 5, and 6, respectively. The direction of positive polarization is usually made to coincide with the 3 – axis and the electrodes are usually attached perpendicularly to this axis, as shown in Figure 2-2 . When these electrodes are connected, the device is short-circuited and the corresponding conditions apply; when they are open, as shown in Figure 2-2, then open-circuit condition are applicable.

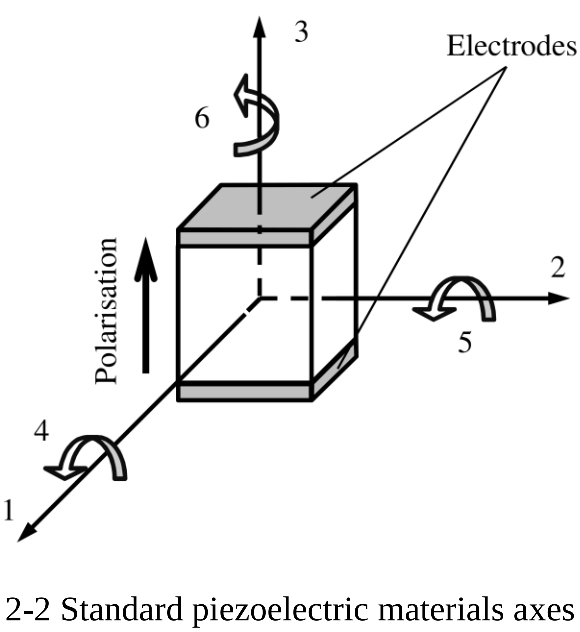

Figure 2-2 Standard piezoelectric materials axes system

For most practical applications, Equation (2-1) can be reduced to a scalar equation based on the operation mode, geometry and the boundary conditions of the piezoelectric device. The term “mode of operation” is used to describe the direction of the generated / applied voltage and the direction of applied / generated stress. For example, if the piezoelectric material is polarized and electrical field are in the 3-direction, while the mechanical stress and strain are in the 1-direction, then the mode of operation is 31-mode and the constitutive equations can be reduced to

$$S_1 = s_{11}^E T_1 + d_{31} E_3 \tag{2-2a}$$

and

$$D_3 = d_{31} T_1 + \varepsilon_{33}^T E_3 \ , \tag{2-2b}$$

where $s_{11}^E$is the compliance under short-circuit, d_{31} is the charge constant, ε_{33}^T is the preemptively under constant stress condition. Commonly, piezoelectric energy harvesters are designed to operate in 33-mode or 31-mode [Kim et al., 2009].

2.3 Piezoelectric Energy Harvester

A piezoelectric energy harvester is a device which utilizes piezoelectric materials to convert mechanical deformation into electrical voltage, which is then used to power an electronic device. Usually, this deformation is introduced by placing the harvester on a vibrating body.

Piezoelectric energy harvesters can be found in different setups based on the application requirements. The setup may differ in shape, with possibilities such as stacks, bimorphs, membranes, spiral rotational springs, etc., or it may differ in the type of support, such as cantilever, simply supported, built-in, etc.

The typically utilized setup for constructing a piezoelectric harvester is the cantilever beam [Erturk and Inman, 2009 and Lien and Shu, 2012]. Compared to other support types, it offers simplicity in construction, high flexibility and a low natural frequency. Often, a tip mass is attached to the free end of the cantilever to increase its deflection and reduce its natural frequency if the beam used is a commercially available devices with a pre-determined frequency. Usually, the cantilever beam is composed of one or two layers of piezoelectric material and another layer of another material used only to reinforce the beam structure. A beam with a single piezoelectric layer is called a unimorph; with two piezoelectric layers, it is then called a bimorph. The harvester is placed / mounted on a vibrating body, and then dynamic strain is induced in the piezoelectric layer (layers) due to beam deflection. This generates alternating voltage across the electrodes attached to the surface of the piezoelectric layer (layers).

Although the piezoelectric harvester is a promising technique for powering electronic devices, there are factors which limit the amount of generated voltage possible. One major limitation of a piezoelectric harvester is that it operates effectively at only a single excitation frequency. This excitation frequency matches the optimal frequency of the piezoelectric harvester, which is defined as the frequency at which the harvester generates the maximum voltage. It is determined by the harvester properties, geometry and the electrical part of the autonomous system. In most cases, the vibrating body has a range of acceleration amplitudes and frequencies. For example, if it is desirable to design a harvester that generates a voltage from human movement, it must be taken into account that the characteristics of this movement change from time to time according to the current activity (walking, running, sleeping, etc.). Therefore, it is desirable to design a piezoelectric harvester with a tunable optimal frequency or one which can operate effectively across a certain range of excitation frequencies. Such harvesters are essential for this technology to be commercially viable.

2.4 Autonomous System with Piezoelectric Harvester

Most of the literature related to autonomous systems with piezoelectric harvesters generally focuses on finding solutions for the inherent limitations of the piezoelectric harvester. There are only few publications concerned with designing complete autonomous systems. Lee et al. [2009], for example, introduced an autonomous system for monitoring the environmental temperature, and Reilly et al. [2011] introduced an autonomous system for monitoring ambient vibration. The former publication is focused on optimizing the structure of the piezoelectric harvester and expanding its bandwidth, while the latter is focused on designing an electrical circuit that fulfills the operation requirements. Both of these articles ignore the effect of the rectifiers and reservoir capacitors on the characteristics of the harvester. Münch et al. [2012] investigated a setup including a harvester, rectifier and capacitor. In this study, the effect of rectifier circuit on harvester performance and on the generated voltage characteristics was examined and noted. Unfortunately, their setup is missing the connected load and there is no clear explanation of the cause of changing characteristics in the generated voltage.

Ottman et al. [2002], Guyomar et al. [2005], Lefeuvre et al. [2005 and 2006], Shu and Lien [2009] and Lien and Shu [2012] modeled the output DC voltage generated by a piezoelectric harvester when connected to a rectifier, capacitor and resistive load (typical basic configuration). All models assume that the voltage generated by the piezoelectric harvester has a harmonic form. In real applications, this assumption can be inaccurate, because the form of the generated voltage signal is influenced by the rectification process, as well as by the connected load. The harvester can behave nonlinearly, especially if the connected load has low impedance.

In general, most of the rest of the published articles on the subject examine many topics concerning enhancement and optimization of the performance of piezoelectric harvesters. These topics are oriented in various directions and different approaches are used. Generally, these topics can be classified as follows: modeling approaches, harvesting circuits, frequency tuning methods, and bandwidth expanding techniques.

2.4.1 Modeling of the Piezoelectric Device

With the increasing interest in using a piezoelectric element to power electronic circuits for different applications, demand is also increasing to develop existing models for predicting the generated voltage across any circuit connected via the piezoelectric device electrodes. There are two classes of models, distinguished by the physical techniques used to handle those parameters: models with distributed parameters and models with lumped-parameters.

Models with distributed parameters are based on Euler-Bernoulli beam theory. These models evaluate the physical equations along the whole length of the beam. They generally give more accurate results than lumped-parameter models, but involve complicated mathematics and long mathematical expressions. Such models have, for example, been used by Lu et al. [2004], Chen et al. [2006], Lin et al. [2007], and Erturk and Inman [2009].

Discretization of a model with distributed parameters leads to a lumped-parameter model. Many researchers have used lumped-parameters for modeling piezoelectric harvesters, for example Roundy et al. [2003], Sodano et al. [2004], du Toit [2005], Shu and Lien [2009], Richter et al. [2006 and 2010], Twiefel et al. [2007] and Lien and Shu [2012]. Such models can be considered a less accurate approximation than one with distributed parameters, but they are accurate enough for many applications. They also provide an explicit understanding of the operation of piezoelectric harvesters and can be discussed using circuit theory by applying electro-mechanical analogies. This motivated Erturk and Inman [2009] to use their distributed parameters model to derive a correction factor for the lumped-parameters model by du Toit [2005], in order to improve its accuracy.

Hemsel et al. [1998] introduced an equivalent mechanical system similar to that shown in Figure 2-3a. This system was developed on the basis of a lumped-parameters model given by Lenk [1975]. Using this equivalent system is very useful in studying and optimizing the piezoelectric device. Therefore, this equivalent system is also used today in many publications, such as Richter et al. [2009] and Twiefel et al. [2007]. The parameters of this equivalent system are the equivalent mass M, the equivalent mechanical damping B, the equivalent mechanical stiffness K, the equivalent capacitance C_p, and α, the conversion factor between the mechanical and electrical domains. In this system, the damping and the stiffness are assumed to be linear. These assumptions can cause inaccuracy in the obtained results, especially if the amplitude of the excitation acceleration is large, as will be shown later in Section (4.5.2).

The equivalent electrical model has been developed over the past decades. Cady [1922] introduced an electrical circuit that brought the equivalent electromechanical characteristics together. This circuit consists of two parallel branches: the first represents the mechanical characteristics and contains an inductor in series with a capacitor, while the other is merely a capacitor representing the electrical nature of the piezoelectric element. This work was expanded by van Dyke [1925] to account for the mechanical losses of the piezoelectric element when an electrical resistance is added in series to the branch representing the mechanical characteristics. This circuit is known today as the Butterworth-van-Dyke circuit. Mason [1935] continued Cady's and van Dyke's work and introduced an ideal transformer between the mechanical and electrical branches to represent the electromechanical coupling of the piezoelectric element. Today, the equivalent electrical system of the piezoelectric device can be represented by the system shown in Figure 2-3b. This system is based on direct analogies between the mechanical and electrical variables: the generated or applied voltage $u(t)$ is analogous to an applied force in the equivalent mechanical system, and the electric charge $q(t)$ is analogous to mechanical displacement in the mechanical system. In the same vein, the applied force $F(t)$ in mechanical systems is analogous to a voltage source in the equivalent electrical system, and the displacement of the mass $x(t)$ is analogous to electrical charge in the electrical equivalent system

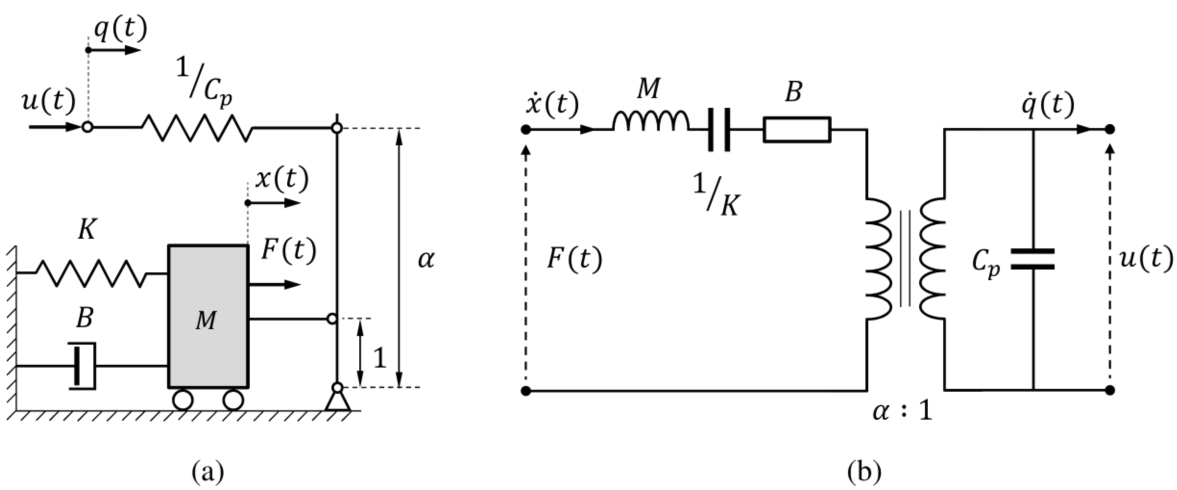

Figure 2-3 General equivalent systems of piezoelectric devices in (a) mechanical and (b) electrical representations

2.4.2 Harvesting Circuits

Most real-life applications require DC voltage, whereas a piezoelectric harvester generates an AC voltage. Therefore, it is essential to use a rectifying circuit in order to provide power for such applications. Using a full wave AC-DC rectifying circuit is common for such purposes [Shu and Lien, 2009]; this makes it necessary to use a capacitor of the proper size, known as the reservoir capacitor, in order to smooth the output DC voltage. The circuit consisting of the rectifying circuit and reservoir capacitor is known as the standard harvesting circuit, shown in Figure 2-4a.

Another harvesting circuit has been developed which is known as the synchronized switch harvesting inductor (SSHI), shown in Figure 2-4b. This circuit also consists of the rectifier and capacitor, plus an electrical switch and inductor. The electrical switch is triggered in tact with the maximum and minimum deflection of the harvester in order to minimize the energy lost during the rectifying process. Such a circuit has been investigated by several researchers, for example, Guyomar et al. [2005], Badel et al. [2005 and 2006], Shu and Lien [2009] and Neubauer et al. [2009].

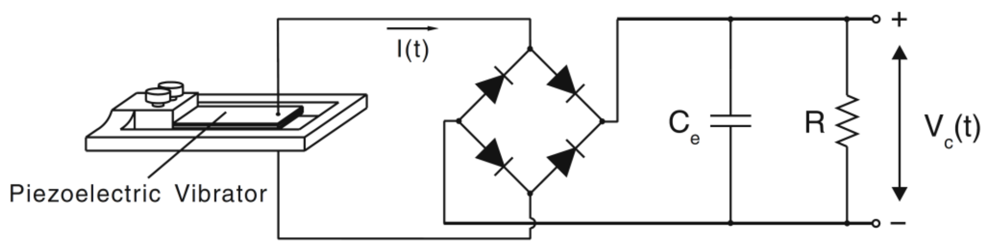

(a)

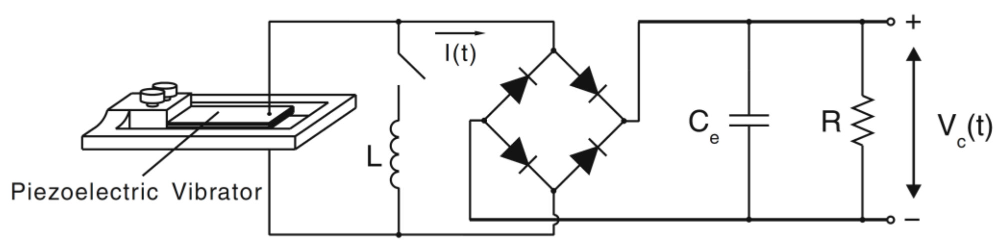

(b)

Figure 2-4 Autonomous system with (a) standard energy harvesting circuit (b) SSHI energy harvesting circuit [Shu and Lien, 2009]

Using the inductor and synchronized electrical switch makes the SSHI circuit consume more power than the standard harvesting circuit. This has motivated many researchers to investigate how to minimize the power dissipation of an SSHI, among them Makihara et al [2006], Lallart and Guyomar [2008], Do et al [2011] and Liang and Liao [2012].

2.4.3 Frequency Tuning Methods

There are many methods can be used to tune the characteristic frequencies of the piezoelectric harvester. These methods differ in both concept and design. A brief review of many developed tuning methods can be found in Zhu et al [2010a]. Here, the focus has been on the tuning methods which are based on applying an external mechanical force in order to change the characteristic frequencies of the piezoelectric harvester.

Lesieutre and Davis [1997] investigated the dependency of piezoelectric electromechanical coupling on mechanical axial pre-compression. In this study, it was concluded that applying a preload of half the buckling load to a symmetrical piezoelectric bimorph device can change the structural stiffness and increase the coupling coefficient by more than 40%. Leland and Wright [2006] later used the method of applying axial pre-compression to a simply supported piezoelectric bimorph to tune its natural frequency. There, it was found that a compressive axial pre-load can reduce the resonance frequency of the harvester by up to 24% and increase the coupling coefficient by up to 25%. Hu et al. [2007] further developed this method and proposed a special cantilever bimorph where the axial compression load can be adjusted by tightening a nut, as shown in Figure 2-5.

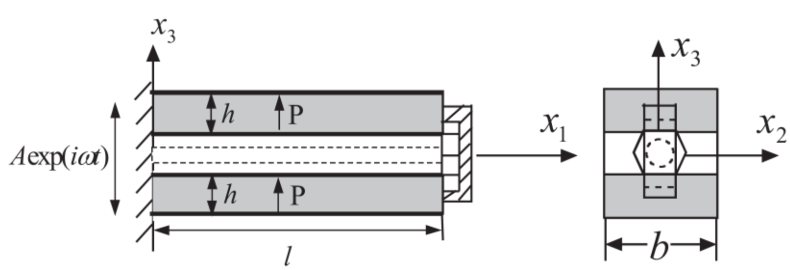

Figure 2-5 Schematic illustration of the technique used to apply an axial preload to a piezoelectric bimorph introduced by Hu et al. [2007]

Challa et al. [2008] presented resonance frequency tuning using a magnetic force. Two small cylindrical magnets at the free end of the cantilever were used, one on the top and one on the bottom, and vertically aligned with two magnets above and below the first two magnets, as shown in Figure 2-6. Magnetic repulsion was used for the lower side and magnetic attraction was used for the upper side. The harvester can thus be tuned by varying the distances between these magnets. In this setup, the shape of the unexcited cantilever depends on the position of the magnets, and the magnetic forces are asymmetrical for both positive and negative deflection.

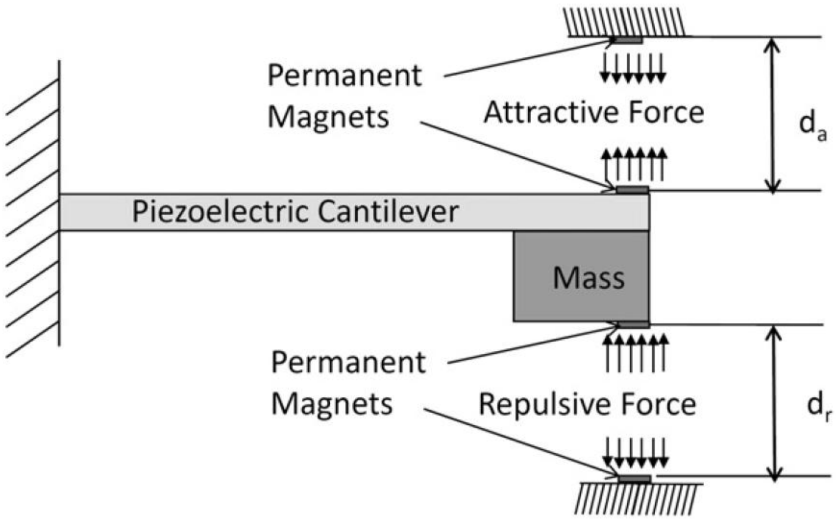

Figure 2-6 Schematic diagram of the setup introduced by Challa et al. [2008]

Zhu et al. [2010b] used the attraction force between two axially aligned permanent magnets to change the resonance frequency of a cantilever beam in an electromagnetic generator, as shown in Figure 2-7. In this design, the opposing faces of the relatively large magnets are curved in order to maintain a constant distance between the two magnets during operation. The resonance frequency of the system can be successfully tuned between 67.6 and 98 Hz. However, in modeling this effect, the authors only consider axial tensile forces, and their model fits well only for larger separation distances.

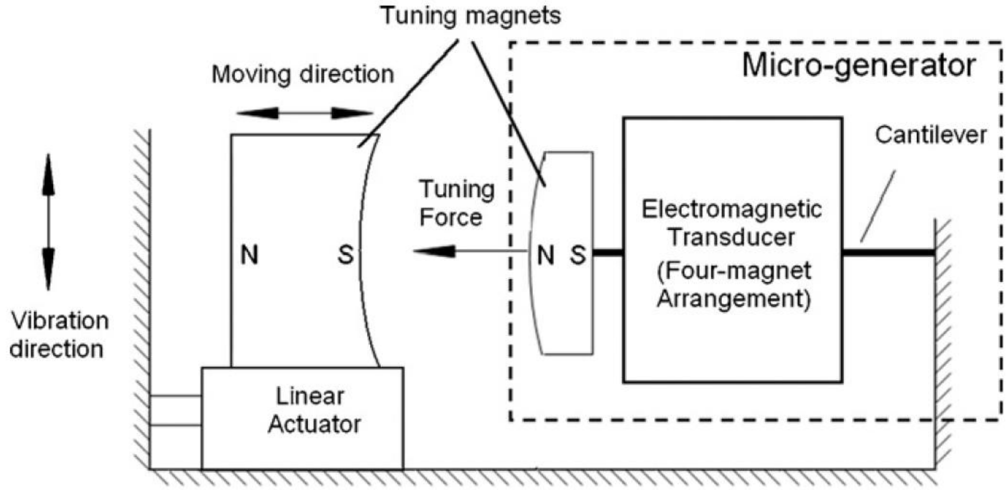

Figure 2-7 Schematic diagram of the setup used by Zhu et al. [2010b]

There are many publications, for example Cottone et al. [2009], Stanton et al. [2010] and Karami and Inman [2011], which have used the repulsion force between two magnets. The repulsion force can change the behavior of the harvester from being a structure with a single equilibrium position to a structure with dual equilibrium positions, as shown in Figure 2-8. This change can enhance the harvester performance with respect to variation of the excitation frequency.

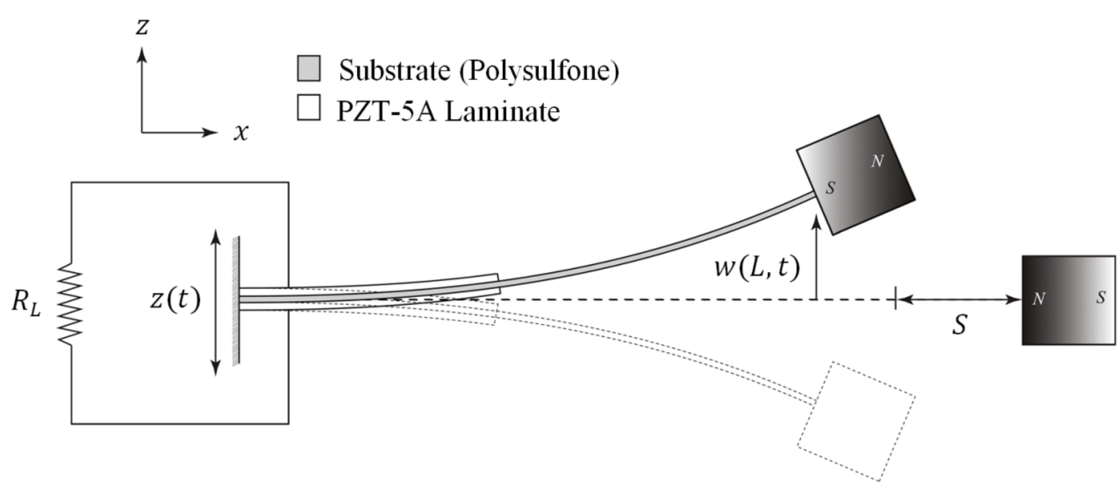

Figure 2-8 Schematic diagram of a piezoelectric harvester with repelled magnets Stanton et al. [2010]

2.4.4 Bandwidth Expanding Techniques

Tang et al. [2010] presented a comprehensive review of most of the techniques developed over the years to overcome the above-mentioned bandwidth limitation of piezoelectric harvesters. This review classifies the known solutions into two main categories: characteristic frequencies tuning and multimodal energy harvesting. Characteristic frequencies tuning is further sub-divided into mechanical methods, electrical methods and magnetic methods; multimodal energy harvesting is divided into hybrid energy harvesting schemes and cantilever arrays.

Characteristic frequencies tuning techniques can be more conveniently divided into manual and self-tuning methods. The self-tuning methods could also be subdivided into active tuning and passive tuning methods. Active tuning methods continuously consume power, while passive tuning methods only require power initially for tuning the harvester frequency.

Up to date, there are many attempts to design a harvester with self-tuning method, but unfortunately no reliable system has been developed until now. For example, the systems developed by Lallart et al. [2010] and that developed by Challa et al. [2011] are both required external power sources in order to be operating. The system introduced by Eichhorn et al. [2011] includes a microprocessor which relies on stored information about the operation of the system at a given excitation.

A harvester cantilever array consists of multiple piezoelectric cantilevers integrated within one harvester in order to increase its bandwidth and/or output power. Even if a subset of the piezoelectric elements in such an array is not actively harvesting energy in a given situation, it is often more efficient than self-tuning techniques, which require additional sensors, control elements, and circuitry.

Shahruz [2006] introduced so-called mechanical band-pass filters consisting of multiple cantilevers, as shown in Figure 2-9. The number of cantilevers and the resonance frequencies required for the desired bandwidth are determined from the individual transfer functions of the tip deflection in terms of the applied acceleration. Dimensions and proof masses are calculated from the pre-defined resonance frequency. In this paper, the author generally does not consider the electrical part, and thus cannot investigate the electrical effect each cantilever has on the others.

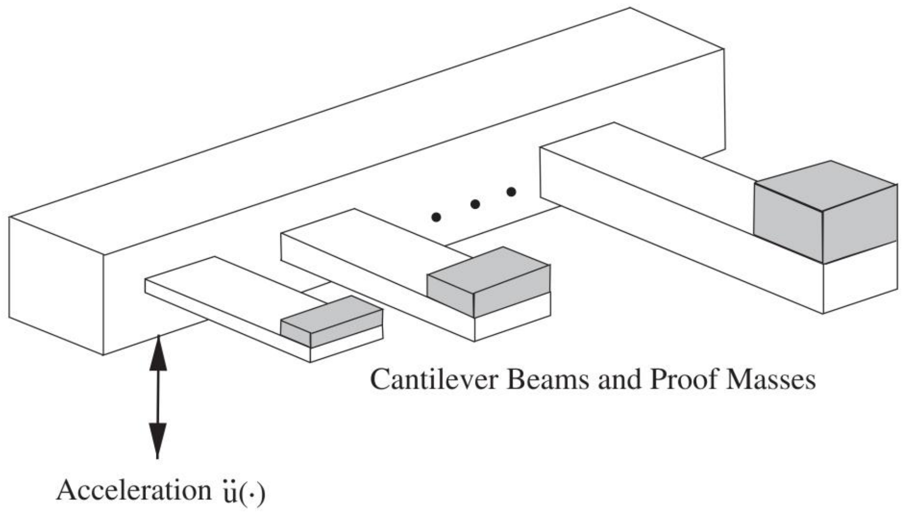

Figure 2-9 Ensemble of cantilever beams with proof masses at their tips [Shahruz, 2006]

Ferrari et al. [2007] designed a multi-frequency piezoelectric harvester which consists of three cantilever bimorphs with the same dimensions. The authors determined the resonance frequency of each bimorph by adjusting the tip mass. The piezoelectric harvester is modeled as a voltage source in series with a branch consisting of a resistor and a capacitor in parallel. This allows an explicit description the effect of the bimorphs on each other. In this setup, a half-wave AC-DC rectifier is used for each bimorph, primarily for two reasons: the electronic application needs DC power, and power transfer between the bimorphs is thus prevented.

Xue et al. [2008] presented another design of an array of cantilevers with different resonance frequencies. Each cantilever has two piezoelectric layers and its resonance frequency is adjusted by varying their thickness as shown in Figure 2-10. The authors concluded that connecting multiple bimorphs in series increases not only the harvested power but also the harvester bandwidth. In this study, 10 piezoelectric bimorphs of different thicknesses were used to harvest power across a bandwidth of 25 Hz. However, the mathematical model given in this work ignores the electrical effect of the bimorphs on each other. Also, the effect of connecting multiple bimorphs in parallel or in series to the optimal load of the complete harvester is not investigated.

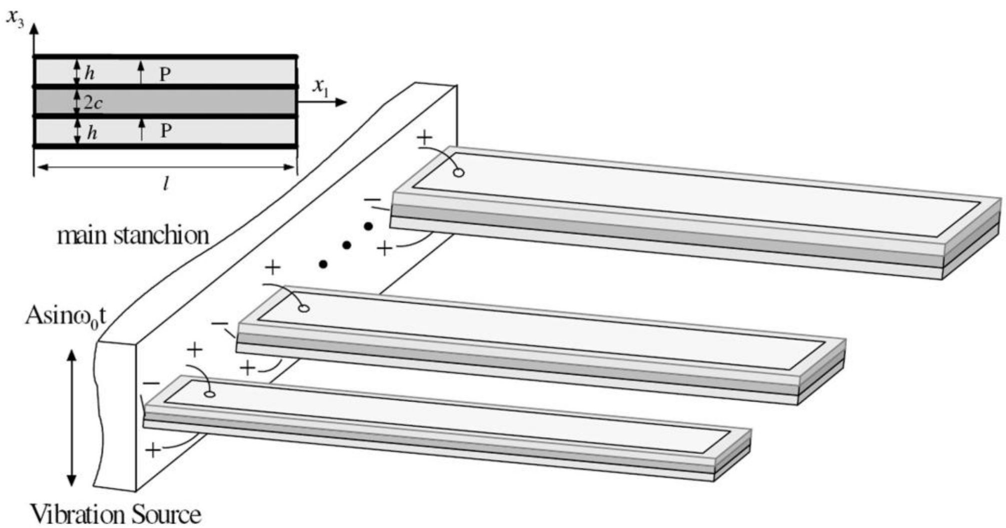

Figure 2-10 Schematic illustration of a Piezoelectric bimorphs harvesting [Xue et al., 2008]

Liu et al. [2008] designed and produced a cantilever array of micrometer-size and investigated the power generation characteristics for cantilevers connected in series. The authors concluded that the phase difference impaired the voltage accumulation of the piezoelectric cantilevers. This problem was solved by using a full-wave AC-DC rectifier for each piezoelectric cantilever. In this setup, the power consumed by the rectification process was much more than the power consumed by the electronic application, but the device was claimed to be promising for ultra-low-power applications.

Richter [2010] constructed an array with six cantilevered piezoelectric bimorphs in order to fulfill the power requirement of an electronic application. The vibrating length of each bimorph was adjusted in order to tune the optimal frequency of each bimorph. The author concluded that the bimorphs should be tuned to the same optimal frequency in order to increase the harvested power.

Lien and Shu [2012] studied a cantilever array including piezoelectric elements connected in parallel. The harvester in the paper is first modeled when connected to a standard harvesting circuit, and is then modeled when connected to a SSHI circuit. The modeling technique used is called the equivalent impedance approach. This approach is based on deriving the equivalent impedance of the rectifier, the capacitor and the load. The authors concluded that, when all the piezoelectric elements have the same optimal frequency, the generated DC voltage can increase, but when they have different optimal frequencies then the bandwidth can be expanded.

It is difficult to implement any of the harvesters presented in the aforementioned publications in industrial applications. The proposed setups require very accurate manufacturing processes and careful handling, and operate within an unchangeable frequency band. If the frequency spectrum of the host changes, for example due to wear or changed operating conditions, those arrays will be useless. Another fact worth mentioning is that the characteristic frequencies of piezoelectric elements may also change, due to aging, temperature, vibration level etc.

.

3 Characteristics of the Piezoelectric Devices

This chapter introduces a model for calculating the parameters of the mechanical and electrical equivalent systems. Additionally, it presents a further model for characteristic frequencies of piezoelectric devices. Both these models are based on material properties, geometry and boundary conditions (mechanical and electrical) of the piezoelectric device which is defined here as that device which consists of piezoelectric materials excited harmonically by either applied external mechanical or electrical stimuli. These two models are validated by laboratory measurements with a cantilever bimorph. They show good correlation with the experimental results

3.1 Characteristics of the Piezoelectric Devices

A piezoelectric device has general characteristics that determine its performance and efficient operating conditions. These characteristics include the structural stiffness, the mechanical and electrical admittances and the characteristic frequencies. These characteristics should be modeled in order to optimize the performance of the piezoelectric device.

3.1.1 Structural Stiffness

In order to analyze the stiffness of the piezoelectric device, the case of quasi-static operation is investigated where inertia and damping can be neglected. Two stiffness limits for a piezoelectric structure can be deduced from the mechanical model shown in Figure 2-3a, where the stiffness is defined as the applied force per the mechanical displacement, i.e. $F(t)/x(t)$. If the electrodes are short-circuited, charge can flow freely and no voltage is built up, i.e. $u(t) = 0$. This state defines the lower stiffness limit. The relationship between force and displacement in this case is described by

$$F(t) = Kx(t). \tag{3-1}$$

If the electrodes of the element are open, no charge can flow, i.e. $q(t) = 0$. This defines the upper stiffness limit. The relationship between force and displacement is described by

$$F(t) = \left(K + \frac{\alpha^2}{C_p}\right) x(t). \tag{3-2}$$

Equation (3-2) shows that the stiffness of the piezoelectric device not only depends on the mechanical properties and boundary conditions, but also depends on the electrical properties and boundary conditions.

3.1.2 Mechanical and Electrical Admittance / Impedance

The mechanical admittance of a piezoelectric device $\hat{Y}_m(s)$ is defined as the ratio of the Laplace transform of its velocity of vibration to the Laplace transform of the applied harmonic voltage in the absence of any external forces [Richter et al., 2009]. The mechanical admittance $\hat{Y}_m(s)$ can be calculated from applying Newton's second law to mechanical equivalent model shown in Figure 2-3a with $F(t) = 0$, thus

$$M\ddot{x}_u(t) + B\dot{x}_u(t) + Kx_u(t) = \alpha u(t), \tag{3-3}$$

where $x_u(t)$ is the displacement of the vibrating mass M. This displacement is caused from applying the harmonic voltage $u(t)$ only. Therefore, the mechanical admittance $\hat{Y}_m(s)$ can be expressed as

$$\hat{Y}_m(s) = \frac{\alpha s}{Ms^2 + Bs + K}. \tag{3-4}$$

This mechanical admittance $\hat{Y}_m(s)$ can be rewritten in term of the excitation frequency ω as

$$\hat{Y}_m(j\omega) = \frac{j\alpha\omega}{(K - M\omega^2) + jB\omega}. \tag{3-5}$$

This complex ratio can be expressed in its real and imaginary parts as

$$\hat{Y}_m(j\omega) = Y_m^R + jY_m^I. \tag{3-6}$$

The real and imaginary parts of the mechanical admittance are determined as

$$Y_m^R = \frac{\alpha B\omega^2}{(K - M\omega^2)^2 + (B\omega)^2} \tag{3-7}$$

and

$$Y_m^I = \frac{\alpha\omega(K - M\omega^2)}{(K - M\omega^2)^2 + (B\omega)^2}. \tag{3-8}$$

If the piezoelectric device is a linear system, then its electrical admittance $\hat{Y}_{el}(s)$ is defined as the ratio of the Laplace transform of the total flowing current $\hat{\imath}_u(s)$ to the Laplace transform of the applied external voltage $\hat{u}(s)$ in the absence of any external force. Applying this to the electrical equivalent system shown in Figure 2-3b and with some modifications based on circuit theory, the circuit shown in Figure 3-1 can be obtained.

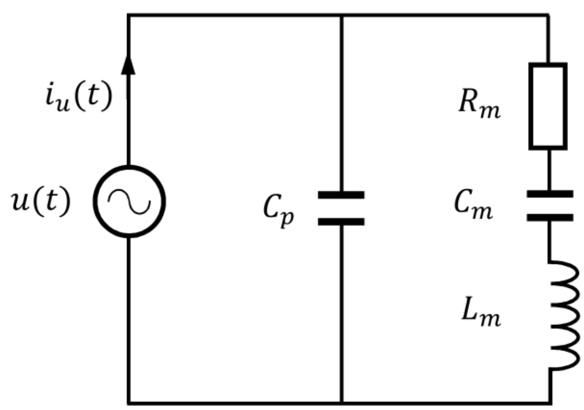

Figure 3-1 Reduced equivalent circuit

Thus, the electrical admittance $\hat{Y}_{el}(s)$ can be expressed as

$$\hat{Y}_{el}(s) = \frac{\hat{\imath}_u(s)}{\hat{u}(s)}. \tag{3-9}$$

Using Figure 3-1, the electrical admittance $\hat{Y}_{el}(s)$ can be expressed as

$$\hat{Y}_{el}(s) = \frac{L_m C_m C_p s^3 + R_m C_m C_p s^2 + \left(C_p + C_m\right)s}{L_m C_m s^2 + R_m C_m s + 1}. \tag{3-10}$$

The electrical admittance $\hat{Y}_{el}(s)$ can be expressed in term of the excitation frequency ω as

$$\hat{Y}_{el}(j\omega) = \frac{-R_m C_m C_p \omega^2 + j\left[\left(C_p + C_m\right)\omega - L_m C_m C_p \omega^3\right]}{1 - L_m C_m \omega^2 + jR_m C_m \omega}. \tag{3-11}$$

It is also a complex ratio which can be expressed by its real and imaginary parts as

$$\hat{Y}_{el}(j\omega) = Y_{el}^R + jY_{el}^I . \tag{3-12}$$

These two parts are found to be

$$Y_{el}^R = \frac{R_m C_m^2 \omega^2}{(1 - C_m L_m \omega^2)^2 + (R_m C_m \omega)^2}, \tag{3-13}$$

and

$$Y_{el}^I = \omega \left\{ \frac{C_m(1 - C_m L_m \omega^2) + C_p[(1 - C_m L_m \omega^2)^2 + (R_m C_m \omega)^2]}{(1 - C_m L_m \omega^2)^2 + (R_m C_m \omega)^2} \right\}. \tag{3-14}$$

The reduced circuit parameters are

$$R_m = \frac{B}{\alpha^2}, \tag{3-15a}$$

$$L_m = \frac{M}{\alpha^2} \tag{3-15b}$$

and

$$C_m = \frac{\alpha^2}{K}. \tag{3-15c}$$

These parameters will be modeled later in Section (3.2.1).

3.1.3 Characteristic Frequencies

Figure 3-2 shows a typical frequency sweep of the electrical admittance of a piezoelectric device in a certain range of excitation frequencies (based on Equation (3-12)).

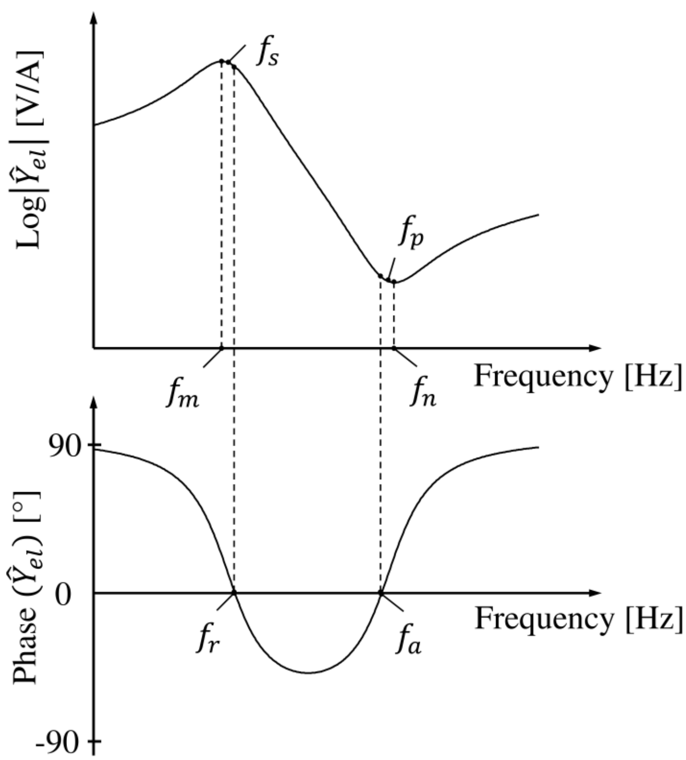

Figure 3-2 Typical electrical admittance of a piezoelectric device

Figure 3-2 shows that at f_m and f_n the admittance reaches its maximum and minimum magnitude, respectively. Also in this range of frequency, the phase of the electrical admittance is equal to zero in two cases (meaning the admittance is purely real) at f_r and f_a. In Figure 3-1, at the series resonance frequency f_s (removing C_p), the admittance of the electrical branch of the equivalent circuit model is zero and the system is undamped ($R_m = 0$). At the parallel resonance frequency f_p (reintroducing C_p), the same admittance is infinite and also the system is undamped ($R_m = 0$).

These characteristic frequencies will be modeled later in Section (3.2.2). They are calculated based on the geometry, the boundary conditions and the properties of the material of the piezoelectric device. Table 3-1 lists the characteristic frequencies of a piezoelectric device and their definitions:

Table 3-1 Characteristic frequencies of a piezoelectric device

Symbol	Definition
f_m	Frequency of maximum electrical admittance
f_n	Frequency of minimum electrical admittance
f_r	Resonance frequency
f_a	Anti-resonance frequency
f_s	Series resonance frequency
f_p	Parallel resonance frequency

According to IEEE [1966], each of these frequencies approximates two other characteristic frequencies in most practical applications when the piezoelectric device has low damping ratio ζ i.e $\zeta \ll 1$, thus

$$f_m \approx f_s \approx f_r \,, \tag{3-16}$$

and

$$f_n \approx f_p \approx f_a \,. \tag{3-17}$$

These two assumptions are used to simplify the model which describes the characteristics of piezoelectric device.

3.2 Calculation of the Characteristics of a Piezoelectric Device

Piezoelectric devices are nowadays used in many different applications. A better understanding of the influence of material properties, geometry and boundary conditions on the performance of these devices requires an analytical calculation of the parameters of the equivalent systems (mechanical and electrical). Additionally, the experimental identification process of these parameters needs a prototype of the theoretical device, expensive measuring equipment, and sufficient skill to identify the parameters of the devices.

In order to provide an explicit understanding of the analytical modeling procedure for the parameters of the equivalent systems, it is preferable to define a certain case where the design of the piezoelectric device (mechanical boundary conditions, the geometry and the operating mode) is given, and then to model that case. The modeling procedure applied in the next section can then later be followed for any other design of a piezoelectric device by including its specific characteristics in the model.

To apply the modeling procedure, a cantilever piezoelectric bimorph has been chosen as an example application. This kind of cantilever is a typical piezoelectric device used in vibration beam applications. It consists of a shim layer sandwiched between two piezoceramic layers – thus the name “bimorph”, due to its two active layers. Figure 3-3 shows a cross section of such a bimorph structure, where w is the width of the beam, l_p is the length of the piezoelectric layers, l is the free (vibrating) length of the beam, h_p is the thickness of an individual piezoelectric ceramic layer, and h_{sh} is the thickness of the shim layer. The coordinate system is the same as the standard one introduced in section (2.2). All formulations are based on two assumptions: the first that $h \ll w \ll l$, i.e. there are no normal stress and shear stress in the 3-direction. The second assumption is that the beam experiences a small deflection. Piezoelectric cantilevers commonly operate in 33-mode or 31-mode. For the following calculations, operation in 31-mode is assumed [IEEE, 1988].

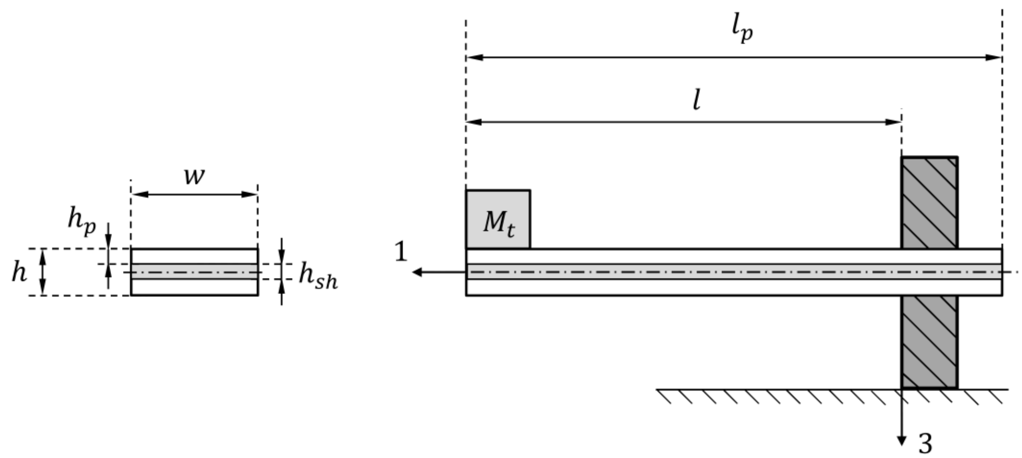

Figure 3-3 Piezoelectric bimorph cantilever and its cross section

3.2.1 Calculation of the Parameters of the Equivalent System

The piezoelectric bimorph shown in Figure 3-3 can be described by using lumped-parameters model. This model is only accurate for the first mode of vibration. Thus, the equivalent stiffness of the cantilever beam K can be expressed as [Kim et al., 2009]

$$K = \frac{3E_b I_b}{l^3}, \tag{3-18}$$

where E_b, I_b and l are the modulus of elasticity, the moment of inertia and the length of the beam, respectively. The natural frequency can be obtained by

$$f_b = \frac{1}{2\pi}\sqrt{\frac{K}{M}}\ , \tag{3-19}$$

where M is the equivalent mass which can be calculated as [Timoshenko, 1937]

$$M = \frac{33}{140} M_b + M_t\ , \tag{3-20}$$

where M_b and M_t are the mass of the vibrating beam and the tip mass attached to the cantilever free end, respectively. The mass of the vibrating beam M_b is expressed as

$$M_b = \left(2\,\rho_p\,h_p + \rho_{sh}\,h_{sh}\right) w\,l, \tag{3-21}$$

with ρ_p as the piezoelectric material density and ρ_{sh} as the density of the shim.

Generally, the modulus of elasticity of a piezoelectric layer E_p depends on the condition of its electrodes (open or short). Thus, the modulus of elasticity under short-circuit conditions E_{psc} can be expressed as [Morgan Electro Ceramics 2007, 2009]

$$E_{psc} = \frac{1}{s_{11}^E}, \tag{3-22}$$

and the modulus of elasticity under open-circuit condition E_{poc} which can be expressed as [Morgan Electro Ceramics 2007, 2009]

$$E_{poc} = \frac{1}{s_{11}^D}. \tag{3-23}$$

The relation of the compliance s_{11}^D to the compliance s_{11}^E for the 31-mode of operation can be expressed by [Morgan Electro Ceramics 2007, 2009]

$$s_{11}^D = s_{11}^E(1 - k_{31}^2)\,. \tag{3-24}$$

Substituting Equation (3-24) into Equation (3-23) gives

$$E_{poc} = \frac{1}{s_{11}^E(1 - k_{31}^2)}\,. \tag{3-25}$$

The bimorph shown in Figure 3-3 includes three layers which have different moduli of elasticity. Therefore, the transformed cross section method can be used to calculate the moment of inertia of this beam. This method allows the width of the layers to be proportioned by the ratio of their moduli of elasticity, thereby defining the entire bimorph as having one modulus of elasticity [Beer and Johnston, 1992]. If this method is applied to the beam shown in Figure 3-3 with assuming that all the three layers are now fabricated from the piezoelectric material, then the equivalent width of the shim layer w_e can be expressed as

$$w_e = \frac{E_{sh}}{E_p} w, \tag{3-26}$$

where E_{sh} and E_p are the moduli of elasticity of the shim and the piezoelectric layers, respectively. Thus, the equivalent cross sectional area of the bimorph can be represented as that shown in Figure 3-4.

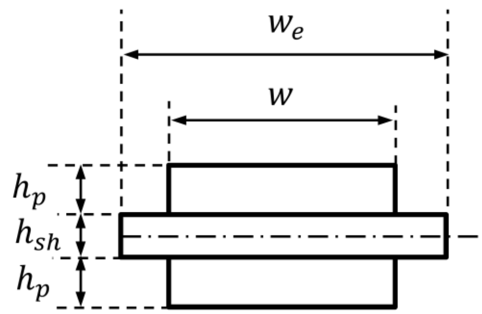

Figure 3-4 Equivalent cross sectional area of a piezoelectric bimorph

The moment of inertia of the beam I_b, which consists of p layers, can be calculated from using the parallel axis theorem [Beer and Johnston, 1992], thus

$$I_b = I_r + \sum_{i=1}^{i=p} I_i + A_i x_i \,, \tag{3-27}$$

where I_r is the moment of inertia of the reference layer. I_i and A_i are the moment of inertia and the cross sectional area of the i^{th} layer, respectively. x_i is the distance between the center of the i^{th} layer and the center of the reference layer.

For the cross sectional shown in Figure 3-4, the central layer is chosen to be the reference one due to the symmetry. Therefore, the moment of inertia of the reference layer can be expressed as [Beer and Johnston, 1992]

$$I_r = \frac{w_e h_{sh}^3}{12} \,. \tag{3-28}$$

The moment of inertia of the other two identical piezoelectric layers can be calculated as

$$I_i = I_p = \frac{wh_p^3}{12}. \tag{3-29}$$

Substituting Equations (3-28) and (3-29) into Equation (3-27) gives that the moment of inertia of the bimorph can be calculated as

$$I_b = \frac{w_e h_{sh}^3}{12} + 2\left[\left(\frac{wh_p^3}{12}\right) + wh_p\left(\frac{h_{sh} + h_p}{2}\right)^2\right]. \tag{3-30}$$

Substituting Equation (3-26) into Equation (3-30) and simplifying the obtained result gives

$$I_b = \frac{w}{12}\left(\frac{E_{sh}}{E_p} h_{sh}^3 + 2h_p^3\right) + \frac{wh_p}{2}\left(h_{sh} + h_p\right)^2. \tag{3-31}$$

Equations (3-23) and (3-25) shows that the bimorph has two moduli of elasticity based on its electrodes condition, thereby the bimorph has also two moments of inertia: moment of inertia under short-circuit condition I_{bsc} and moment of inertia under open-circuit condition I_{boc}. Substituting Equation (3-23) into Equation (3-31) resulting that the moment of inertia under short-circuit condition I_{bsc} can be expressed as

$$I_{bsc} = \frac{w}{12}\left(s_{11}^E E_{sh} h_{sh}^3 + 2h_p^3\right) + \frac{wh_p}{2}\left(h_{sh} + h_p\right)^2. \tag{3-32}$$

The moment of inertia under open-circuit conditions I_{boc} can be calculated from substituting Equation (3-25) into Equation (3-31), thus

$$I_{boc} = \frac{w}{12}\left[s_{11}^E (1 - k_{31}^2) E_{sh} h_{sh}^3 + 2h_p^3\right] + \frac{wh_p}{2}\left(h_{sh} + h_p\right)^2. \tag{3-33}$$

Referring to Equation (3-18), the lower stiffness limit is

$$K_{bsc} = \frac{3E_{psc}\, I_{bsc}}{l^3} \tag{3-34}$$

and the upper stiffness limit is

$$K_{boc} = \frac{3\, E_{poc}\, I_{boc}}{l^3}\,. \tag{3-35}$$

Substituting Equation (3-34) into Equation (3-19) gives that the short-circuit resonance frequency can be expressed as

$$\omega_{sc} = \sqrt{\frac{K_{bsc}}{M}}\,. \tag{3-36}$$

Also, substituting Equation (3-35) into Equation (3-19) gives that the open-circuit resonance frequency can be calculated as

$$\omega_{oc} = \sqrt{\frac{K_{boc}}{M}}\,. \tag{3-37}$$

Richter [2010] modeled the equivalent capacitance of a piezoelectric layer $C_{p,1}$ operating in the 31-mode. In this work, the capacitance $C_{p,1}$ is modeled by calculating the current flowing into it from using the constitutive equation of the piezoelectric materials, then equating the obtained equation to that equation for the current flowing into a standard capacitor. Thus, the capacitance of one piezoelectric layer $C_{p,1}$ can be expressed as

$$C_{p,1} = \frac{w l_p \varepsilon_{33}^T (1 - k_{31}^2)}{h_p}\,. \tag{3-38}$$

If the two piezoelectric layers of the bimorph structure (shown in Figure 3-3) are connected in parallel, the total capacitance of the bimorph C_p equals $2C_{p,1}$; if they are connected in series, C_p is given by $C_{p,1}/2$.

Referring to the structural stiffness introduced in Section (3.1.1), specifically to Equation (3-2) and Equation (3-1), the following relationship can be deduced

$$K_{boc} = K_{bsc} + \frac{\alpha^2}{C_p}. \tag{3-39}$$

Therefore from Equations (3-36), (3-37) and (3-39), the conversion factor α can be expressed as

$$\alpha = \sqrt{(\omega_{oc}^2 - \omega_{sc}^2) M C_p}\,. \tag{3-40}$$

The equivalent damping coefficient B can be expressed as

$$B = 2\zeta M \omega_{sc}\,, \tag{3-41}$$

where ζ is the damping ratio. Substituting Equations (3-40) and (3-41) into Equation (3-15a) yields

$$R_m = \frac{2\zeta \omega_{sc}}{(\omega_{oc}^2 - \omega_{sc}^2) C_p}\,. \tag{3-42a}$$

The equivalent inductance L_m can also be calculated from substituting Equation (3-40) into (3-15b), thus

$$L_m = \frac{1}{(\omega_{oc}^2 - \omega_{sc}^2) C_p}\,. \tag{3-42b}$$

The equivalent capacitance C_m can be found from substituting Equation (3-40) into (3-15c) to have

$$C_m = \left(\frac{\omega_{oc}^2 - \omega_{sc}^2}{\omega_{sc}^2}\right) C_p. \tag{3-42c}$$

Now, all the parameters of the equivalent systems (mechanical and electrical) of a piezoelectric bimorph are modeled.

3.2.2 Calculation of the Characteristic Frequencies

From the definitions of the series resonance frequency ω_s and the parallel resonance frequency ω_p given in Section (3.1.3), it is concluded that the series resonances frequency ω_s corresponds to the short-circuit natural frequency ω_{sc} (Equation (3-36)). The parallel resonances frequency ω_p corresponds to the open-circuit natural frequency ω_{oc} (Equation (3-37)).

It is shown in Figure 3-2 that the electrical admittance of the piezoelectric device has zero phases at resonance and anti-resonance frequencies. This means that the admittance is purely real and the imaginary part is equal to zero. Thus, equating the imaginary part, given in Equation (3-14), to zero gives

$$C_m\left(1 - C_m L_m \omega_{r,a}^2\right) + C_p\left[\left(1 - C_m L_m \omega_{r,a}^2\right)^2 + \left(R_m C_m \omega_{r,a}\right)^2\right] = 0\,. \qquad (3\text{-}43)$$

Equation (3-43) can be simplified to

$$\omega_{r,a}^4 + \beta_1 \omega_{r,a}^2 + \beta_2 = 0, \qquad (3\text{-}44)$$

where

$$\beta_1 = \frac{C_m C_p R_m^2 - C_m L_m - 2C_p L_m}{C_p C_m L_m^2} \qquad (3\text{-}45a)$$

and

$$\beta_2 = \frac{C_p + C_m}{C_p C_m^2 L_m^2}. \qquad (3\text{-}45b)$$

The solution to Equation (3-44) for the resonance frequency can be expressed as

$$f_r = \frac{1}{2\pi}\sqrt{\frac{-\beta_1 - (\beta_1^2 - 4\beta_2)^{\frac{1}{2}}}{2}}\,, \qquad (3\text{-}46)$$

and for the anti-resonance can be expressed as

$$f_a = \frac{1}{2\pi}\sqrt{\frac{-\beta_1 + (\beta_1^2 - 4\beta_2)^{\frac{1}{2}}}{2}}. \qquad (3\text{-}47)$$

Four of the six characteristic frequencies which were described in Section (3.1.3) are formulated in Equation (3-36) and Equation (3-37) for the parallel and series resonance frequencies respectively, and in Equation (3-46) and Equation (3-47) for the resonance and anti-resonance frequencies. The maximum and minimum admittance frequencies can be calculated from

$$\frac{d\left|\hat{Y}_{el}\right|}{d\omega} = 0\,. \tag{3-48}$$

The analytical solution to Equation (3-48) is a very long term. Therefore, it is determined numerically from a simulated admittance frequency sweep.

3.3 Identification of the Characteristics of a Piezoelectric Device

The magnitude and phase of the electrical admittance curves can be obtained experimentally for a range of excitation frequencies by using gain / phase analyzer equipment; the characteristic frequencies can then be directly identified from the measurement. These measured curves can be redrawn in the complex plane to produce a circle, as shown in Figure 3-5. The reactance of the piezoelectric capacitance X_p, the piezoelectric device bandwidth $\omega_2 - \omega_1$, and its radius r_{el} can all be determined from this circle.

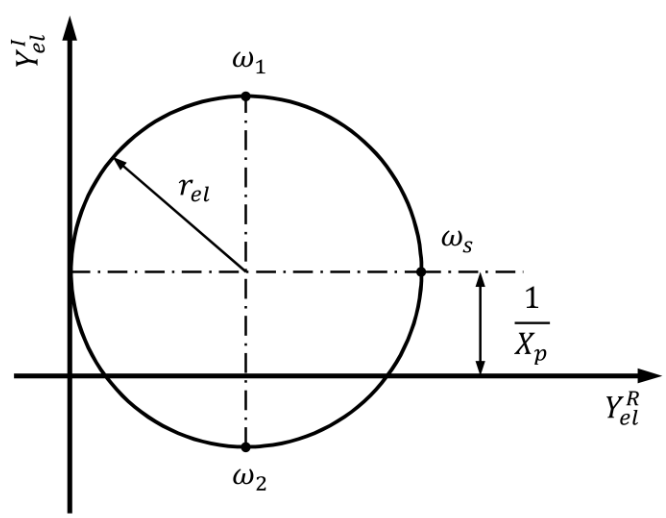

Figure 3-5 Frequency response locus of the electrical admittance of a piezoelectric device, adopted from [Richter et al., 2009]

Then the parameters of the equivalent electrical system shown in Figure 3-5 can be identified using the following relationships [Richter et al., 2009]

$$R_m = \frac{1}{2r_{el}}, \tag{3-49a}$$

$$L_m = \frac{R_m}{\omega_2 - \omega_1}, \tag{3-49b}$$

$$C_m = \frac{1}{L_m \omega_s^2}, \tag{3-49c}$$

and

$$C_p = \frac{1}{\omega_s X_p}. \tag{3-49d}$$

To identify the parameters of mechanical equivalent systems, similar circle drawn using experimental measurements, representing the frequency response locus of the mechanical admittance, is required. This is accomplished by measuring the velocity of the piezoelectric device per excitation voltage (magnitude and phase). Therefore, the conversion factor between the electrical and the mechanical domain α can be determined as [Richter et al., 2009]

$$\alpha = \frac{r_{el}}{r_m}, \tag{3-50}$$

where r_m is the radius of the mechanical admittance frequency response circle.

3.4 Validation of the Analytical Model

In experimental work, piezoelectric bimorphs called "Piezo Bending Actuators 427.0085.11Z" from Johnson Matthey were used. A photo of this bimorph is shown in Figure 3-6 and its technical data are given in Table 3-2.

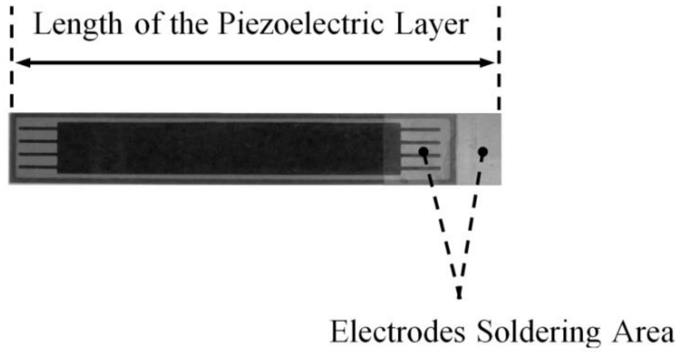

Figure 3-6 A photo of the top-view of the used bimorph (Piezo Bending Actuators 427.0085.11Z)

Table 3-2 Specifications of the used bimorph (geometry according to Figure 3-3)

Parameter	Symbol	Value
Total length of piezoelectric layers	l_b	45.00 ±0.1 mm
Beam width	w	7.20 ±0.1 mm
Total beam thickness	h	0.78 ±0.03 mm
Shim layer thickness	h_{sh}	0.28 ±0.05 mm
Piezoelectric layer density	ρ_p	8000 $\mathrm{kg/m^3}$
Shim layer density	ρ_{sh}	1800 $\mathrm{kg/m^3}$
Piezoelectric coupling factor	k_{31}	0.38
Piezoelectric compliance	s_{11}^E	15.8×10^{-12} $\mathrm{m^2/N}$
Piezoelectric dielectric constant	ε_{33}^T	61.95 $\mathrm{nF/m}$
Beam mechanical quality factor	Q_m	45
Shim layer modulus of elasticity	E_{sh}	120×10^9 $\mathrm{N/m^2}$

The bimorph was clamped between two aluminum bars using two screws to construct a cantilever beam as shown in Figure 3-7. The free length of the cantilever was repeatedly measured with a caliper gauge. The results deviated by about $\pm$ 0.1 mm, so the values given here are the averages.

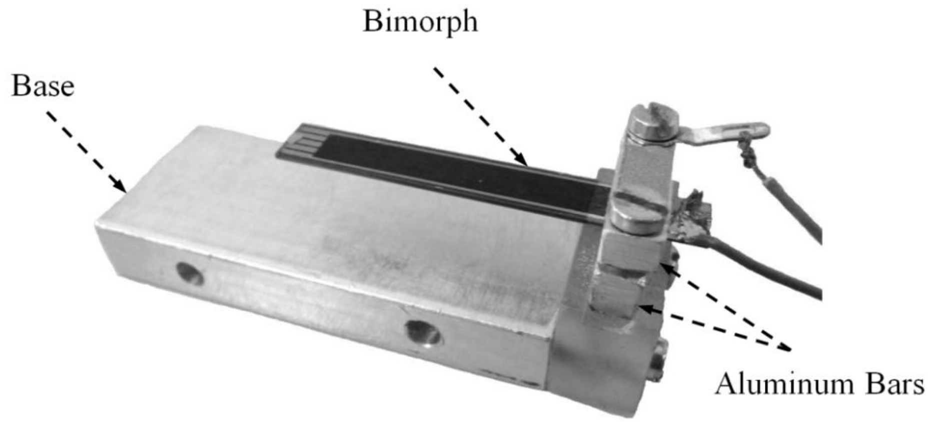

Figure 3-7 Piezoelectric cantilever (Typical piezoelectric harvester)

Impedance analyzer type HP 4192A was used to measure the electrical admittance of the piezoelectric cantilever across a certain range of the excitation frequencies. The resonance and the anti-resonance frequencies of the piezoelectric cantilever were identified from the measured admittance as introduced in section (3.3). Three bimorphs (nominally identical) were tested for different free lengths at an excitation level of 500 mV_{RMS}.

The measurements of the resonance frequencies with the corresponding lengths of the beam are shown in Figure 3-8. Additionally this figure includes the calculations of the resonance frequencies for three analytical models. The analytical models are: the proposed model “New Model”, the model introduced by Wang and Cross [1998] and the model developed by Richter et al. [2006]. Figure 3-8 clearly shows that the newly developed model gives significantly better estimates for the resonance frequency than previous models.

Figure 3-9 shows the measured anti-resonance frequencies with the corresponding lengths of the beam. Neither of the models introduced by Wang and Cross [1998] and Richter et al. [2006] includes the calculation of the anti-resonance frequency.

The New Model, as in model introduced by Richter et al. [2006], makes it possible to calculate the parameters of the Butterworth-Van-Dyke equivalent circuit, and thus enables a simulation of frequency sweeps of the admittance of piezoelectric elements, using Equation (3-12). For the clarity issue, Figure 3-10 and Figure 3-11 show the measured frequency sweeps of admittance magnitude and phase for only the first bimorph of the three which are used in the experimental work. These figures additionally contain the corresponding frequency sweeps calculated using the New Model and the model introduced by Richter et al. [2006]. Except for the maximum admittance value, the New Model fits the measurement better than the model introduced by Richter et al. [2006]. The experimental results show that the capacitance of the bimorph as calculated by the new model is about 25% larger than the real capacitance. This difference is the main reason for the over-estimation of the admittance and it occurs due to ignoring the internal resistance of the piezoelectric bimorph.

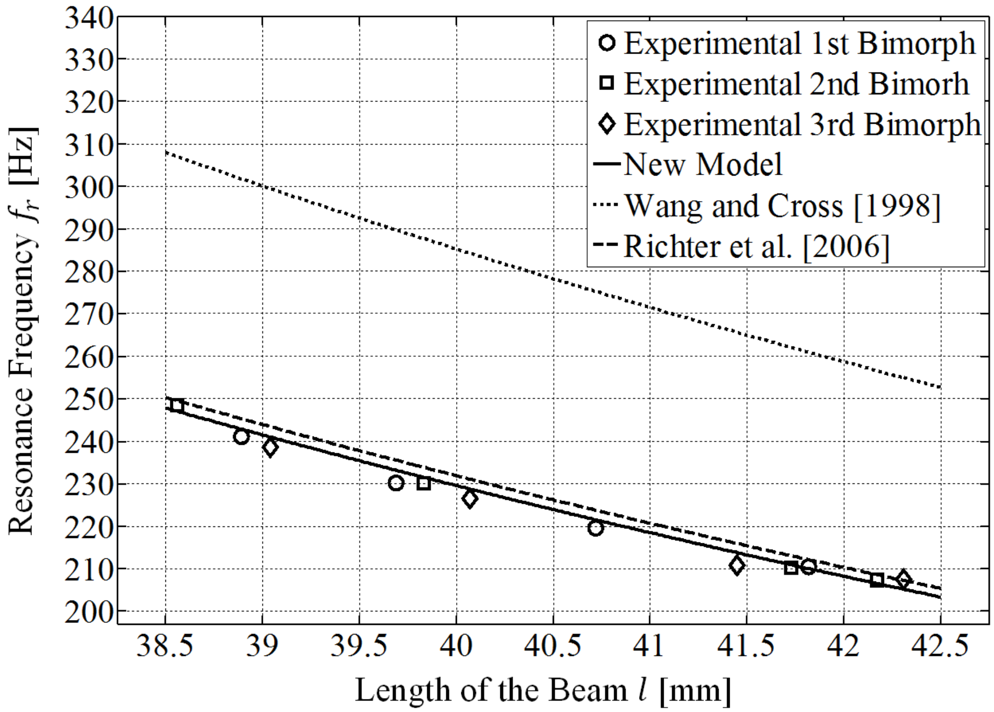

Figure 3-8 Comparison of measured and calculated resonance frequencies

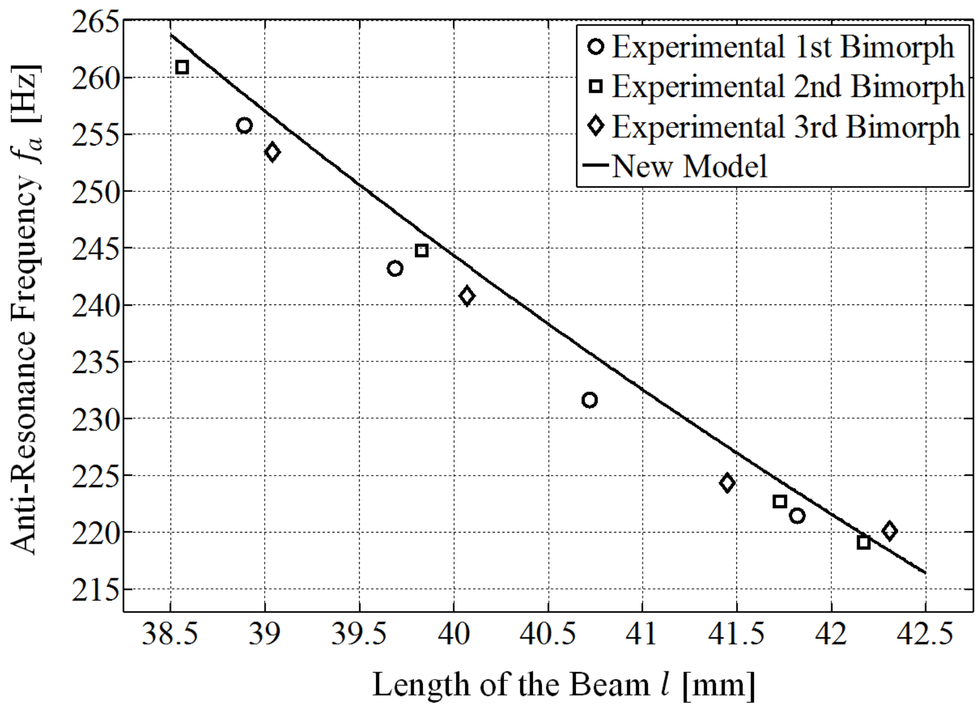

Figure 3-9 Comparison of measured and calculated anti-resonance frequencies

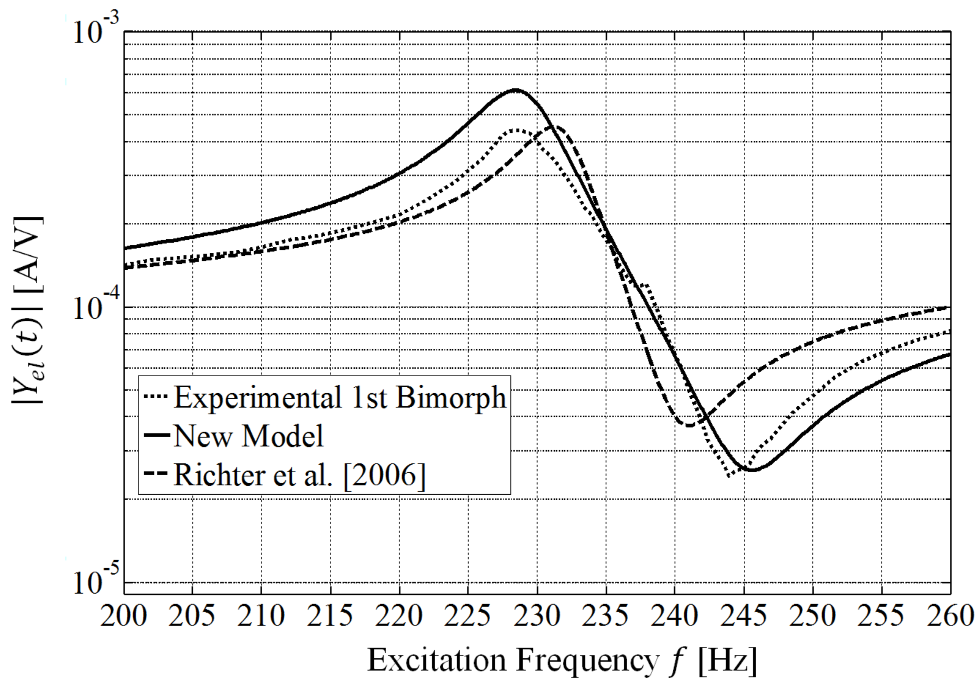

Figure 3-10 Comparison of measured and calculated frequency sweeps of admittance magnitude for the first bimorph

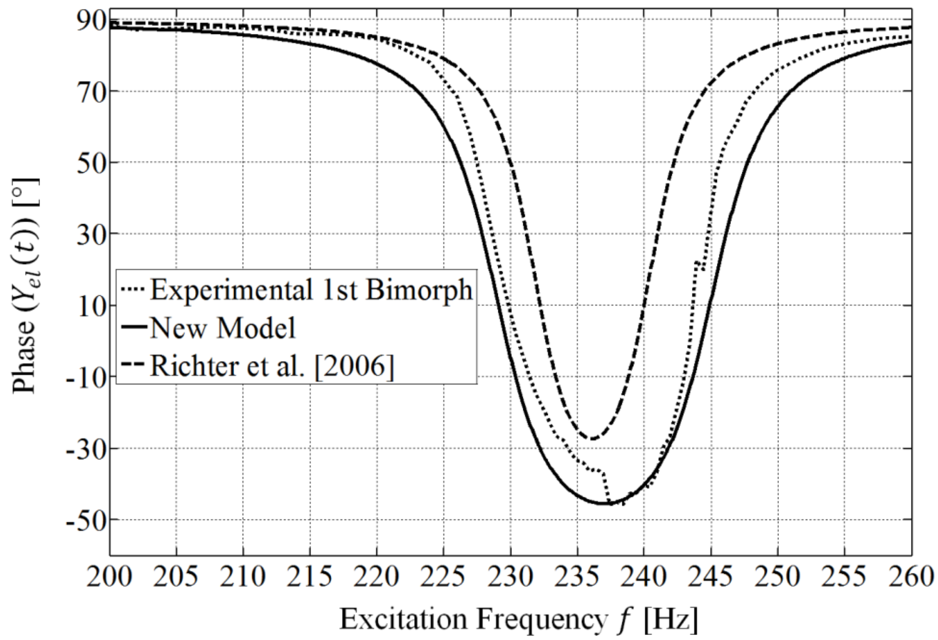

Figure 3-11 Comparison of measured and calculated frequency sweeps of admittance phase for the first bimorph

One of the great advantages of analytical modeling is the possibility of doing parameter studies with very little effort. For example, Figure 3-12 and Figure 3-13 theoretically show the influence of the manufacturing tolerances for beam thickness and shim layer thickness (given in Table 3-2) on the resonance and anti-resonance frequencies: the resonance and anti-resonance frequencies change by about 0.16 Hz per 1 µm change in beam thickness and by about 0.31 Hz per 1 µm change in shim layer thickness. Thus, based on simulations, the effect of the manufacturing tolerances for individual bimorphs can be predicted and countered constructively.

Other possible causes for deviations between model and experiment are the assembly of the structure, i.e. clamping of the cantilever, and inaccurate measurement of its length. In most setups, the free length of the piezoelectric bimorph does not depend on manufacturing tolerances of the bimorph, but rather is determined during assembly. How exactly the free length can be adjusted depends on the assembly and accuracy of measurement. In many cases, these factors lead to even higher inaccuracy than the manufacturing tolerances.

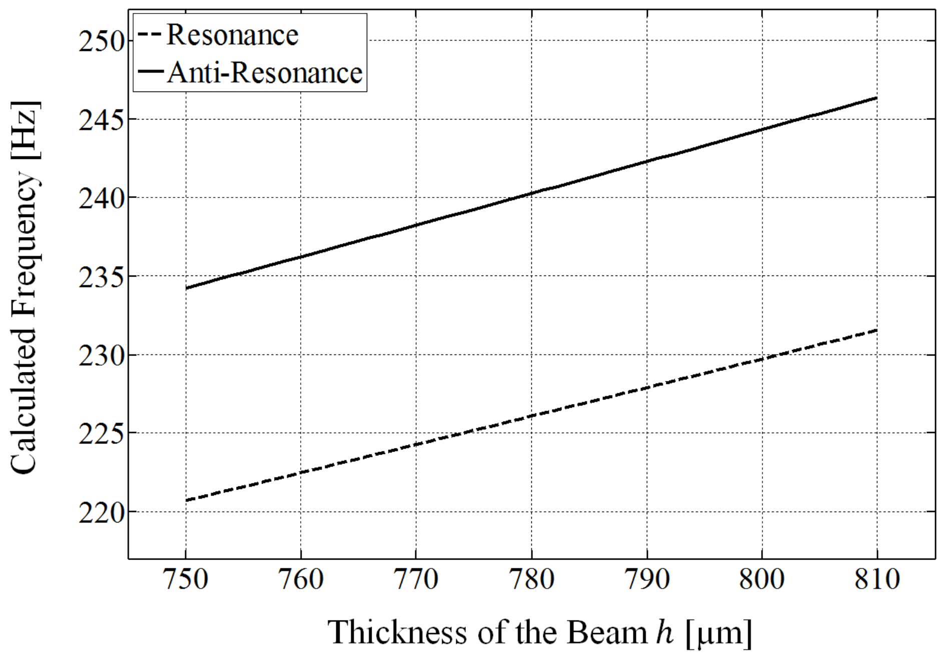

Figure 3-12 Effect of beam thickness manufacturing tolerances on characteristic frequencies

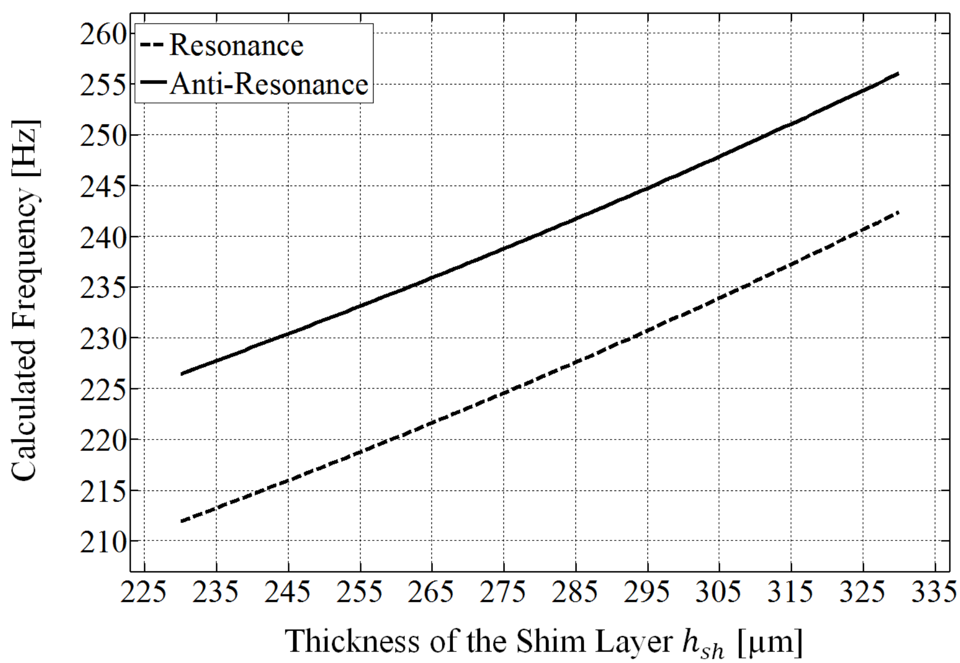

Figure 3-13 Effect of shim layer thickness manufacturing tolerances on characteristic frequencies

4 Modeling of the Basic Autonomous System

In this chapter, a model is derived which describes the operation of a typical autonomous system with piezoelectric harvester. Such a system consists of two main parts: the electromechanical part (piezoelectric harvester) and the electrical part. Generally, the electrical part determines the performance of the piezoelectric harvester. Therefore, the electrical part is analyzed first; then the piezoelectric harvester is modeled.

The system modeled here is also investigated experimentally and good correlation is found between the theoretical and the experimental results: In steady-state operation, the piezoelectric harvester experiences two alternating load conditions because of the electrical part. These loading conditions can considerably impair the harvester operation and cause the system to behave nonlinearly.

4.1 Elements of the Basic Autonomous Systems

The basic configuration of an autonomous system typically contains three elements in addition to the piezoelectric harvester: a full-wave rectifier, a reservoir capacitor and an electronic device which has a task to perform (e.g., a temperature sensor), as shown in Figure 4-1. Here, this system is called a Basic Autonomous System or simply "BAS".

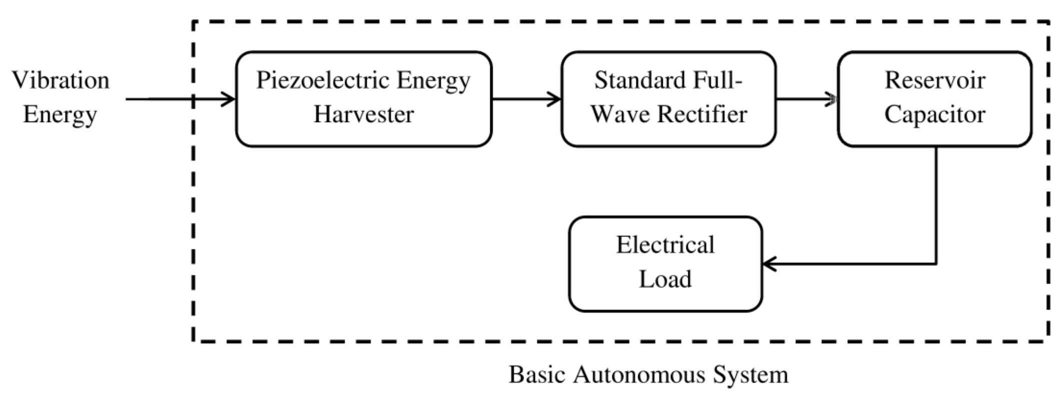

Figure 4-1 Configuration of the Basic Autonomous System (BAS)

As can be seen in Figure 4-2, the standard full-wave rectifier is a diode bridge circuit which is used to convert the AC voltage $u(t)$ generated by a typical piezoelectric harvester into DC voltage U_{dc}. This DC voltage U_{dc} is used to power an electronic device, which is represented here by the resistive load R_l. The reservoir capacitor C_R is used to smooth the output DC voltage.

The reservoir capacitor stores the electrical energy supplied by the harvester; it then releases some of this energy in order to power the connected electronic device for those time intervals when the harvester is not supplying any energy. This may be due to the nature of the generated energy and/or due to the rectification process (diode barrier voltage).

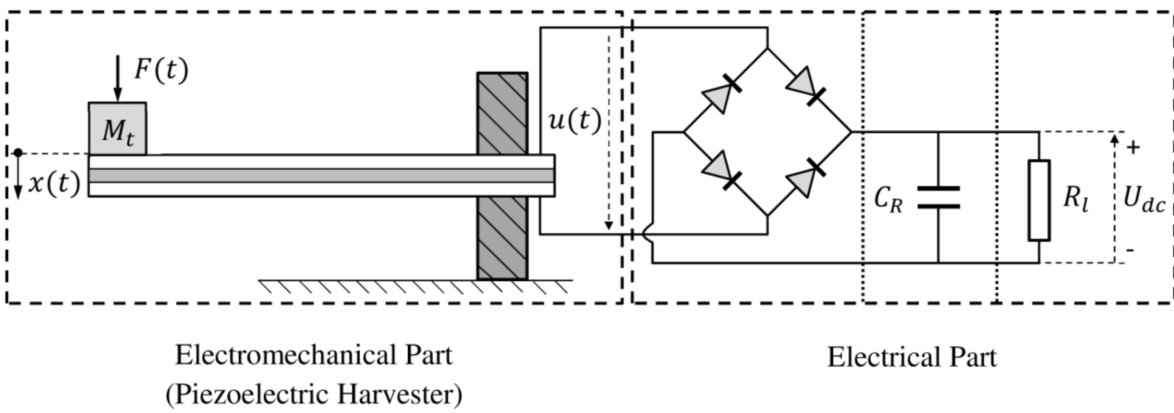

Figure 4-2 Schematic of a Basic Autonomous System

Figure 4-2 shows that the BAS has two main parts: the electromechanical (piezoelectric harvester) and electrical parts. In the next section, these parts are analyzed separately in order to investigate their influences on each other. Another benefit of this modular model is that the parts can be exchanged easily.

4.2 The Electrical Part

The electrical part of the BAS must be analyzed first because it determines the performance of the piezoelectric harvester.

4.2.1 Principle of Operation

The electrical representation of the entire autonomous system is shown in Figure 4-3. The electrical part of the BAS consists of three elements: a full-wave rectifier circuit, a reservoir capacitor and a connected load. The rectifier circuit consists of four diodes: D_1, D_2, D_3 and D_4. The piezoelectric harvester (represented here by the voltage $u(t)$) is assumed to generate a harmonic AC voltage which is expressed by

$$u(t) = U_0 \sin \omega t\ , \tag{4-1}$$

where U_0 is the amplitude of the generated voltage, t is the time and ω is the frequency of the excitation (force or acceleration). The corresponding output DC voltage U_{dc} can be calculated as [Jaeger and Blalock, 2011]

$$U_{dc} = U_0 - 2U_d\ , \tag{4-2}$$

where U_d the barrier voltage of the diode which is the voltage drop across the diode in order to be conductive.

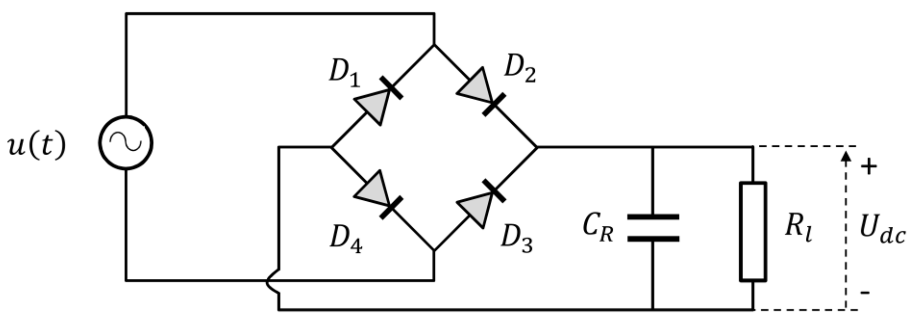

Figure 4-3 Electrical part of a basic autonomous system

Figure 4-4a shows the generated voltage $u(t)$ for the first two periods of operation of the harvester, where t_p is the period. The corresponding output DC voltage is shown in Figure 4-4b. These two figures (Figure 4-4a and Figure 4-4b) show that the first period of operation is very important and it includes four time intervals. These time intervals are: the dead zone time interval t_0, the diode transient conduction time interval t_{tr}, the open-circuit time interval t_{op} and finally the diode steady-state conduction time interval t_{ss}. These time intervals are dependent on the characteristics of the components of the BAS.

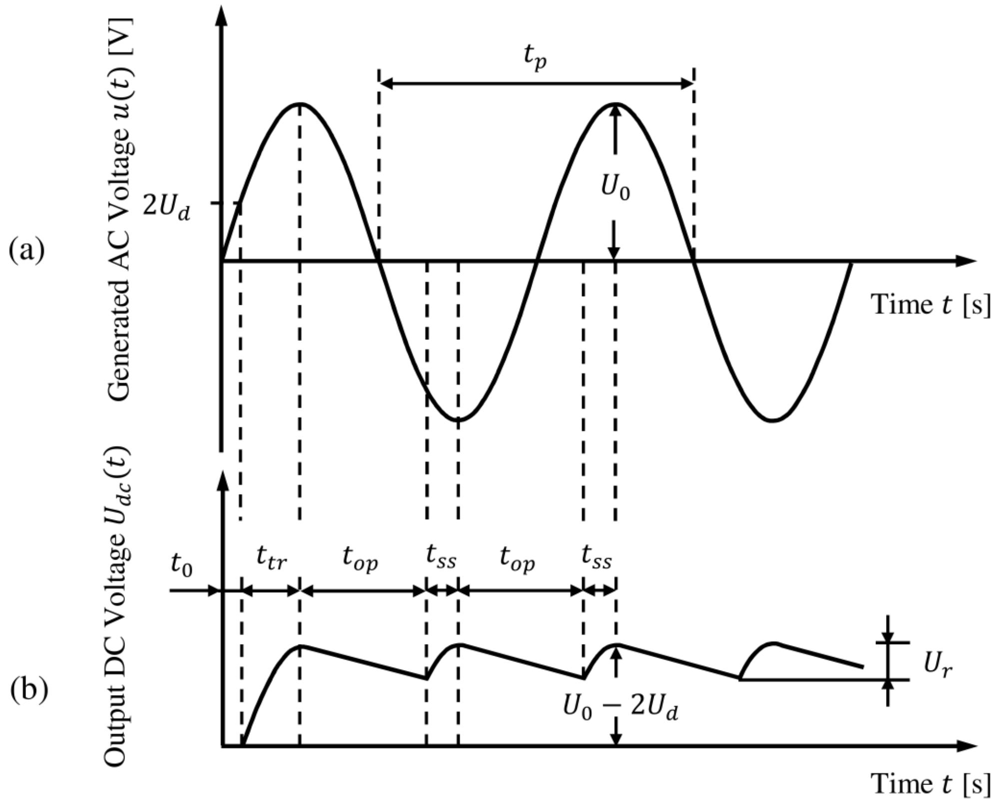

Figure 4-4 (a) Applied AC voltage $u(t)$ and (b) the output DC voltage across the connected load $U_{dc}(t)$

The rectification process starts when the dead zone time interval ends. This time interval is defined as that time interval during which the AC voltage is applied and the output DC voltage is zero. The dead zone time interval occurs because the magnitude of the generated AC voltage $|u(t)|$ is less than the voltage U_d. In a full-wave rectifier, two diodes must be conductive in order to allow the current to flow through the circuit. This causes the amount of the generated voltage to drop by $2U_d$.

In a well-designed system, the dead zone time interval t_0 exists only in the first quarter of the first period of operation, as shown in Figure 4-4b. This is because the reservoir capacitor C_R will have already stored some energy and can supply output DC voltage during periods of time when the harvester is not delivering voltage.

The transient conduction time interval t_{tr} starts when the magnitude of the generated AC voltage $|u(t)|$ rises to be greater than the barrier voltages of the diodes $2U_d$ (two diodes), signaling the end of the dead zone time interval. Within this time interval, either the first pair of diodes (D_2 and D_4) is on and the other pair (D_1 and D_3) is off or vice-versa. This causes the current to flow from the harvester into the parallel loads C_R and R_l. The size of the reservoir capacitor C_R should be calculated carefully so that it is fully charged at the end of this time interval; otherwise, the transient conduction time will continue over into the next period until the capacitor is fully charged and will have a voltage of magnitude equal to ($U_0 - 2U_d$).

After that, when the applied AC voltage magnitude $|u(t)|$ becomes less than the capacitor voltage, the diodes are then off because the capacitor is attempting at that point to discharge its stored energy through them in their reverse direction. This means the harvester is now disconnected from the load side, i.e. it is in open-circuit condition. This happens in a time interval called the open-circuit time interval t_{op}. In this time interval, the load R_l is electrically powered by only the energy stored in the capacitor.

When the capacitor voltage becomes smaller than the magnitude of the applied AC voltage $|u(t)|$, t_{op} has ended and the steady-state conduction time interval t_{ss} starts. During this time interval, the other pair of diodes (those which were not conducting earlier) begins to conduct and the first conducting pair is no longer doing so. During this time interval, the capacitor has time to recharge again.

The second period (and also all the following periods) of operation consists only of the open-circuit time interval t_{op} and the steady-state conduction time interval t_{ss} of the diodes, i.e. the system operates in steady state condition as shown in Figure 4-4b.

4.2.2 Time Intervals of Operation

Referring back to Figure 4-4b, the transient conduction time interval can be expressed as

$$t_{tr} = \frac{t_p}{4} - t_0 \,. \tag{4-3}$$

The dead zone time interval is the time required for the generated voltage magnitude $|u(t)|$ to reach the value of the voltage drop across the diodes. Mathematically, this can be done by setting Equation (4-1) equal to $2U_d$ and setting $t = t_0$:

$$u(t_0) = U_0 \sin \omega t_0 = 2U_d \,. \tag{4-4}$$

By simplifying Equation (4-4) and solving for t_0, the dead zone time interval can be expressed as

$$t_0 = \frac{1}{\omega} \arcsin\left(\frac{2U_d}{\hat{u}}\right). \tag{4-5}$$

When the transient conduction time interval t_{tr} has ended, the open-circuit time interval t_{op} begins. In this time interval, the harvester experiences an open-circuit condition and is disconnected from the electrical load R_l, which operates by consuming the energy stored in the reservoir capacitor C_R. Based on Figure 4-4b, the open-circuit time interval t_{op} can be expressed as

$$t_{op} = \frac{t_p}{2} - t_{ss} \,. \tag{4-6}$$

The steady state conduction time interval t_{ss} for a full wave rectifier can be expressed as [Jaeger and Blalock, 2011]

$$t_{ss} = \frac{1}{\omega} \sqrt{\frac{2U_r}{U_0}} \,, \tag{4-7}$$

where U_r is the ripple voltage as shown in Figure 4-4b; it can be calculated as [Jaeger and Blalock, 2011]

$$U_r \approx \frac{t_p(U_0 - 2U_d)}{2R_l C_R} \,. \tag{4-8}$$

Equation (4-8) shows that the ripple voltage U_r is inversely proportional with the size of the reservoir capacitor C_R.

4.3 Electrical Representation of the BAS

It is concluded from the previous section that the piezoelectric harvester experiences different loading conditions depending on which time interval it is operating in. It is desirable to determine these loading conditions in order to be able to predict the performance of the harvester during the operation. The loading conditions can be determined by further analyzing the electrical part of the autonomous system.

Jaeger and Blalock [2011] represented the diode by the circuit shown in Figure 4-5, where the resistance R_d is the bulk resistance of the diode, U_d is the dropped voltage across the diode and i_d the current flowing across the diode.

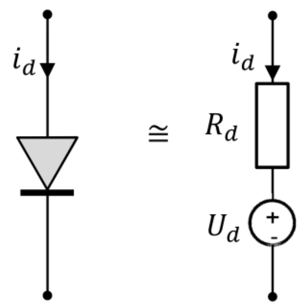

Figure 4-5 Equivalent circuit of a diode

Based on the electrical presentation of the diode, the basic autonomous system can be presented by the circuit shown in Figure 4-6. In this circuit, $U_n(t)$ is the net applied voltage and S is an electrical switch. The net voltage $U_n(t)$ includes the drops of the voltage resulting from diodes. Furthermore, the state of the electrical switch (open or closed) depends on within which time interval the harvester is currently operating.

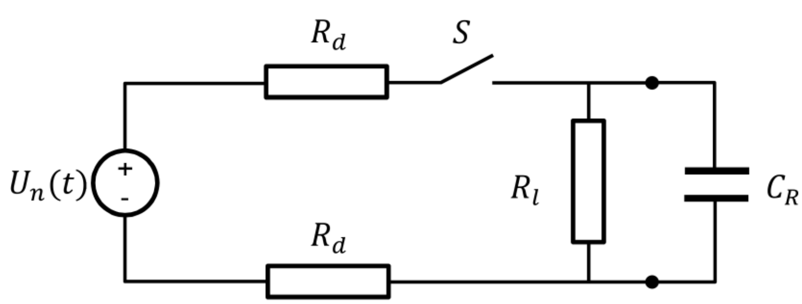

Figure 4-6 Equivalent electrical circuit

4.3.1 Charging Time Constant of the Reservoir Capacitor

In the transient conduction time interval t_{tr} the electrical switch S shown in Figure 4-6 is closed for the first time and the reservoir capacitor has no stored electrical energy. The equivalent circuit is as shown in Figure 4-7, where $U_n(t)$ is assumed to be constant of magnitude equal to U within this time interval.

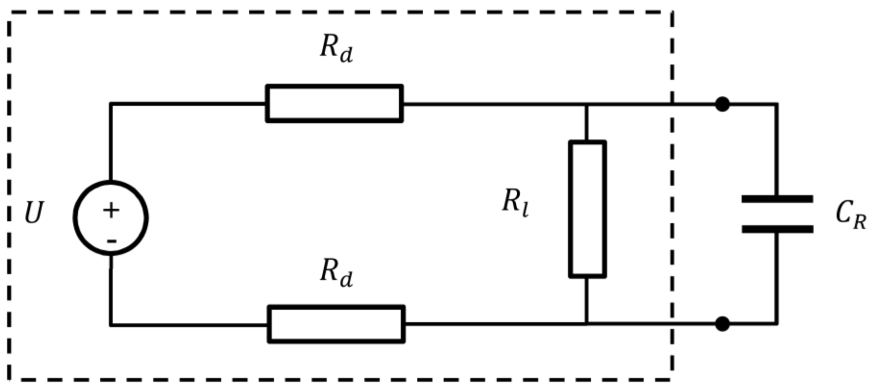

Figure 4-7 Equivalent circuit in transient conduction time interval

Thevenin's theorem is one possible technique that can be used to calculate the increase of the reservoir capacitor voltage. This theorem states that any circuit includes a voltage source (sources) and resistances, such as those shown in Figure 4-7 (inside box), which can be replaced by a single voltage source U_{Th} and single resistor R_{Th} in series as shown in Figure 4-8. [Alexander and Sadiku, 2006]

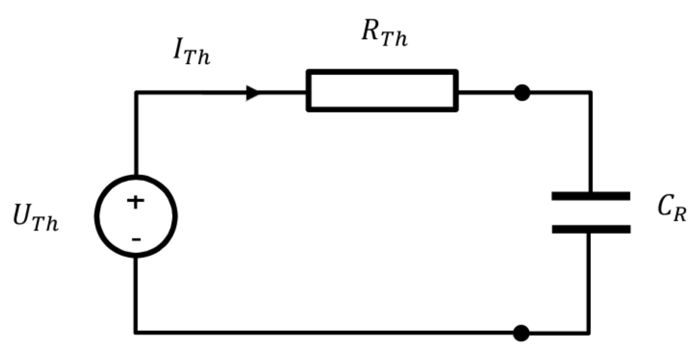

Figure 4-8 Equivalent circuit obtained using Thevenin's theorem

The procedure to calculate the voltage and resistance according to Thevenin's theorem consists of two steps, the first of which is to short-circuit the terminal of the reservoir capacitor C_R and then calculate the total current I_{Th} flowing in the resulting circuit [Alexander and Sadiku, 2006]. This is found to be

$$I_{Th}(t) = \frac{U}{2R_d}\,. \tag{4-9}$$

The second step is to remove the reservoir capacitor and to leave its branch open, and to then calculate the voltage across this branch. This is known as Thevenin's voltage source and it is calculated as

$$U_{Th} = \left(\frac{R_l}{R_l + 2R_d}\right) U\,. \tag{4-10}$$

The equivalent Thevenin's resistance R_{Th} can be found by using the equation

$$R_{Th} = \frac{U_{Th}}{I_{Th}} = \frac{2R_d R_l}{R_l + 2R_d}\,. \tag{4-11}$$

Generally, the bulk diode resistance R_d does not exceed $(R_d)_{max} = 2\Omega$ at room temperature for all the diode types used in rectifying circuits.The connected load R_l is also usually much greater than this value, i.e. $R_d \ll R_l$. This means that Equation (4-10) and Equation (4-11) can be approximated to get

$$U_{Th} \approx U \tag{4-12}$$

and

$$R_{Th} \approx 2R_d\,. \tag{4-13}$$

Thus, the equivalent circuit within the charging time interval can be reduced to that shown in Figure 4-9. $q_{ch}(t)$ is the electrical charge during the capacitor charging time interval.

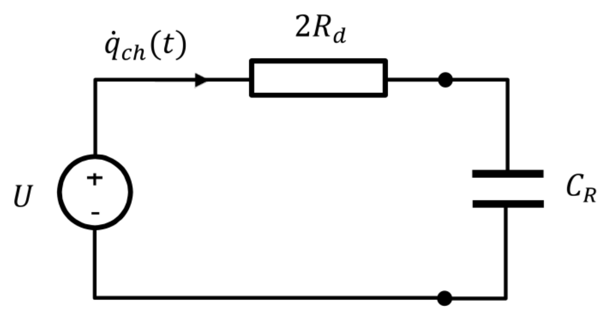

Figure 4-9 Equivalent circuit of BAS while capacitor is charging

Applying Kirchhoff's voltage law to the equivalent circuit shown in Figure 4-9 gives

$$U - 2R_d \frac{dq_{ch}(t)}{dt} - \frac{q_{ch}(t)}{C_R} = 0\,. \tag{4-14}$$

If the capacitor initially has no electrical charge, i.e. $q_{ch}(0) = 0$, then the solution of Equation (4-14) is found to be

$$q_{ch}(t) = UC_R\left[1 - e^{-(t/t_{ch})}\right]. \tag{4-15}$$

Thus, the charging current flowing into the capacitor is

$$I_{ch}(t) = \frac{U}{2R_d} e^{-(t/t_{ch})} \tag{4-16}$$

and the voltage across the capacitor is given by

$$U_{ch}(t) = U\left[1 - e^{-(t/t_{ch})}\right], \tag{4-17}$$

where

$$t_{ch} = 2R_d C_R\,. \tag{4-18}$$

Here, it is desirable to fully charge the reservoir capacitor within the transient conduction time t_{tr}. This minimizes the time of the transient operation with a smaller ripple in the output DC voltage. The typical curve of the voltage increase across the capacitor is shown in Figure 4-10. This figure shows that when the time t reaches five times the charging constant t_{ch}, the voltage across the capacitor is almost equal to the input voltage U.

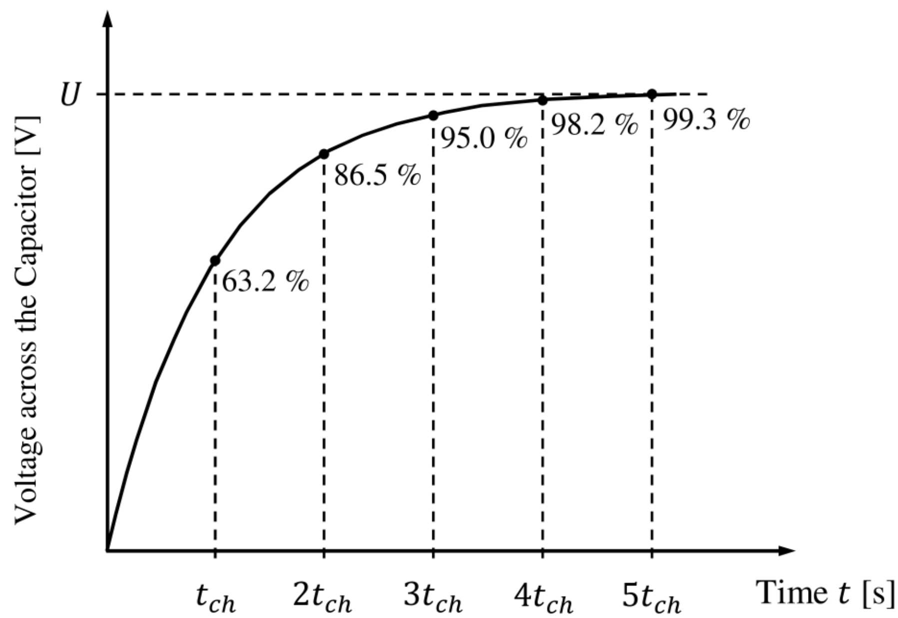

Figure 4-10 Typical voltage variation for a charging capacitor

Therefore, the proper capacitor should fulfill the following condition:

$$t_{tr} = 5t_{ch} \, . \tag{4-19}$$

Substituting Equations (4-3) and (4-5) into Equation (4-19) shows that the required reservoir capacitor size can be expressed as

$$C_R = \frac{t_p}{20\pi R_d}\left[\frac{\pi}{2} - \arcsin\left(\frac{2U_d}{U_0}\right)\right] . \tag{4-20}$$

Equation (4-20) can be used to show that the reservoir capacitor required depends on the amplitude of the generated voltage U_0. Normally, the electronic device attached to the BAS requires the DC voltage to maintain a certain value in order to operate. This required DC voltage must be equal to the generated AC voltage amplitude minus the voltage drops across the diodes. For example, a temperature sensor requires a voltage supply of 1.5 V and if the diodes used both have a 0.49 V barrier voltage, then the generated voltage amplitude should be 2.48 V in order to provide the required DC voltage.

4.3.2 Discharging Time Constant of the Reservoir Capacitor

At this point, the reservoir capacitor C_R has lost a certain amount of its stored energy, which has been consumed by the connected load R_l. To determine the amount lost, the time required for discharging the capacitor must first be found. This can be achieved by using the Kirchhoff voltage law for the capacitor and resistor loop shown in Figure 4-6, when the switch S is open, assuming that the capacitor is fully charged. This result in

$$\frac{q_{dis}(t)}{C_R} - I_{dis}R_l = 0, \tag{4-21}$$

where $q_{dis}(t)$ is the electrical charge across the capacitor during the discharging time interval and I_{dis} is the discharging current and is given by

$$I_{dis}(t) = -\frac{dq_{dis}(t)}{dt}. \tag{4-22}$$

The minus sign refers to the fact that the capacitor is losing charge. Substituting Equation (4-21) into Equation (4-22) gives the following relationship:

$$\frac{dq_{dis}(t)}{q_{dis}(t)} = -\frac{dt}{R_l C_R}. \tag{4-23}$$

Integrating both sides of Equation (4-23) with $q_{dis}(0) = q_0$ results in

$$q_{dis}(t) = q_0 e^{-(t/t_{dis})}, \tag{4-24}$$

where

$$t_{dis} = R_l C_R\,. \tag{4-25}$$

It can now be concluded from Equations (4-18) and (4-25) that the charging time constant of the reservoir capacitor t_{ch} is much smaller than its discharging time constant t_{dis}. This is because the diode bulk resistance is much smaller than the connected load ($R_d \ll R_l$), meaning that the reservoir capacitor C_R is almost full in the conduction time interval during the steady-state operation, thereby the harvester powers mainly the connected load. Therefore the piezoelectric harvester experiences two alternating load conditions due to the rectification process: one is resistive-load condition and the other is open-circuit condition.

4.4 Electromechanical Part (Piezoelectric Harvester)

It was discussed in the previous section that the piezoelectric harvester experiences two alternating loading conditions during steady-state operation due to the rectification process. If the harvester generates voltages with different characteristics (magnitudes and phases) under these loading conditions, then the harvester generates a non-harmonic voltage, i.e. the harvester becomes a nonlinear system. Therefore, it is desirable to model the generated voltage under each of these loading conditions in order to predict the response of the piezoelectric harvester. As mentioned above, these loading conditions are the resistive load and the open-circuit conditions.

Before continuing with the system analysis, it is important to mention that the data for the piezoelectric element used in both the modeling process and in the experiments is the same as that given in Table 3-2. Such an element has low damping, as do most of those elements used for energy harvesting applications. Therefore, its characteristic frequencies can be approximately represented by the resonance and anti-resonance frequencies according to the assumptions in IEEE [1969], given before in Equation (3-16) and Equation (3-17).

4.4.1 Resistive-Load Condition

Resistive-load condition refers to the condition in which the electrodes of the piezoelectric element in a harvester are connected via a resistive load R_l as shown in Figure 4-11.

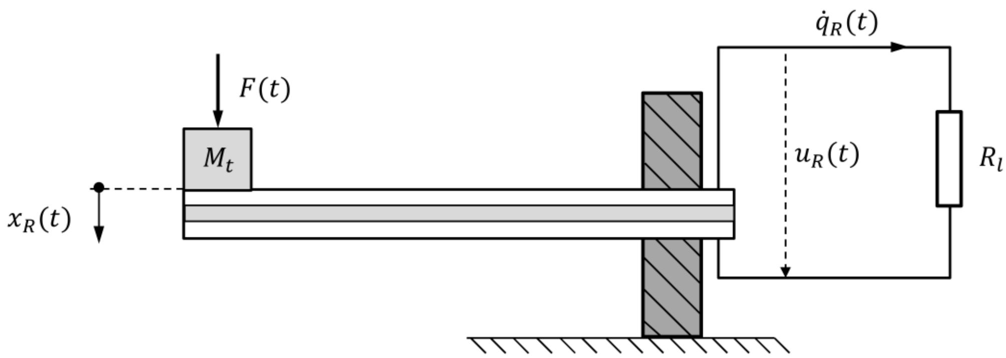

Figure 4-11 Piezoelectric harvester connected to a resistive load

All the parameters of the systems are as defined previously. $x_R(t)$ is the beam deflection. $u_R(t)$ and $q_R(t)$ are the generated voltage and charge across the connected resistive load. The force $F(t)$ can be an externally applied force or an equivalent force resulting from acceleration which is assumed to be a harmonic force described by

$$F(t) = F_0 \sin \omega t \,. \tag{4-26}$$

If the system is linear, then the generated AC voltage $u_R(t)$ can be expressed as

$$u_R(t) = U_R \sin\left(\omega t + \varphi_{u_R}\right), \tag{4-27}$$

where ω is the excitation frequency of the force $F(t)$ in rad/s, F_0 and U_R are the amplitudes of the excitation force and the generated AC voltage, and φ_{u_R} is the phase difference between them.

Using the lumped-parameters model introduced in Section (2.4.1), the mechanical equivalent system of the piezoelectric harvester under resistive-load condition can be obtained, as shown in Figure 4-12a. From applying the analogies between the mechanical and the electrical variables, the equivalent electrical system of the piezoelectric harvester also under resistive-load condition can represented by the circuit shown in Figure 4-12b. Similar equivalent systems can be found in Richter [2010].

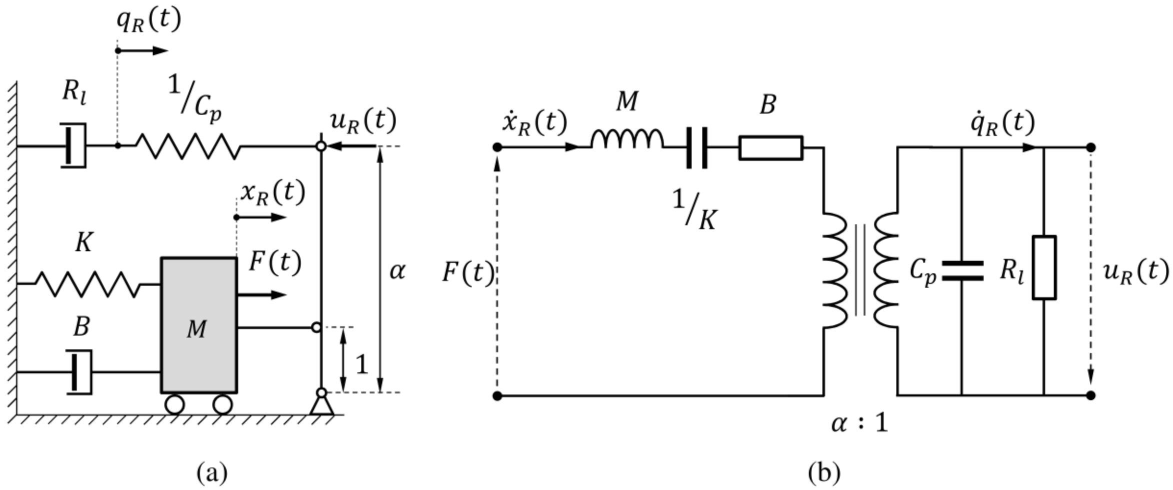

Figure 4-12 Equivalent systems of the piezoelectric harvester in resistive load condition (a) mechanical and (b) electrical

At this point, the first goal is to calculate the generated voltage as a function of the connected load R_l and the excitation frequency of the external force ω, and then to derive the relationship between these two variables in order to determine the conditions at which the maximum voltage can be generated. The governing equation of such a system is

$$M\ddot{x}_R(t) + B\dot{x}_R(t) + Kx_R(t) = F(t) - \alpha u_R(t). \quad (4\text{-}28)$$

For the electrical side

$$\alpha\dot{x}_R(t) = C_p\dot{u}_R(t) + \dot{q}_R(t) \quad (4\text{-}29)$$

and

$$\dot{q}_R(t) = \frac{u_R(t)}{R_l}. \quad (4\text{-}30)$$

Applying the Laplace transform to Equations (4-28), (4-29) and (4-30) for zero initial conditions results in:

$$[Ms^2 + Bs + K]\hat{X}_R(s) = \hat{F}(s) - \alpha\hat{U}_R(s), \quad (4\text{-}31)$$

$$\alpha\hat{X}_R(s) = C_p\hat{U}_R(s) + \hat{Q}_R(s) \quad (4\text{-}32)$$

and

$$s\hat{Q}_R(s) = \frac{\hat{U}_R(s)}{R_l}. \tag{4-33}$$

$\hat{F}(s)$, $\hat{X}_R(s)$, $\hat{U}_R(s)$ and $\hat{Q}_R(s)$ are the Laplace transforms of the excitation force, harvester deflection, generated AC voltage and generated charge respectively. Based on Equations (4-31), (4-32) and (4-33), the piezoelectric harvester in a resistive load condition is presented by the block diagram shown in Figure 4-13.

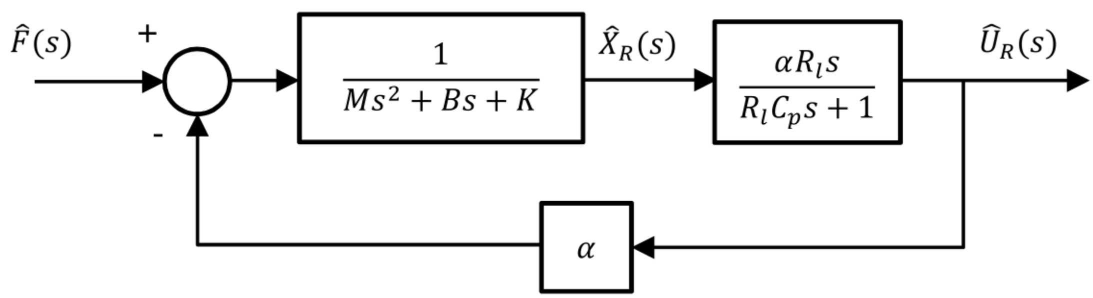

Figure 4-13 Block diagram of a piezoelectric harvester under resistive-load condition

The transfer function of the block diagram shown in Figure 4-13 is

$$\frac{\hat{U}_R(s)}{\hat{F}(s)} = \frac{\alpha R_l s}{MR_lC_ps^3 + \left(M + BR_lC_p\right)s^2 + \left(B + KR_lC_p + \alpha^2 R_l\right)s + K}. \tag{4-34}$$

In terms of resonance frequency ω_r, anti-resonance frequency ω_a and damping ratio ζ, Equation (4-34) can be rewritten as

$$\frac{\hat{U}_R(s)}{\hat{F}(s)} = \frac{(\alpha R_l/M)\ s}{R_lC_ps^3 + \left(1 + 2\zeta\omega_r R_lC_p\right)s^2 + \left(2\zeta\omega_r + \omega_a^2 R_lC_p\right)s + \omega_r^2}, \tag{4-35}$$

where (from Chapter 3)

$$\omega_r = \sqrt{\frac{K}{M}}, \tag{4-36a}$$

$$\omega_a = \sqrt{\omega_r^2 + \frac{\alpha^2}{MC_p}}\,, \tag{4-36b}$$

and

$$\zeta = \frac{B}{2M\omega_r}\,. \tag{4-36c}$$

The sinusoidal form of this transfer function is

$$\frac{\hat{U}_R(j\omega)}{\hat{F}(j\omega)} = \frac{j(\alpha R_l \omega/M)}{\left[\omega_r^2 - \left(1 + 2\zeta\omega_r R_l C_p\right)\omega^2\right] + j\omega\left[2\zeta\omega_r + R_l C_p(\omega_a^2 - \omega^2)\right]}\,. \tag{4-37}$$

This gives the amplitude of the generated AC voltage as

$$U_R = \frac{(\alpha R_l \omega/M)\,F_0}{\sqrt{\left[\omega_r^2 - \left(1 + 2\zeta\omega_r R_l C_p\right)\omega^2\right]^2 + \omega^2\left[2\zeta\omega_r + R_l C_p(\omega_a^2 - \omega^2)\right]^2}} \tag{4-38}$$

and the phase difference as

$$\varphi_{u_R} = \frac{\pi}{2} - \arctan\left(\frac{\omega\left[2\zeta\omega_r + R_l C_p(\omega_a^2 - \omega^2)\right]}{\omega_r^2 - \left(1 + 2\zeta\omega_r R_l C_p\right)\omega^2}\right). \tag{4-39}$$

From Equation (4-2), the generated DC voltage U_{dc} can be expressed as

$$U_{dc} = U_R - 2U_d\,. \tag{4-40}$$

Referring to Figure 4-13, the transfer function between the excitation force $\hat{F}(s)$ and the deflection $\hat{X}_R(s)$ is

$$\frac{\hat{X}_R(s)}{\hat{F}(s)} = \frac{\left(R_l C_p s + 1\right)}{MR_l C_p s^3 + \left(M + BR_l C_p\right)s^2 + \left(B + KR_l C_p + \alpha^2 R_l\right)s + K}\,. \tag{4-41}$$

Applying the same procedure and simplifications used before yields the system sinusoidal transfer function:

$$\frac{\hat{X}_R(j\omega)}{\hat{F}(j\omega)} = \frac{\left[\left(1 + jR_lC_p\omega\right)/M\right]}{\left[\omega_r^2 - \left(1 + 2\zeta\omega_r R_l C_p\right)\omega^2\right] + j\omega\left[2\zeta\omega_r + R_l C_p(\omega_a^2 - \omega^2)\right]}. \tag{4-42}$$

The deflection $x_R(t)$ can be expressed as

$$x_R(t) = X_R \sin\left(\omega t + \varphi_{x_R}\right), \tag{4-43}$$

where X_R and φ_{x_R} are the amplitude of the deflection and phase difference between the deflection $x_R(t)$ and the force $F(t)$. From Equation (4-42), the amplitude X_R can be expressed as

$$X_R = \frac{F_0}{M}\sqrt{\frac{\left[1 + \left(R_l C_p \omega\right)^2\right]}{\left[\omega_r^2 - \left(1 + 2\zeta\omega_r R_l C_p\right)\omega^2\right]^2 + \omega^2\left[2\zeta\omega_r + R_l C_p(\omega_a^2 - \omega^2)\right]^2}}. \tag{4-44}$$

The phase difference φ_{x_R} can be expressed as

$$\varphi_{x_R} = \arctan\left(R_l C_p \omega\right) - \arctan\left(\frac{\omega\left[2\zeta\omega_r + R_l C_p(\omega_a^2 - \omega^2)\right]}{\omega_r^2 - \left(1 + 2\zeta\omega_r R_l C_p\right)\omega^2}\right). \tag{4-45}$$

4.4.2 Open-Circuit Condition

The open-circuit condition refers to a condition in which nothing is connected between the electrodes of the piezoelectric harvester. Thus, if the system is linear and the force $F(t)$ is harmonic (see Equation (4-26)), then the generated voltage at open-circuit condition $u_{oc}(t)$ can be expressed as

$$u_{oc}(t) = U_{oc} \sin\left(\omega t + \varphi_{u_{OC}}\right), \tag{4-46}$$

where U_{OC} is the amplitude of the generated AC voltage at open-circuit condition and φ_{u_O} is the phase difference between the generated voltage $u_{oc}(t)$ and the force $F(t)$. This amplitude can be obtained from

$$U_{oc} = \lim_{R_l \to \infty} U_R\,. \tag{4-47}$$

Substituting Equation (4-38) into Equation (4-47), and then solving the obtained equation to find that the amplitude U_{oc} can be expressed as

$$U_{oc} = \frac{\left(\alpha / MC_p\right)F_0}{\sqrt{(\omega_a^2 - \omega^2)^2 + (2\zeta\omega_r\omega)^2}} \,. \tag{4-48}$$

The phase difference $\varphi_{u_{oc}}$ can be also calculated from

$$\varphi_{u_{oc}} = \lim_{R_l \to \infty} \varphi_{u_R} \,. \tag{4-49}$$

Substituting Equation (4-39) into Equation (4-49) and simplifying the obtained equation give that the phase difference $\varphi_{u_{oc}}$ can be expressed as

$$\varphi_{u_{oc}} = \frac{\pi}{2} + \arctan\left(\frac{\omega_a^2 - \omega^2}{2\zeta\omega_r\omega}\right). \tag{4-50}$$

The excitation frequency at which the harvester generates the maximum voltage under open-circuited conditions $\omega_{oc,opt}$ can be found by applying

$$\left.\frac{dU_{oc}}{d\omega}\right|_{\omega=\omega_{oc,opt}} = 0 \tag{4-51}$$

resulting in

$$\omega_{oc,opt} = \sqrt{\omega_a^2 - 2\zeta^2\omega_r^2} \,. \tag{4-52}$$

For systems with low damping ($\zeta \ll 1$), Equation (4-52) can be approximated as

$$\omega_{oc,opt} \approx \omega_a \,. \tag{4-53}$$

Therefore, the maximum generated amplitude of a piezoelectric harvester U_{max} can be calculated from substituting Equation (4-53) into Equation (4-48), thus

$$U_{max} = \frac{\alpha F_0}{2\zeta MC_p\omega_r\omega_a} \,. \tag{4-54}$$

Substituting Equation (4-53) into Equation (4-50) shows that the phase difference $\varphi_{u_{oc}}$ is about 90° when the maximum voltage is generated. To complete the process, the deflection under open-circuit condition $x_{oc}(t)$ must be calculated. This deflection can be expressed as

$$x_{oc}(t) = X_{oc}\sin\left(\omega t + \varphi_{x_{oc}}\right), \tag{4-55}$$

where X_{oc} is the amplitudes of the deflection under open-circuit condition and $\varphi_{x_{oc}}$ is the phase difference between the deflection $x_{oc}(t)$ and the force $F(t)$. In the same way that followed above, the amplitude X_{oc} and the phase $\varphi_{x_{OC}}$ can be calculated, thus

$$X_{oc} = \lim_{R_l \to \infty} X_R\ . \tag{4-56}$$

Substituting Equation (4-44) into Equation (4-56), and then solving the obtained equation to get that the amplitude X_{OC} can be expressed as

$$X_{oc} = \frac{(F_0/M)}{\sqrt{(\omega_a^2 - \omega^2)^2 + (2\zeta\omega_r\omega)^2}}\,. \tag{4-57}$$

The phase difference $\varphi_{x_{oc}}$ can be calculated from

$$\varphi_{x_{oc}} = \lim_{R_l \to \infty} \varphi_{x_R}\ . \tag{4-58}$$

Also, Substituting Equation (4-45) into Equation (4-58), then the phase difference $\varphi_{x_{OC}}$ found to be

$$\varphi_{x_{oc}} = \frac{\pi}{2} + \arctan\left(\frac{\omega_a^2 - \omega^2}{2\zeta\omega_r\omega}\right). \tag{4-59}$$

Again, substituting Equation (4-53) into Equation (4-59) shows that the phase difference $\varphi_{x_{oc}}$ is about 90° when the maximum deflection is achieved.

4.4.3 Base-Excited Harvester

Usually, a piezoelectric harvester is an electromechanical device that is located in or on a vibrating host structure in order to generate an AC voltage, which can be used to power an electronic application. In this construction, the base of the piezoelectric harvester is excited, thus exciting the entire structure. It is advisable to model such systems under one of the loading conditions defined previously: resistive-load condition or open-circuit. This enables us to perform a direct comparison between the two models and find the coupled variables.

Figure 4-14 shows a typical harvester under a resistive-load condition with $x_b(t)$ as the excited base displacement and $x_t(t)$ as the induced tip deflection. All other variables and parameters are the same as defined previously.

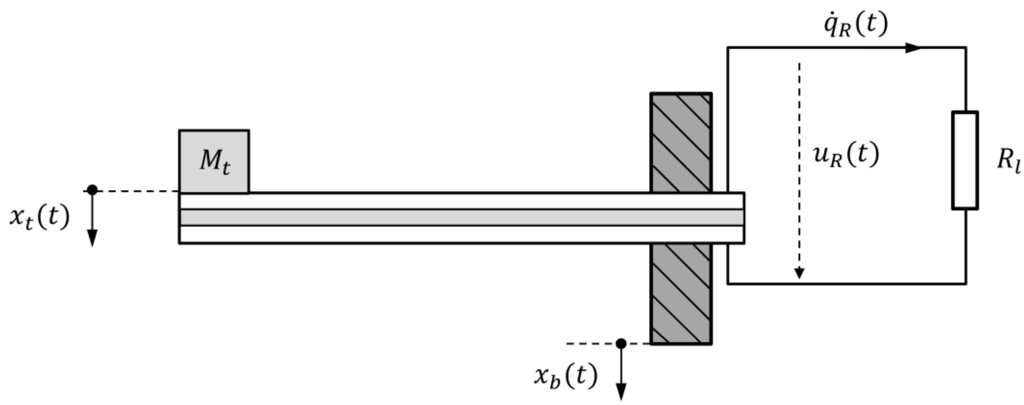

Figure 4-14 Base-excited piezoelectric harvester under resistive-load condition

The equivalent mechanical system is shown in Figure 4-15. This figure was constructed under the assumption, stated earlier, that the piezoelectric element used has low damping and a high mechanical quality factor, meaning that $x_b(t) \ll x_t(t)$.

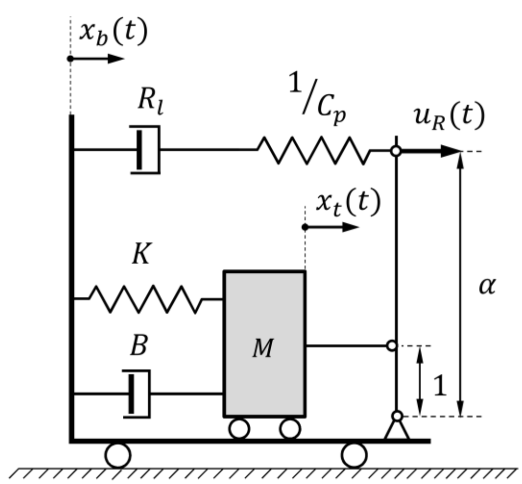

Figure 4-15 Equivalent systems of a base-excited harvester

If $x_R(t)$ is defined as the relative deflection such that

$$x_R(t) = x_t(t) - x_b(t), \tag{4-60}$$

then the governing equation can be expressed as

$$M\ddot{x}_t(t) + B\dot{x}_R(t) + Kx_R(t) = -\alpha u_R(t). \tag{4-61}$$

The equation for the electrical side is the same as the equation obtained earlier (Equation (4-29)). Regarding the governing equation, subtraction of $M\ddot{x}_b(t)$ from both sides gives

$$M\ddot{x}_R(t) - B\dot{x}_R(t) + Kx_R(t) = -M\ddot{x}_b(t) - \alpha u_R(t). \tag{4-62}$$

Comparing the governing equation of the base-excited system (Equation (4-62)) to that of the force-excited system (Equation (4-28)) shows that the force $F(t)$ can be replaced by the force $-M\ddot{x}_b(t)$, so that both equations have the same form. Therefore, this replacement can be used in all formulas obtained for force excitation, making them also valid for a base-excitation system. Thus, the generated AC voltage amplitude under a resistive-load condition U_R (Equation (4-38)) becomes

$$U_R = \frac{(\alpha R_l \omega)\, A_b}{\sqrt{\left[\omega_r^2 - \left(1 + 2\zeta\omega_r R_l C_p\right)\omega^2\right]^2 + \omega^2\left[2\zeta\omega_r + R_l C_p(\omega_a^2 - \omega^2)\right]^2}} \tag{4-63}$$

where A_b is the amplitude of the acceleration of the base excitation. The corresponding amplitude of the deflection X_R becomes (according to Equation (4-44))

$$X_R = A_b \sqrt{\frac{[1 + (R_l C_a \omega)^2]}{\left[\omega_r^2 - \left(1 + 2\zeta\omega_r R_l C_p\right)\omega^2\right]^2 + \omega^2\left[2\zeta\omega_r + R_l C_p(\omega_a^2 - \omega^2)\right]^2}}. \tag{4-64}$$

In the same way, the amplitude of the generated AC voltage under open-circuited condition U_{OC} given by Equation (4-48) here becomes for a base-excited system

$$U_{oc} = \frac{(\alpha/C_p)A_b}{\sqrt{(\omega_a^2 - \omega^2)^2 + (2\zeta\omega_r\omega)^2}} \tag{4-65}$$

and the corresponding amplitude of the deflection X_{oc} (according to Equation (4-57)) is

$$X_{oc} = \frac{A_b}{\sqrt{(\omega_a^2 - \omega^2)^2 + (2\zeta\omega_r\omega)^2}}. \tag{4-66}$$

Table 2-2 shows amplitudes of the accelerations for some representative excitation sources available in our environment.

4.4.4 Numerical Example

It is very important at this stage to simulate the models derived in order to investigate the performance of the harvester under the two alternating loading conditions due to the rectification process: resistive-load and open-circuit conditions.

A bimorph, such as that described in Table 3-2, is assumed to be a cantilever beam. The vibrating length of this bimorph is also assumed to be 39.5 mm. These data are used to calculate the electromechanical parameters and characteristic frequencies of this structure based on the model derived in Chapter 3 (see Section (3.2)). The resonance frequency and the anti-resonance frequency is calculated and found to be 234.4 Hz and 250.0 Hz, respectively. This imaginary harvester is assumed to be excited from its base with a harmonic acceleration. This acceleration has an amplitude equal to 5.5 $\mathrm{m/s^2}$.

The above calculated parameters are used to simulate Equation (4-63) across certain ranges of connected load R_l and excitation frequency f, as shown in Figure 4-16. This figure shows that the amplitude of the generated AC voltage U_R is strongly affected by both the connected load and the frequency of excitation. It is noted here that the amplitude U_R approaches the maximum generated amplitude U_{max} when the excitation frequency matches the anti-resonance and the connected load approaches infinite size.

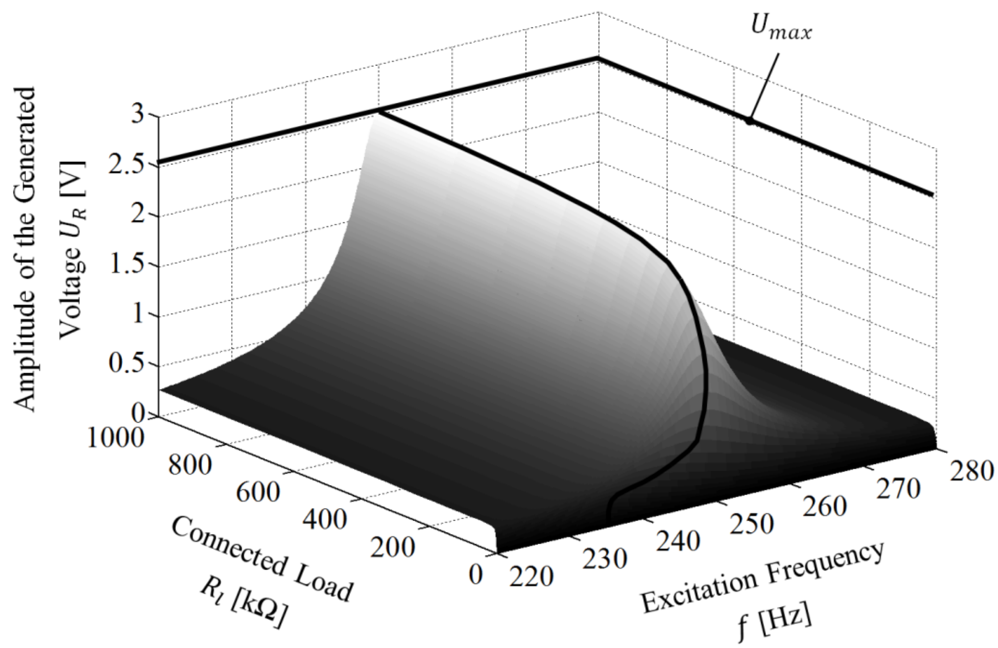

Figure 4-16 Generated voltage as a function of the excitation frequency and the connected load

Figure 4-17 shows the magnitudes and phases of the generated voltages across a range of connected loads, first when the harvester is excited at its resonance frequency and then when it is excited at its anti-resonance frequency. Figure 4-17 shows that both magnitude and phase of the generated voltage are considerably affected by the excitation frequency, but it was shown previously that the piezoelectric harvester with autonomous system experiences two alternating loading conditions due to the rectification process: open-circuit and resistive load conditions. Therefore, if the connected load is of low impedance, then the harvester generates voltages with different characteristics (magnitudes and phases) under these loading conditions. This can considerably impair the operation of the harvester and cause the system to behave nonlinearly. This conclusion can be supported by Figure 4-18, which shows the generated voltages, first when the harvester is in open-circuit condition, and then when the harvester is connected to a small load (8.1 $k\Omega$). In both situations, the harvester is tested within a certain range of excitation frequencies. This figure shows that the amplitudes and phases of the generated voltages in both cases vary considerably with the variation of the excitation frequency.

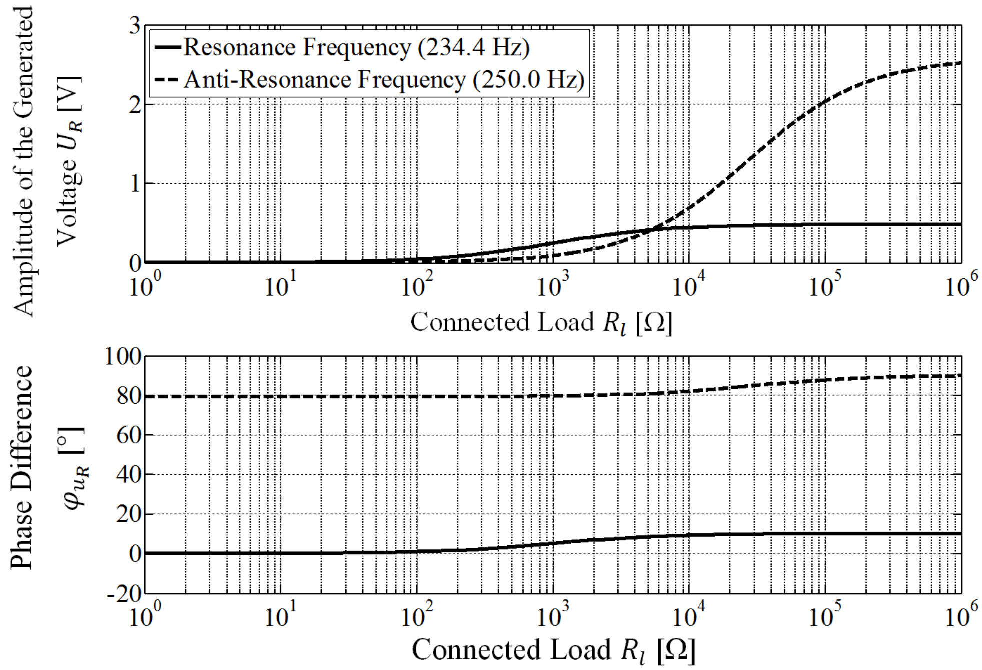

Figure 4-17 Magnitudes and phases of the generated voltages at resonance and anti-resonance frequency excitations

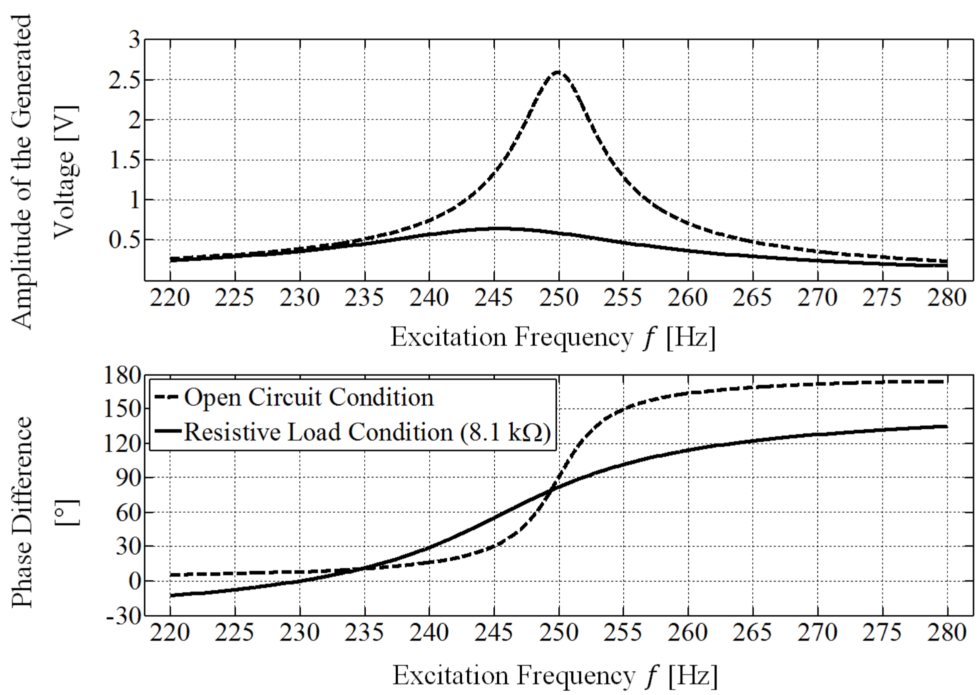

Figure 4-18 Magnitudes and phases of the generated voltages under small and large loads

This means that the harvester cannot generate a harmonic voltage if the connected load is of low impedance. Therefore, the autonomous system with low impedance load does not operate as described previously. Such system in steady state operation, specifically within the conduction time interval, current flows from the harvester into both the resistive load and the partly charged capacitor. When the capacitor voltage reaches a level close to the harvester voltage (minus the voltage drop across the diodes), the diodes block the current flow. The harvester is now in open-circuit condition. But in this condition, the harvester voltage amplitude is much higher than the capacitor voltage, causing the diodes to conduct again. This again changes the loading condition of the harvester and current flows into the load and the capacitor. This switching between conducting and non-conducting diode states occurs with an extremely high frequency and could not be measured in real application. The switching continues until the voltage generated by the harvester in open-circuit condition (minus voltage drop across diodes) becomes less than the capacitor voltage.

4.4.5 Frequency of Maximum Voltage

The optimal frequency $\omega_{R,opt}$ at which the maximum voltage is generated under resistive-load conditions can be calculated from the following condition

$$\left.\frac{dU_R}{d\omega}\right|_{\omega=\omega_{R,opt}} = 0\,. \tag{4-67}$$

Applying this condition to Equation (4-63) results in the only real positive solution being

$$\omega_{R,opt} = \sqrt{\frac{\beta_f + \left(3\sqrt{3}C_pR_l\omega_r^4 + \sqrt{27C_p^2R_l^2\omega_r^8 - \beta_f^3}\right)^{2/3}}{\sqrt{3}C_pR_l\left(3\sqrt{3}C_pR_l\omega_r^4 + \sqrt{27C_p^2R_l^2\omega_r^8 - \beta_f^3}\right)^{1/3}}}\,, \tag{4-68}$$

where

$$\beta_f = \left(2\zeta\omega_r + C_pR_l\omega_a^2\right)^2 - 2\omega_r^2\left(2\zeta C_pR_l\omega_r + 1\right). \tag{4-69}$$

Mathematically, Equation (4-69) is not valid for extremely small load values on the order of micro-ohms. However, these values are much lower than any real load, and cannot be generated by any real wire that could be used to short-circuit the system. For example, a wire of pure copper with a diameter of 0.5 mm and a length of 5 mm has a resistance of 0.43 mΩ, for which Equation (4-68) is still valid.

Figure 4-19 shows the typical plot of $\omega_{R,opt}$ over load resistance, calculated from Equation (4-69). The figure shows three distinct ranges of the optimal frequency:

I. Optimal frequency is almost constant and very close to the resonance frequency.
II. Maximum voltage is generated at a load-dependent frequency between resonance and anti-resonance frequencies.
III. Optimal frequency is almost constant and very close to the anti-resonance frequency.

In the following, these ranges are referred to the resonance frequency range (I), the load-dependent optimal frequency range (II) and the anti-resonance frequency range (III).

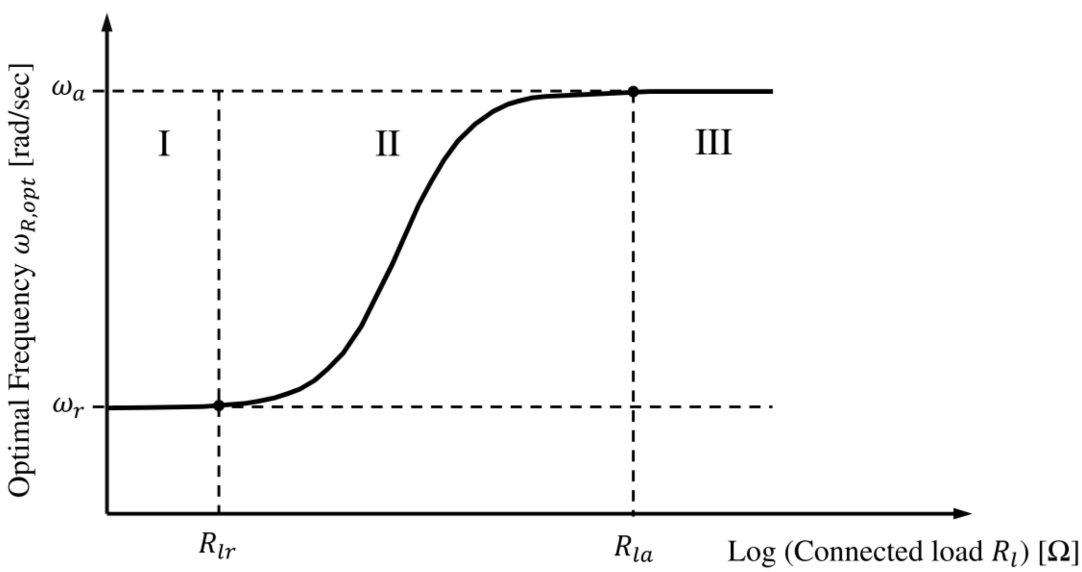

Figure 4-19 Optimal frequency of a piezoelectric harvester over connected load resistance

Referring to Figure 4-19, R_{lr} and R_{la} are resistances called the characteristic load resistances. The first one R_{lr} is the largest resistance at which the system can still be excited at its resonance frequency to generate the maximal voltage. This resistance can be calculated from Equation (4-68) as

$$\omega_r = \omega_{R,opt}(R_{lr})\ . \tag{4-70}$$

The second resistance R_{la} is the smallest one which is connected to the harvester when it operates at its anti-resonance frequency in order to generate the maximal voltage. This resistance can also be calculated from Equation (4-68), thus

$$\omega_a = \omega_{R,opt}(R_{la})\ . \tag{4-71}$$

Both these characteristic resistances can be determined from simulating a figure similar to that shown in Figure 4-19, which is based on Equation (4-68).

4.5 Experimental Verification

In this section, the validity of the derived models of the BAS is studied. Additionally, the nonlinearity of the BAS with low impedance load is investigated. For these purposes, typical piezoelectric harvesters are implemented and tested under different operation conditions such as varying the connected load or the frequency of the applied base acceleration.

4.5.1 Experimental Setup

Figure 4-20 schematically shows the setup that was used in the experiments discussed in this chapter. The piezoelectric harvester is excited with a harmonic acceleration supplied by an electro-dynamic shaker. In order to keep this acceleration at the desired value, it is monitored using a laser vibrometer with single laser head (2) and an oscilloscope. The amplitude and frequency of this acceleration are manually adjusted by manipulating the signal generator and amplifier used. A second vibrometer with two laser heads (1) and (3) is used to measure the relative deflection of the piezoelectric bimorph. The relative deflection refers to the difference between the tip and base displacements which is monitored and measured using an oscilloscope. The base frame of the harvester is rigid compared to the bimorph structure, so that the measured velocity at any location on the base frame is the same.

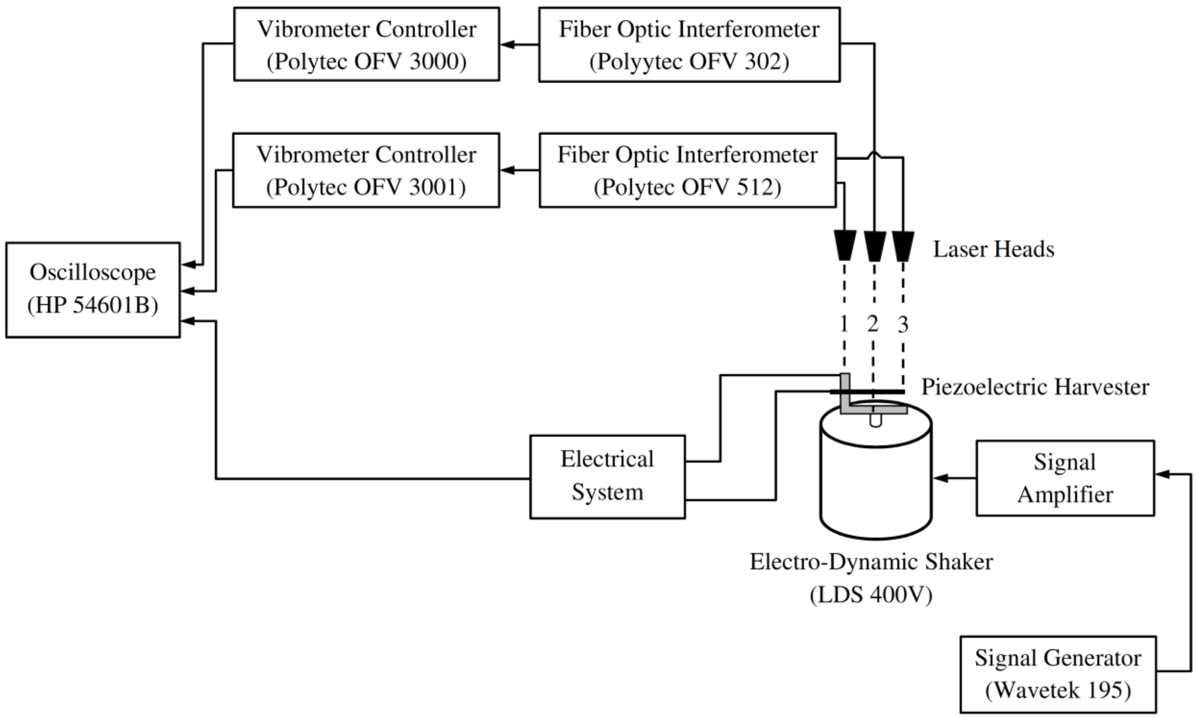

Figure 4-20 Schematic of the experimental setup

The “electrical system” in Figure 4-20 refers to the electrical components connected to the piezoelectric harvester. In the experiments performed here, this system can be one of two: it can be only a resistive load, or it consists of a full-wave rectifier, reservoir capacitor and resistive load. Both systems were studied for varying connected loads and excitation accelerations (amplitudes and frequencies). The generated AC voltage and its corresponding output DC voltage was measured and monitored using an oscilloscope.

4.5.2 Model Validation

In this section, the accuracy of the derived model for the piezoelectric harvester is considered. A piezoelectric harvester was used which has a setup similar to that shown in Figure 3-7. The length of the cantilevered beam was adjusted in order to tune the harvester anti-resonance frequency f_a to 250 Hz and the resonance frequency f_r to about 234.7 Hz.

Table 2-2 shows that amplitudes of excitation acceleration for energy harvesting applications commonly are ranged from 0.2 to $12.0\,\mathrm{m/s^2}$. Therefore, the derived model was investigated within this range for varying connected loads and excitation frequencies.

Figure 4-21 and Figure 4-22 show the amplitudes of the generated AC voltages: the former figure shows the harvester being excited at its resonance frequency f_r and the latter shows the harvester excited by an acceleration at the anti-resonance frequency f_a.

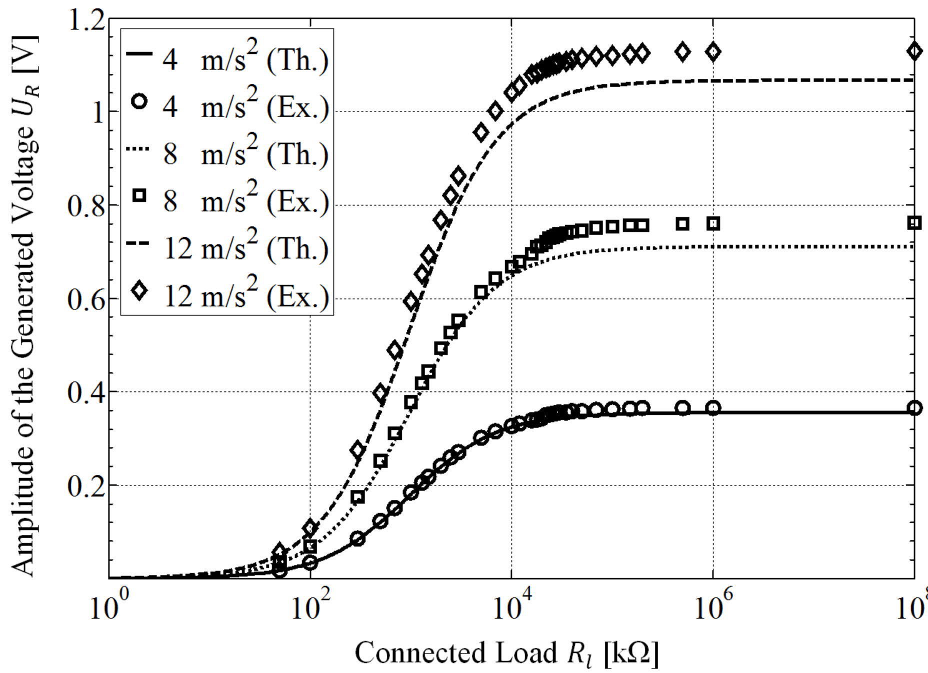

Figure 4-21 Piezoelectric harvester excited at an acceleration frequency matching its resonance frequency ($f_r = 234.7$ Hz)

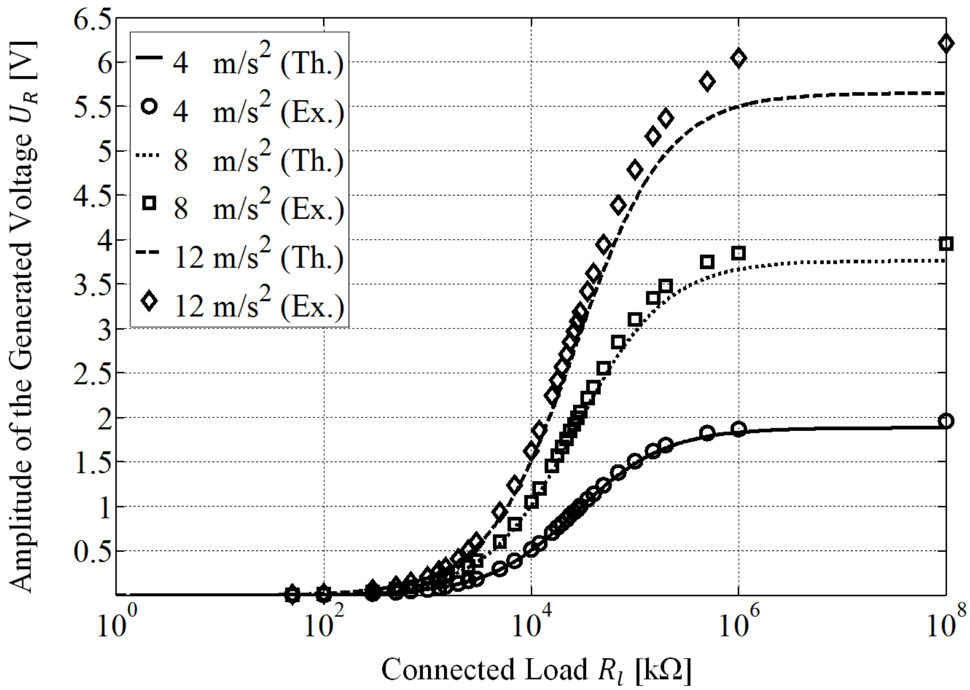

Figure 4-22 Harvester excited at an acceleration frequency matching its anti-resonance frequency ($f_a = 250.0$ Hz)

The difference between the simulated and the experimental results obtained for $4\ \mathrm{m/s^2}$ acceleration amplitude ranges from 1% to 3%, for $8\ \mathrm{m/s^2}$ acceleration amplitude from 5% to 8%, and for $12\ \mathrm{m/s^2}$ acceleration amplitude from 8% to 12%. It is concluded from these values that the deviations between the theoretical and experimental results increase with increasing amplitude of the excitation acceleration.

One possible reason for getting such deviations is using the lumped-parameter model which lacks the effect of the mode shape i.e. the description of the strain distribution along the beam. Also, assuming that the equivalent damping and the equivalent stiffness are linear (see Section (2.4.1)) can cause inaccurate results, especially if the excitation amplitude is large.

Also, the equivalent mass of the piezoelectric harvester can cause inaccurate results, especially if the excitation amplitude is large. This equivalent mass has been modeled with assuming that the curve of the deflection of the beam under dynamic loading condition is the same as that under static loading condition.

Figure 4-23 and Figure 4-24 show the amplitudes of the generated AC voltages for two cases across a range of excitation frequencies: first when the harvester is connected to a load equal to its resonance resistance ($R_{lr} = 1$ kΩ), and secondly when the connected load is equal to the harvester anti-resonance resistance ($R_{la} = 27.7$ kΩ). Both of these loads have been calculated by simulating Equation (4-68). These two figures confirmed that the harvester generates greater voltage if it is connected to a high impedance load and excited by a frequency matching the anti-resonance frequency of the piezoelectric harvester. both figures show accuracy similar to that obtained previously. The deviations between the theoretical and experimental results are also proportional to the amplitude of the excitation acceleration.

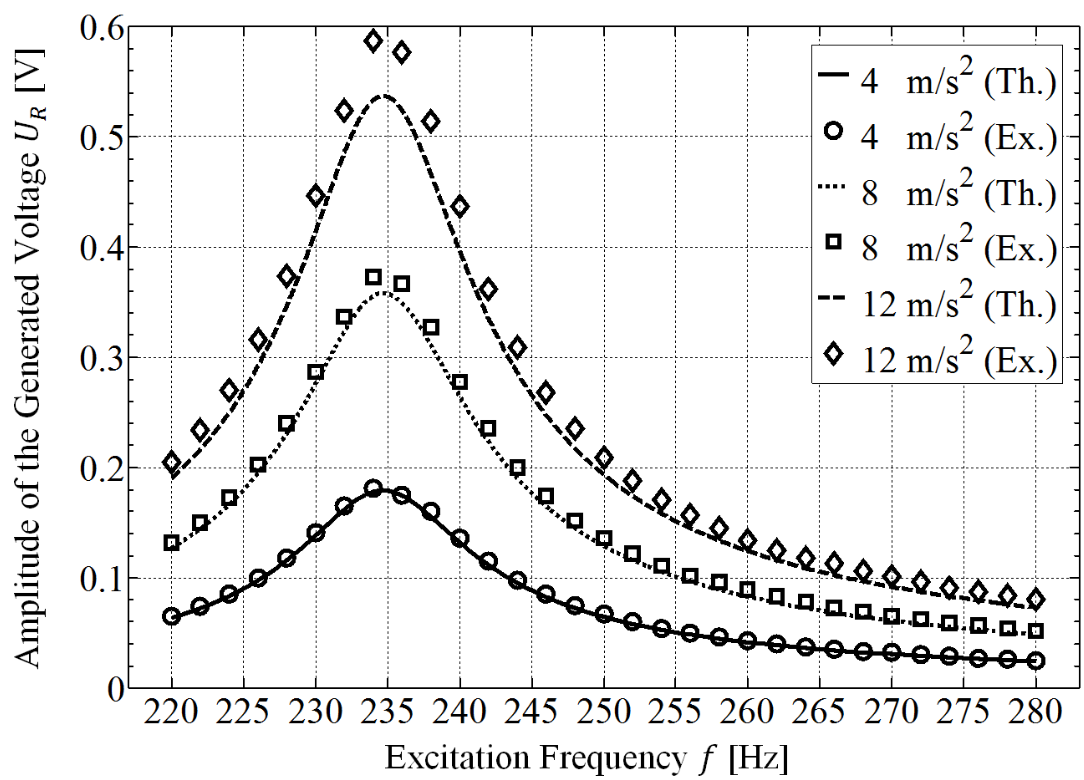

Figure 4-23 Frequency sweep of the generated voltage of a piezoelectric harvester connected to its resonance resistance $R_{lr} = 1$ kΩ

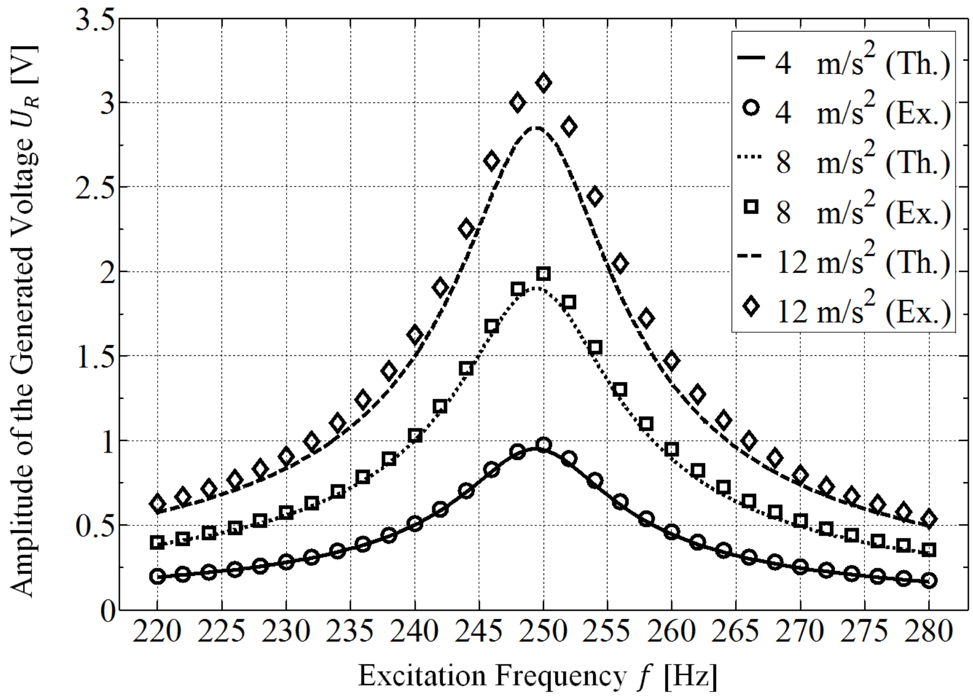

Figure 4-24 Frequency sweep of the generated voltage of a piezoelectric harvester connected to its anti-resonance resistance $R_{la} = 27.7$ kΩ

4.5.3 Characteristics of the Generated Voltage

Figure 4-25 shows the generated voltages of a typical harvester (described in Section (3.4)) operated under different resistive-load conditions, measured using an oscilloscope (Yokogawa DL1640 with input impedance of 1 MΩ). The harvester was excited by a base acceleration frequency equal to its anti-resonance frequency ($f_a = 238.1$ Hz). The excitation acceleration was applied with an amplitude of $A_b = 5.5$ $\mathrm{m/s^2}$. This figure shows that the voltage generated by the harvester under the larger loads is almost the same in amplitude and phase as that generated by the harvester when no load is connected, while the generated voltage under the smaller load is completely different in phase and amplitude.

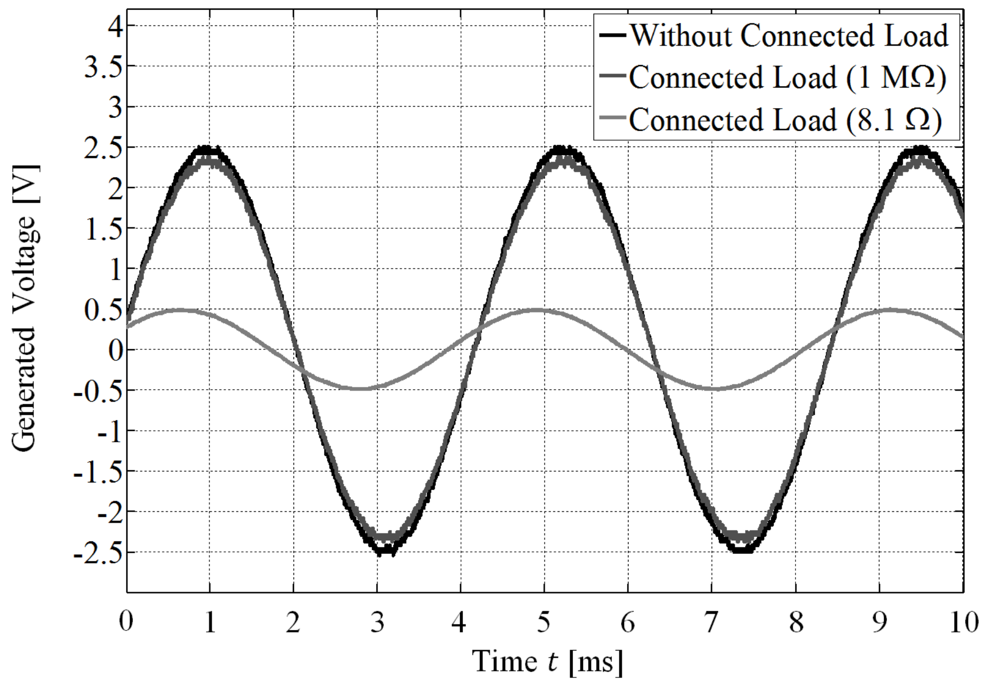

Figure 4-25 Generated voltage under different resistive load conditions, all excited by an acceleration frequency equal to the harvester anti-resonance frequency ($f_a = 238.1\ \text{Hz}$)

Figure 4-26 shows the measured voltages produced by the same piezoelectric harvester as above under different loading conditions, but this time connected to a full wave rectifier and proper capacitors for each load. The figure shows that the generated AC voltage is not a harmonic wave for the small load, but that it tends to move closer to a perfect harmonic wave for the larger connected load. Thus, the harvester generates almost the same voltage at the two alternating loading conditions, if it is connected to a large load.

Figure 4-26 confirms that the autonomous system with load of low impedance is a nonlinear system. In steady-state operation of such system, specifically within the conduction time interval, the harvester is loaded by the resistive load and the not-yet-fully charged capacitor. When the capacitor reaches a level close to the voltage of the harvester, it attempts to power the circuit, causing the diodes not to conduct. Therefore, the harvester is now in open-circuit condition. In this condition, however, the harvester generates a voltage amplitude higher than that of the capacitor (plus the voltage drop across the diodes), causing the diodes to conduct once again. This causes the loading condition of the harvester to change again; as the capacitor is now fully charged, though, this means that the diodes do not immediately begin to conduct. These conducting-and-not–conducting switches continue until the generated voltage in the open-circuit condition becomes less than that for the capacitor, at which point the harvester disconnects.

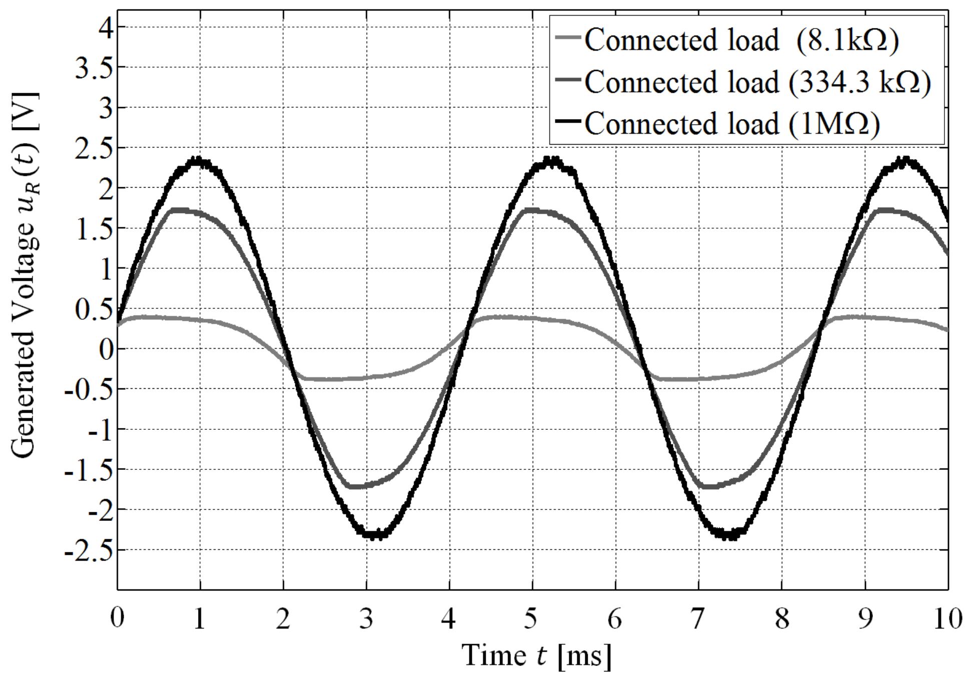

Figure 4-26 Generated voltage of a harvester in a BAS under different connected loads, all excited by an acceleration frequency equal to the harvester anti-resonance frequency ($f_a = 238.1$ Hz)

Now, it is concluded that the piezoelectric harvester in an autonomous application works efficiently and behaves linearly if it is connected to a relative high impedance load and is excited at a frequency matching to its anti-resonance frequency.

5 Harvester with Multiple Piezoelectric Elements

In this chapter, the model which describes the operation of the basic autonomous system (BAS) is extended in order to be valid for a BAS including a harvester with multiple piezoelectric elements.

The advantages of using multiple piezoelectric elements include increasing the generated voltage and/or expanding the operational frequency bandwidth of the piezoelectric harvester. Operational scenarios to achieve these objectives are proposed.

The proposed operational scenarios require fine frequency tuning for each piezoelectric element. Therefore, a frequency tuning technique called magnetic stiffening is introduced. The magnetic stiffening depends on changing the attraction force between two permanent magnets in order to affect the structural stiffness of the harvester. Furthermore, a finite element model has been constructed in order to investigate the effect of the magnetic forces on the behavior of the harvester. The experimental results prove the advantages of using multiple piezoelectric elements.

5.1 Configurations of the Piezoelectric Elements

Designing a piezoelectric harvester with multiple piezoelectric elements is a possible solution to some of the serious drawbacks which currently limit the usage of the piezoelectric harvester in applications. These drawbacks are related to the amount of the generated voltage and the bandwidth of the frequencies within which the piezoelectric harvester can operate efficiently, as introduced in Chapter 2. In such harvesters, the electrical connections between the piezoelectric elements, as well as the electromechanical characteristics of each one, are the important parameters which can be adjusted in order to increase the generated voltage or enhance the bandwidth. There are two primary possible types of connection to electrically connect the piezoelectric elements: they can be connected in series or in parallel. Generally, the elements are either connected in series in order to increase the output voltage or they are connected in parallel in order to increase the output current.

These connection types (series and parallel) are divided into direct and indirect. For example, Figure 5-1 shows the possible connection of two piezoelectric elements. In this figure, the piezoelectric elements are represented by AC voltage sources. The connection is direct if these sources are connected together before the rectification process; if they are connected together after the rectification process, it is then an indirect connection.

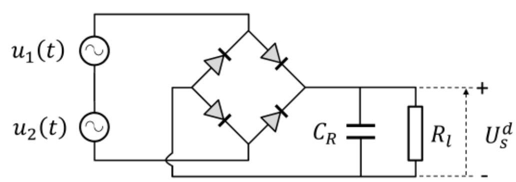

(a) Direct Series Connection

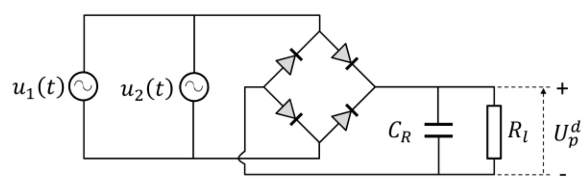

(c) Direct Parallel Connection

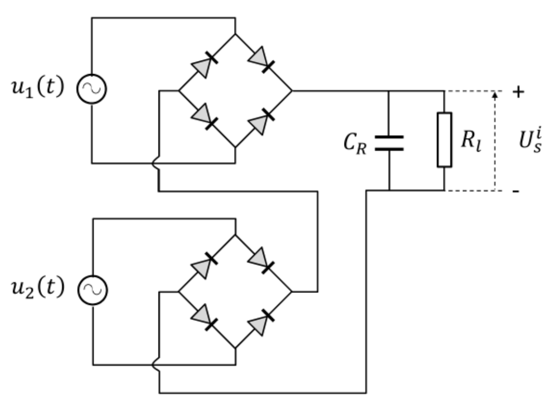

(b) Indirect Series Connection

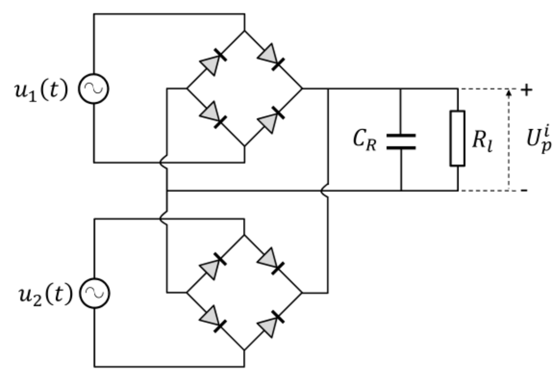

(d) Indirect Parallel Connection

Figure 5-1 Possible types of electrical connection of two piezoelectric elements (represented as voltage sources)

5.1.1 Direct Series Connection

In a direct series connection, the electrodes of all the piezoelectric elements of a harvester are connected together in series before the rectification process. Figure 5-1a shows an example for connecting two piezoelectric elements in direct series.

If $u_i(t)$ is the generated voltage of the i^{th} element of a harvester with number n of piezoelectric elements, then the total generated voltage $u_t(t)$ can be expressed as

$$u_t(t) = \sum_{i=1}^{i=n} u_i(t) \,. \tag{5-1}$$

If the connected load is of a high impedance, then each bimorph generates a harmonic AC voltage as introduced in the previous chapter. The generated AC voltage of the i^{th} piezoelectric element can be described by

$$u_i(t) = U_i \sin(\omega t + \varphi_i) \,, \tag{5-2}$$

where U_i and φ_i are the amplitude and the phase difference of the generated voltage of the i^{th} piezoelectric element, respectively. Therefore, the total generated voltage $u_t(t)$ can be assumed to be harmonic also and can be expressed as

$$u_t(t) = U_t \sin(\omega t + \varphi_t) \,, \tag{5-3}$$

where U_t and φ_t are the amplitude and the phase difference of the total generated voltage $u_t(t)$, respectively. Thus, the corresponding total output DC voltage U_s^d can be calculated as

$$U_s^d = \begin{cases} U_t - 2U_d & \text{if } U_t > 2U_d \\ 0 & \text{if } U_t \leq 2U_d \end{cases} \,. \tag{5-4}$$

If all the piezoelectric elements are from the same type and all are tuned to have the same optimal frequency (the frequency at which the harvester generates the maximum voltage), then the maximum output DC voltage at direct series connection is generated. Thus, all of the elements generate the same voltage $u_s(t)$ which can be expressed as

$$u_s(t) = U_s \sin(\omega t + \varphi_s) \,, \tag{5-5}$$

where U_s and φ_s are the common amplitude and the phase difference of the generated voltage by each piezoelectric element, respectively. Substituting Equation (5-5) into

Equation (5-1) gives that the maximum generated AC voltage $u_{max}(t)$ can be expressed as

$$u_{max}(t) = n \cdot U_s \sin(\omega t + \varphi_s). \tag{5-6}$$

Therefore, the corresponding generated DC voltage U_{max}^d can be calculated as

$$U_{max}^d = \begin{cases} (n \cdot U_s) - 2U_d & \text{if } n \cdot U > 2U_d \\ 0 & \text{if } n \cdot U \leq 2U_d \end{cases}, \tag{5-7}$$

where U_s can be calculated using Equation (4-63).

If all the piezoelectric elements are from the same type and are all tuned to have different optimal frequencies, then the total output voltage $u_t(t)$ may not increase. This is because each element generates an AC voltage with characteristics (magnitude and phase) which differ from the characteristics of the voltages generated by the other elements, as can be predicated from Figure 4-18 in Chapter 4.

5.1.2 Indirect Series Connection

The indirect series connection means that the piezoelectric elements are connected in series after the rectification process has been carried out, as indicated in the example circuit shown in Figure 5-1b.

For a harvester with n piezoelectric elements, the output DC voltage of the i^{th} element U_i^{dc} can be expressed as

$$U_i^{dc} = \begin{cases} U_i - 2U_d & \text{if } U_i > 2U_d \\ 0 & \text{if } U_i \leq 2U_d \end{cases}, \tag{5-8}$$

where U_i is the amplitude of the generated voltage of the i^{th} element of a harvester (see Equation (5-2)). Thus, the total output DC voltage U_s^i then can be expressed as

$$U_s^i = \sum_{i=1}^{i=n} U_i^{dc}. \tag{5-9}$$

Again, if all the piezoelectric elements are from the same type and are all tuned to have the same optimal frequency, then each element generates the same AC voltage

$u_s(t)$ (Equation (5-5)). Therefore, the maximum generated DC voltage at indirect series connection U_{max}^{i} can be obtained from substituting Equation (5-5) into Equation (5-8), then substituting the result into Equation (5-9), thus

$$U_{max}^{i} = \begin{cases} n \cdot (U_s - 2U_d) & \text{if } U_s > 2U_d \\ 0 & \text{if } U_s \leq 2U_d \end{cases}. \qquad (5\text{-}10)$$

Comparing Equation (5-7) to (5-10) shows that the voltage loss in the indirect connection is greater than that in the direct connection. Therefore, it is not advisable to use an indirect series connection when the piezoelectric elements have the same optimal frequency.

Nevertheless, this type of connection can be used to expand the bandwidth of a piezoelectric harvester. To achieve this goal, each element should be tuned to a certain optimal frequency depending on a predefined scenario which is called the tuning scenario. This tuning scenario can have any arrangement related to requirement of the used application and the preferences of the designer.

The tuning scenario proposed in this work can be illustrated by the example shown in Figure 5-2. This figure shows the generated voltage of three neighbor piezoelectric elements (solid-line curves). The piezoelectric elements are assumed to generate equal peaks of DC voltage. These elements are tuned in such a way that at the frequencies f_{h1} and f_{h2}, each of the neighboring elements generates half of the peak DC voltage. Thus, the total generated voltage is theoretically similar to that shown in Figure 5-2 (dashed-line curve). Using this scenario, the peak voltage generated by a single piezoelectric element at a single excitation frequency is extended across a considerable range of excitation frequencies.

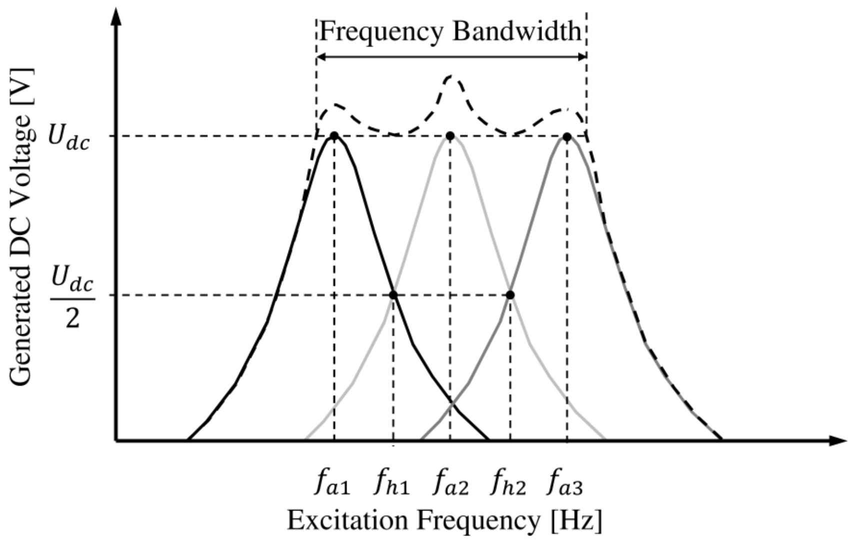

Figure 5-2 Schematic of tuning scenario for bandwidth enhancement

5.1.3 Parallel Connections

If a harvester includes piezoelectric elements with different optimal frequencies which are connected in parallel, then only the element that generates the higher voltage powers the load, while the other elements do not. In a direct parallel connection, the other elements which are not generating voltage at the moment behave as additional parallel loads. Therefore, these elements cause the generated voltage to decrease. This is because these parallel elements reduce the overall load connected to the operating element.

In indirect parallel connections, the voltage generated by the operating element prevents the rectifier circuits of the other elements from conducting. Therefore, it is not advisable to use either parallel connection type if the piezoelectric elements have different optimal frequencies.

If all the piezoelectric elements have the same optimal frequency and are connected in parallel (direct or indirect), then the generated current increases. This case is not examined further because it is interested in replacing batteries with piezoelectric harvesters in currently commercial electronic applications. In such applications, achieving the required voltage is necessary to ensure achieving of the required power for the operation; the current is therefore uninteresting for this purpose.

5.2 Frequency Tuning Method

A harvester with multiple piezoelectric elements must be designed while considering a method to perform a fine frequency tuning for each of its elements. The tuning method used to adjust the frequencies of the piezoelectric elements is based on the excitation frequency and the tuning scenario.

One possible method that can be used to perform a frequency tuning is accomplished by using a pair of permanent magnets. This tuning method is called magnetic stiffening. This method depends on adjusting the distance between two permanent magnets positioned facing each other, thereby changing the attraction force between these magnets by adjusting the separation distance between them. This attraction force affects the stiffness of the piezoelectric element and thus its characteristic frequencies.

Magnetic stiffening is based on a typical piezoelectric harvester with an additional magnet at its free end, see Figure 5-3. A second magnet, aligned opposite the first one in axial direction. The magnetic force depends on the distance y_M between the magnets. As y_M can be adjusted without touching the vibrating piezoelectric element, the optimal frequency of the harvester can be adjusted during operation.

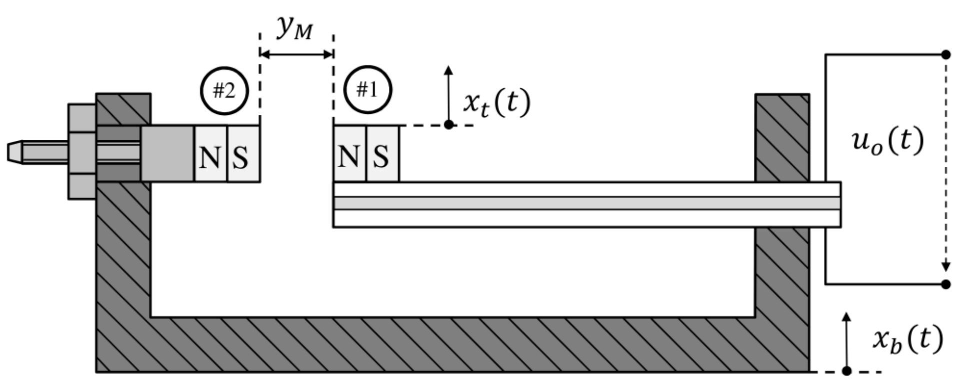

Figure 5-3 Schematic of a tunable energy harvester using axially aligned magnets

All the variables shown in Figure 5-3 are as defined earlier, where $x_b(t)$ is the base excitation displacement, $x_t(t)$ is the corresponding tip deflection and $u_o(t)$ is the generated AC voltage under open-circuit conditions.

5.3 Determination of Magnetic Force

It is desirable to model the attraction force between the two magnets. This model must be based on the properties of the magnets and separation distance between them. Such modeling leads to a complex and multi-dimensional calculation task. Finite element analysis can be used to calculate the magnetic force, but such analysis requires advanced knowledge of magnetism and detailed information about the characteristics of the magnet(s) used. As an alternative solution, an online interpolator based on a large dataset of experimental measurements conducted by K&J Magnetics [2013] has been used. Basing on these data, an empirical model for determining the attraction force between two identical rectangular permanent magnets has been developed. The attraction force F_M is expressed as

$$F_M = l_M \cdot w_M \cdot h_M^c \cdot B_r \cdot \left|B_y(y_M)\right| \cdot f(y_M)\,, \tag{5-11}$$

where l_M, w_M and h_M are the length, width and thickness (in magnetization direction) of the magnet and B_r is the residual flux density of the magnet; these values can be taken from the magnet datasheet. c is an empirical corrective exponent and $f(y_M)$ is an empirical function describing the decay of the attraction force between two magnets. $\left|B_y(y_M)\right|$ is the magnitude of the magnetic flux density field of a single magnet at a distance d from one of its poles. For a rectangular magnet, $\left|B_y(y_M)\right|$ is computed using the following formula [Magnet Sales & Manufacturing Inc., 2000]:

$$\begin{aligned}\left|B_y(y_M)\right| = \frac{B_r}{\pi}\Bigg[&\arctan\left(\frac{l_M\, w_M}{2y_M\sqrt{4y_M^2 + l_M^2 + w_M^2}}\right)\\ &- \arctan\left(\frac{l_M w_M}{2(h_M + y_M)\sqrt{4(h_M + y_M)^2 + l_M^2 + w_M^2}}\right)\Bigg]\,.\end{aligned} \tag{5-12}$$

To determine the empirical parameters, a reference magnet with the dimensions $l_M \times d_M \times h_M = 6\ \text{mm} \times 6\ \text{mm} \times 4\ \text{mm}$ and material class N42, with a residual flux density of $B_r = 1.32\ \text{T}$, is used in the curve fitting process. Starting from this reference, l_M, w_M, h_M and B_r are varied individually, and a suitable formula for $f(y_M)$ as well as a value for c are identified by curve fitting. The function $f(y_M)$ is found to be

$$f(y_M) = \left(1.749 + 1.145\, e^{\left(-\frac{y_M}{y_0}\right)}\right) \times 10^6 \mathrm{NT^{-2}m^{-7/3}}\,, \tag{5-13a}$$

where $y_0 = 1$ mm. The curve fitting gives that the constant c has the following value:

$$c = 0.33\,. \tag{5-13b}$$

The above stated model gives good accurate results for any type magnet which is fabricated from the neodymium material, as will be shown later in Section (5.5.1).

5.4 Modeling of Tuning Method

In this section, a model is derived which describes the effect of the magnetic stiffening on the characteristic frequencies of the piezoelectric harvester.

5.4.1 Equivalent System

At any separation distance y_M within the range in which the magnets still attract each other, the harvester is loaded by the magnetic force and the mass of the attached magnet M_M. The magnetic force can be split into two components: $F_{Mx}(t)$ in x-direction and $F_{My}(t)$ in y-direction as shown in Figure 5-4.

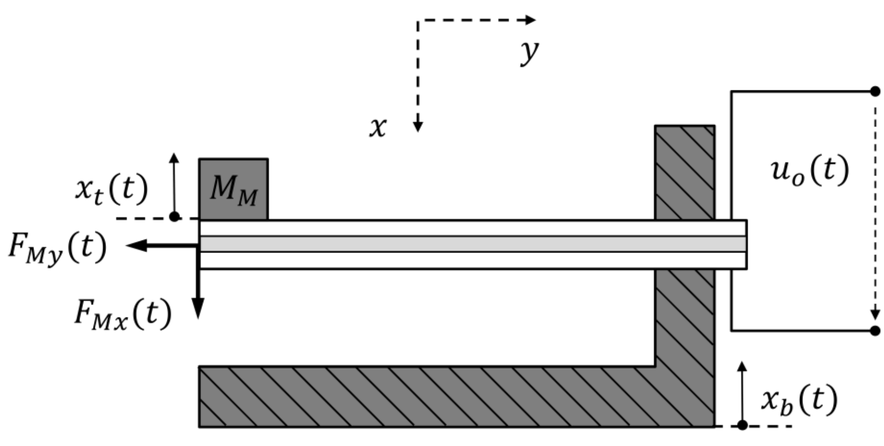

Figure 5-4 Effect of magnetic forces on a vibrating harvester

The magnetic force component $F_{My}(t)$ has a fixed direction; it acts as an external tension force. This force has a slightly varied magnitude due to the variation of separation distance during the vibration. Therefore, it is assumed to have constant magnitude.

The other magnetic force component $F_{Mx}(t)$ always acts opposite to the direction of the vibration. This force varies from zero at no deflection position (equilibrium position) to the maximum at the greatest deflection position (maximum deflection). The behavior of all the forces acting on the piezoelectric element during vibration is shown in Figure 5-5.

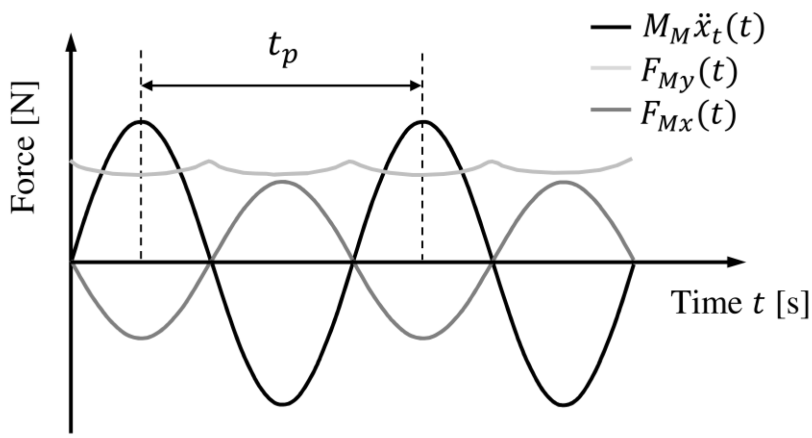

Figure 5-5 Forces acting on the piezoelectric element during vibration

Timoshenko [1937] modeled the effect of this force (axial force $F_{Mx}(t)$) on the structural stiffness of a cantilever beam. Based on that model, this force can be modeled as an additional spring K_{M1} attached to the free end of the harvester.

The transverse force component $F_{Mx}(t)$ is the primary parameter that determines the harvester characteristic frequencies. This force behaves as the force from a mechanical spring, as shown in Figure 5-5. This force considerably affects the structural stiffness of the harvester. The stiffness equivalent to the effect of this transverse force is K_{M2}.

The total stiffness, equivalent to the effect of the magnetic forces, can be expressed as

$$K_M = K_{M1} + K_{M2}\,. \tag{5-14}$$

The equivalent system of a piezoelectric harvester with magnetic tuning effects is shown in Figure 5-6.

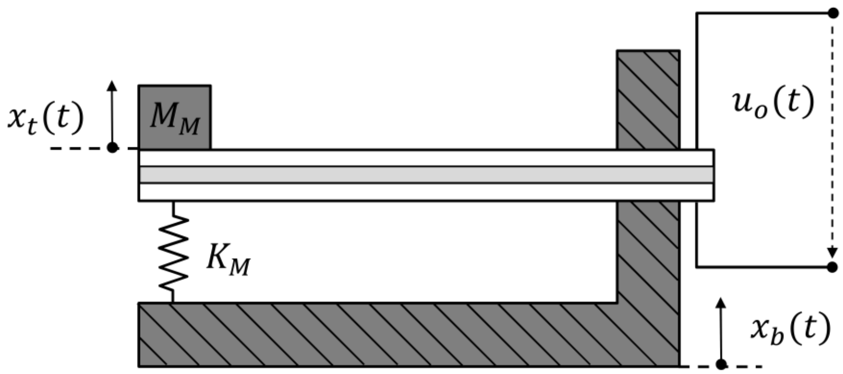

Figure 5-6 Equivalent effect of magnetic force on the harvester structure

5.4.2 Modeling of the Magnetic Stiffening

Figure 5-7 shows a frozen instant of the harvester shown in Figure 5-3 while it is vibrating. All the variables in this figure are as previously defined. θ is the angle between the magnetic force F_M and the x-axis. X_0 is the amplitude of the deflection of the harvester.

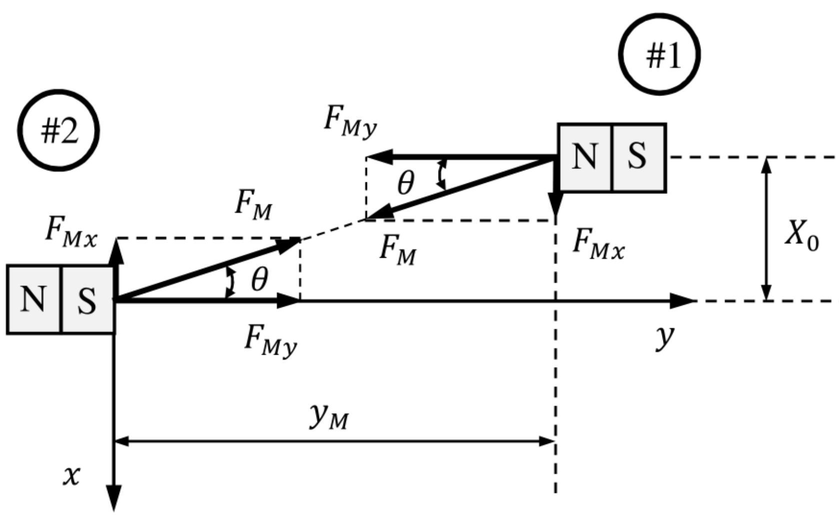

Figure 5-7 Components of the magnetic force

The resonance frequency of a cantilever with the application of a constant axial load $\omega_{r,ax}$ can be expressed as [Timoshenko, 1937]

$$\omega_{r,ax} = \omega_r \sqrt{1 + \left(\frac{5}{14}\right)\frac{F_{My} l^2}{E_b I_b}}\,, \tag{5-15}$$

where ω_r is the unloaded resonance frequency, l is the span of the cantilever, E_b is the modulus of elasticity and I_b is the moment of inertia. The unloaded resonance frequency ω_r can be calculated using Equation (4-36a).

Let K_F be the equivalent spring stiffness in transverse direction representing the effect of the axial force on the cantilever resonance frequency; as a result

$$\omega_{r,ax} = \sqrt{\frac{K + K_F}{M}}\,, \tag{5-16}$$

where M is the total equivalent vibrating mass of the structure, as defined in Chapter 3. Using the resonance frequency equation (Equation (4-36a)) with Equations (5-15) and (5-16) gives that the stiffness K_F can be expressed as

$$K_F = \left(\frac{5}{14}\right)\left(\frac{F_{My} l^2}{E_b I_b}\right) K\,. \tag{5-17}$$

Substituting Equation (3-18) which describes the equivalent stiffness of a cantilever beam into Equation (5-17), thus

$$K_F = \left(\frac{15}{14}\right)\frac{F_{My}}{l}\,. \tag{5-18}$$

If the vibration amplitude X_0 is small compared to the separation distance y_M of the magnets, θ is then also small, so that $F_{My} \approx F_M$. Thus the equivalent spring stiffness for the magnetic effect becomes

$$K_{M1} = \left(\frac{15}{14}\right)\frac{F_M}{l}\,. \tag{5-19}$$

Referring to Figure 5-7, the transverse magnetic force can be expressed as

$$F_{Mx} = F_M \sin\theta \tag{5-20}$$

and for small angles

$$\sin\theta \approx \tan\theta = \frac{X_0}{y_M}. \tag{5-21}$$

Substituting Equation (5-21) into Equation (5-20), the transverse force becomes

$$F_{Mx} = \left(\frac{F_M}{y_M}\right) X_0 . \tag{5-22}$$

This shows that the stiffness for this force can be described as

$$K_{M2} = \frac{F_M}{y_M}. \tag{5-23}$$

The total equivalent stiffness for the magnetic effect in the x- direction is therefore

$$K_M = K_{M1} + K_{M2} = \left(\frac{1}{y_M} + \frac{15}{14l}\right) F_M . \tag{5-24}$$

As stated in the previous chapters, the piezoelectric element used in the harvester has a low damping ratio, i.e. $\zeta \ll 1$. Therefore, the characteristic frequencies can be represented by only the resonance and anti-resonance frequencies. Based on Equation (3-36), the resonance frequency under magnetic stiffening can be expressed as

$$\omega_r = \sqrt{\frac{K_{bsc} + K_M}{M}}. \tag{5-25}$$

The anti-resonance frequency under magnetic stiffening is calculated from Equation (3-37) and found to be

$$\omega_a = \sqrt{\frac{K_{boc} + K_M}{M}} . \tag{5-26}$$

where K_{bsc} and K_{boc} are the short-circuit and the open-circuit stiffnesses, respectively. M is the equivalent mass and can be calculated using Equation (3-20), but here the attached tip mass M_t must be replaced by the magnet mass M_M.

5.4.3 Finite Element Model

It is important to study the effect of the magnetic tuning technique on the mode shape of the piezoelectric element. Changing the mode shape not only affects the generated voltage, but also invalidates the assumptions which were used when deriving the model which describes the magnetic stiffening.

Using finite element tools (FE-tools) is one possible way to simulate the harvester under the effect of magnetic force. Such simulation requires an advanced knowledge of magnetism, as well as detailed information about the magnet used. This simulation contains a particular difficulty in that the magnetic force should be coupled to the mechanical system and is at the same time a function of the beam deflection, i.e. the magnetic force acts on the deflection magnitude while, simultaneously, the deflection magnitude acts on the magnetic force (magnitude and direction). This complex loop makes such simulation program difficult to implement correctly.

An alternative solution is to investigate the effect of the magnetic stiffening by implementing the equivalent model, as shown in Figure 5-8. This is accomplished using ANSYS/Workbench. The beam dimensions and properties are same as those given in Table 3-2. The magnet used has a face area of 8.5 x 2 mm^2 and a thickness of 1.5 mm (from HKCM Engineering, manufacturing code Q08.5x02x01.5Ni48H). The size of the magnet is suitable for it to be attached to the front of the piezoelectric bimorph, as shown in Figure 5-8.

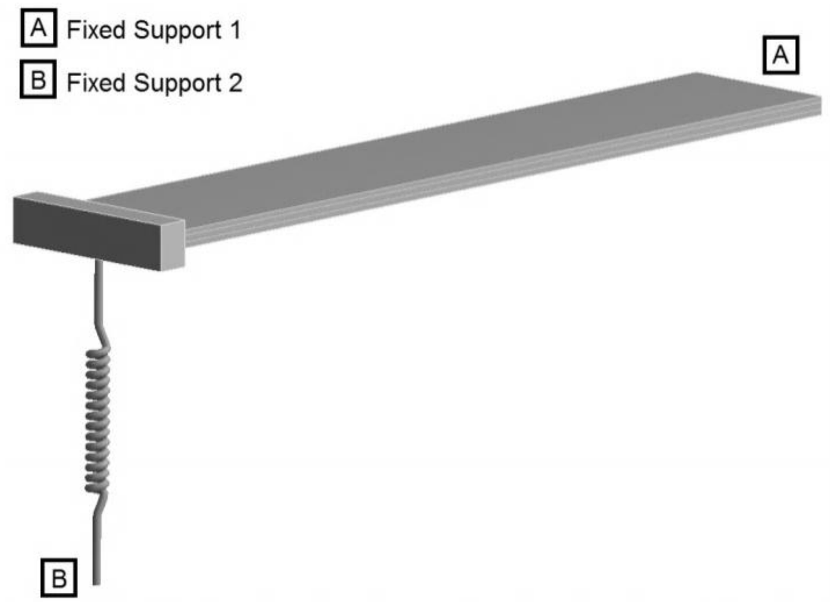

Figure 5-8 Simulation of the equivalent system in ANSYS

Figure 5-9 shows the calculated equivalent magnetic stiffness K_M (Equation (5-24)) as a function of the magnet separation distance, as well as the mode shapes at the first eigenfrequency, calculated for arbitrarily chosen distances of 0.1, 1, and 10 mm.

Figure 5-9 shows that for separation distances 1 mm and 10 mm, the mode shape changes only very slightly, unlike the case at the distance equal to 0.1 mm where the mode shape change is more significant. This change in mode shape is due to the large magnetic stiffness K_M which causes the beam to deform as if pinned at the tip. Therefore, it is concluded that for every magnetically stiffened harvester there is minimal separation distance y_{min} below which the vibration mode shape of the harvester is changed significantly. The value of this minimal separation distance y_{min} depends on the sizes and properties of the magnets. For the currently used setup, the minimal separation is identified to be equal to $y_{min} = 1$ mm.

Changing the mode shape causes a change in strain distribution along the length of the cantilever beam. Thus, the generated charges along the length of the attached electrodes can cancel each other partly. Therefore, it is not recommended to use magnetic stiffening for separation distances smaller than y_{min} in energy harvesting applications.

Due to the change in mode shape, the effective stiffness and the equivalent mass of the beam are also changed. Thus, the model introduced earlier cannot be appropriate for the distances smaller than y_{min}. Therefore, the magnetic stiffness K_M shown in Figure 5-9 is distinguished by a dashed line for the distances smaller than 1 mm.

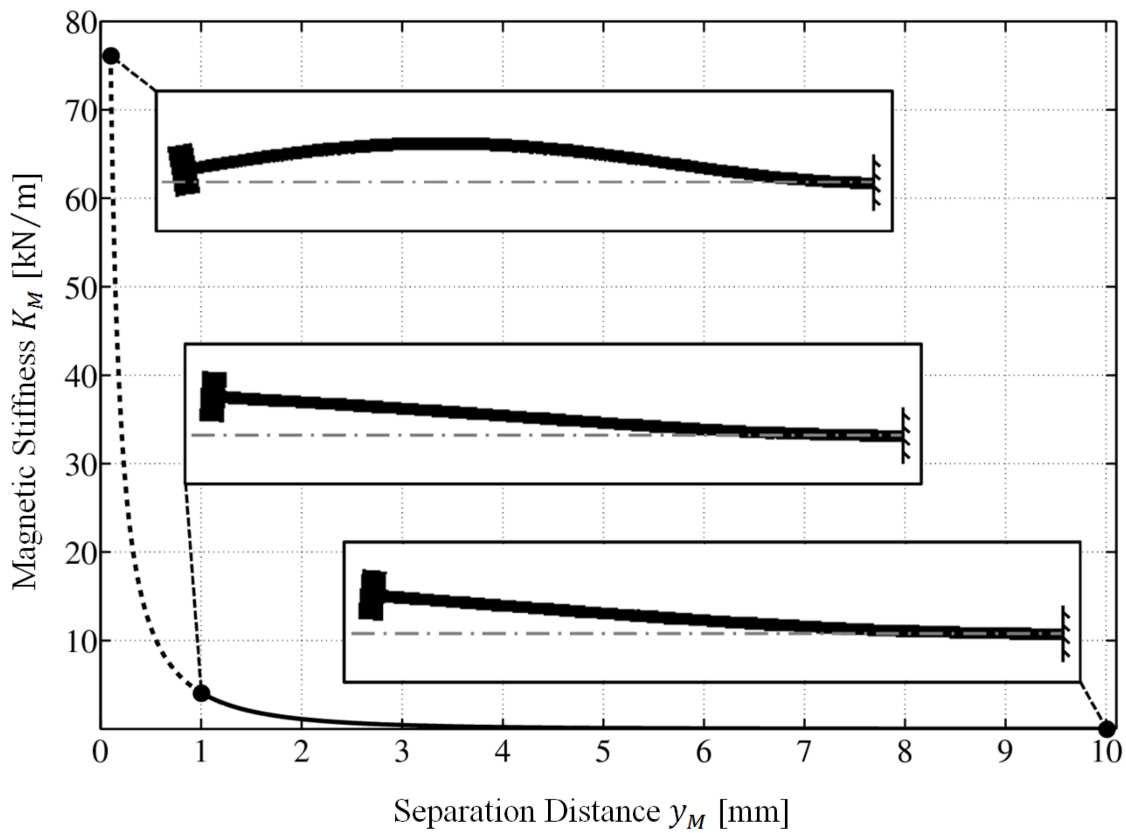

Figure 5-9 Calculated equivalent magnetic stiffness as a function of magnet separation distance; insets show mode shapes, calculated for distances 0.1, 1, and 10 mm using finite element simulation

5.5 Experimental Results and Discussion

Here, the models derived previously in this section are validated by comparing the numerical results with the corresponding experimental results.

5.5.1 Magnetic Force Calculation

In this section, the empirical model introduced in Section (5.3) is validated. This model describes the attraction force between two permanent magnets. The results of this model are investigated for two types of permanent magnets from HKCM Engineering: a large magnet (manufacturing code Q10×04.5×04.5Ni-N52) and a small magnet (manufacturing code Q08×02×01.5Ni48H).

Figure 5-10 shows the comparison between the results of the empirical model and the experimental data for both these magnets. The experimental data are obtained from K&J Magnetics [2013]. The figure shows that the empirical model provides predominantly accurate results. For the larger and stronger magnet and for very small distances below 0.5 mm, the deviation increases significantly, although the model remains accurate for the smaller and weaker magnet at these distances. Consequently, the model should be applied cautiously at small distances below approximately 0.5 mm.

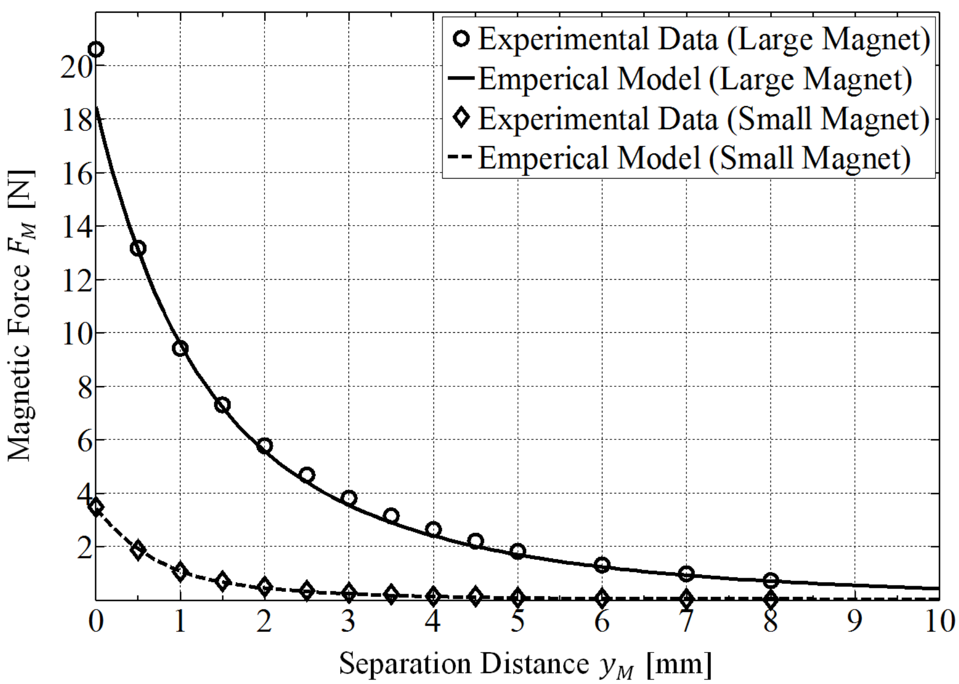

Figure 5-10 Comparison between empirical model and experimental data from K & J Magnetics for magnetic attraction force

5.5.2 Tuning Method Validation

The resonance frequency can be identified by measuring the electrical admittance of the bimorph, as discussed in Chapter 3. The electrical admittance is measured for different separation distances between the magnets. For this purpose, an impedance analyzer of the type HP 4192A has been used. The bimorph excitation voltage is 500 mV_{RMS}.

The experimental setup is shown in Figure 5-11. In this setup, the piezoelectric bimorph used has the specifications given in Table 3-2. The magnets are from HKCM Engineering, manufacturing code Q08.5×02×01.5Ni48H, with a face area of 8.5 × 2 mm^2 and a thickness of 1.5 mm. The distance between the two magnets is adjusted using a micrometer screw.

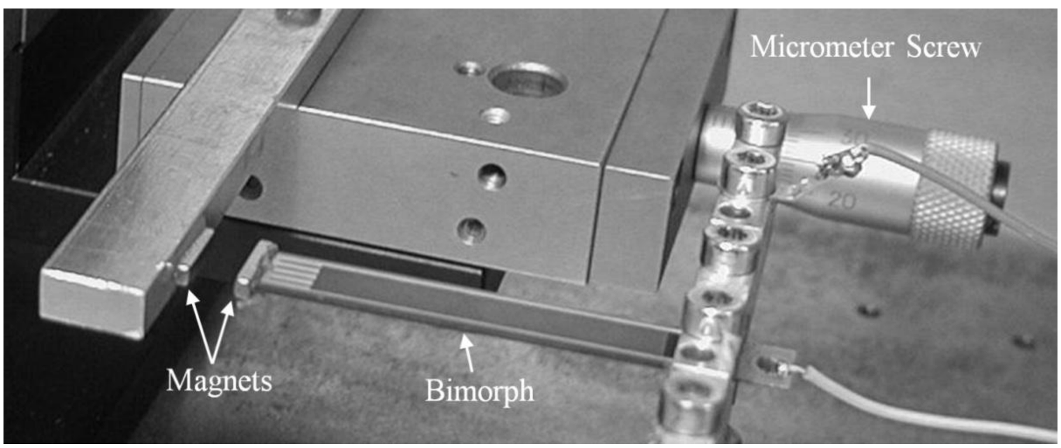

Figure 5-11 Experimental setup of the magnetic stiffening technique

The frequency sweeps of the electrical admittance of the bimorph were measured for separation distances ranging from 0.5 mm to 10 mm. Figure 5-12 shows some of these frequency sweeps at different selected separation distances. It is concluded from this figure that resonance and the anti-resonance frequencies cannot be identified for the distances smaller than 1 mm. for example, at separation distance equal to 0.5 mm, the frequency sweep of the phase of the electrical admittance never becomes zero. The main reason for this is the change in mode shape as discussed earlier in Section (5.4.3). Therefore, the distance 1 mm is identified to be the minimal separation for this setup, i.e. y_{min} =1 mm.

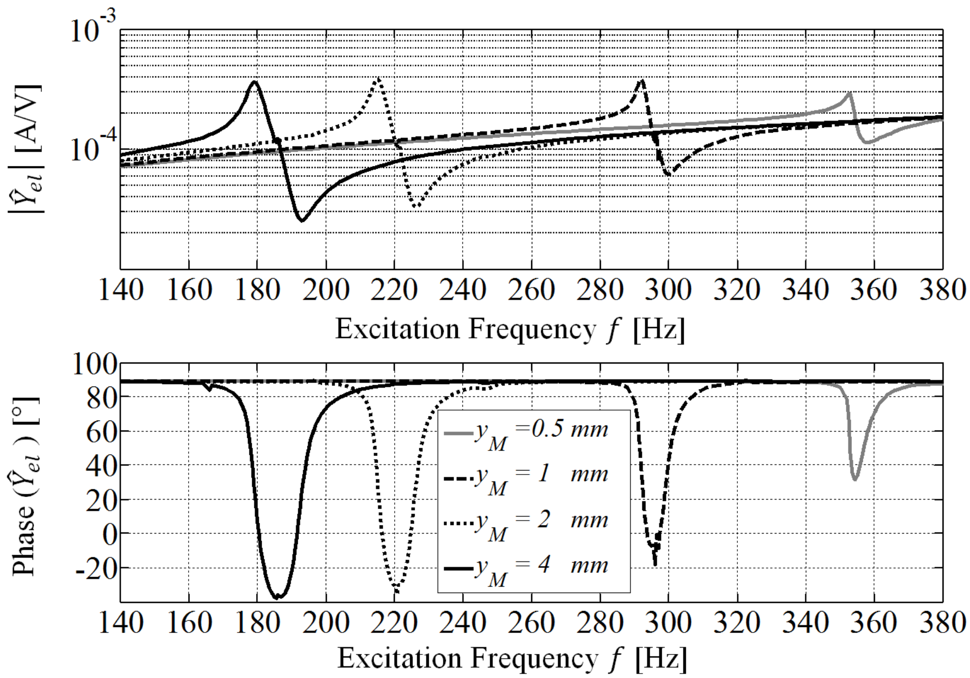

Figure 5-12 Frequency sweeps of the electrical admittance of the harvester

Figure 5-13 shows the identified resonance frequencies with the corresponding separation distances. Additionally, this figure shows the calculated resonance frequency obtained using the model introduced in Section (5.4.2). This figure shows that the calculated results fit the experimental results quite well. At a distance of 1 mm apart, the calculated and the measured resonance frequencies are almost the same. This may be because the magnetic stiffness K_M at this distance is much greater than that structural stiffness of the bimorph K. Within the range of separation distances from 5 mm to 10 mm, the model also displays very good accuracy. The magnetic stiffening within this range has no significant effect on the harvester resonance frequency.

Figure 5-13 also shows that the bimorph resonance frequency can be affected substantially by changing the magnet separation distance. At 1 mm apart, an increase in the resonance frequency of about 71%, as compared to operation at large distances, is obtained. At lower distances, distortions of the measured sweeps are observed. Therefore, no experimental resonance frequencies can be given for distances smaller than 1 mm.

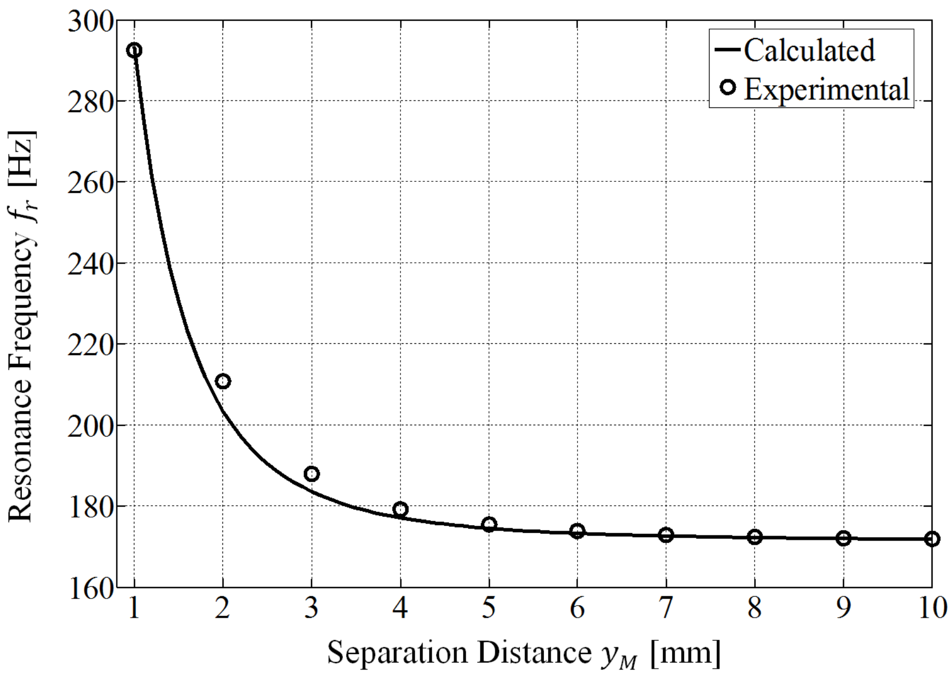

Figure 5-13 Resonance frequency of the piezoelectric harvester

The mechanical quality factor Q_m of the piezoelectric harvester at each distance can be identified by measuring the frequency sweep of the electrical admittance. A typical frequency sweep of a piezoelectric harvester is shown in Figure 5-14.

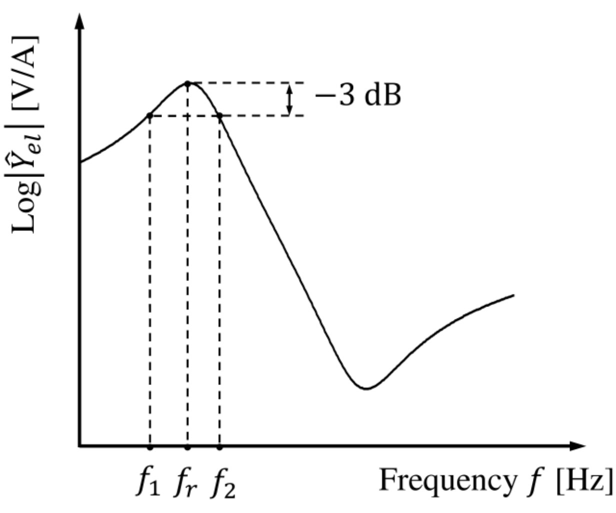

Figure 5-14 Typical frequency sweep of the electrical admittance of a piezoelectric harvester

From Figure 5-14, the mechanical quality factor Q_m can be calculated as [Zickgraf, 1996]

$$Q_m = \frac{f_r}{f_2 - f_1}. \tag{5-27}$$

The damping ratio ζ is related to the mechanical quality factor Q_m and has the following relationship [de Silva, 2000]

$$\zeta = \frac{1}{2Q_m}. \tag{5-28}$$

The identified structural damping ratios with the corresponding magnet separation distances are shown in Figure 5-15. The structural damping ratio decreases with decreasing distance down to 1 mm, meaning that the bimorph experiences larger deflections with decreasing distances. Therefore, the amount of voltage generated can be also increased at those distances down to 1 mm.

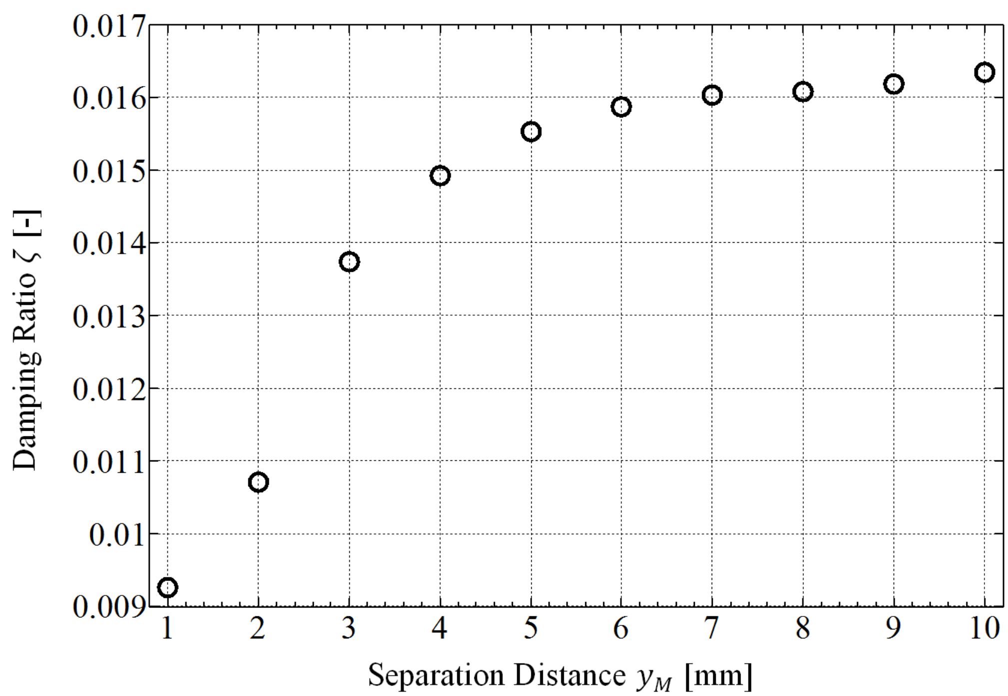

Figure 5-15 Damping ratio versus magnet separation distance

5.5.3 Harvester with Multiple Bimorphs

Magnetic stiffening can be used to design a novel harvester with multiple piezoelectric cantilevers. This harvester is called the “Harvester with Magnetically-Stiffened Cantilevers” (HMSC). It has none of the drawbacks stated previously in Chapter 2: HMSC does not need a special manufacturing process, and it is not sensitive to the effects of manufacturing tolerances for either the piezoelectric elements or the harvester structure. The effect of manufacturing and handling tolerances on the characteristic frequencies is uncritical for this design. The optimal frequency and bandwidth can be readjusted according to the vibration source and tuning scenario used.

An assembled HMSC is shown in Figure 5-16. It consists of three piezoelectric bimorphs (described in Table 3-2). The magnetic stiffening can be individually performed for each bimorph. The bimorphs are electrically isolated from each other and from the base by plastic separator. Magnets with a face area of 8.5 x 2 mm^2 and a thickness of 1.5 mm (from HKCM Engineering, manufacturing code Q08.5x02x01.5Ni48H) were used in the construction. The distance between the two magnets can be adjusted using a knurled screw.

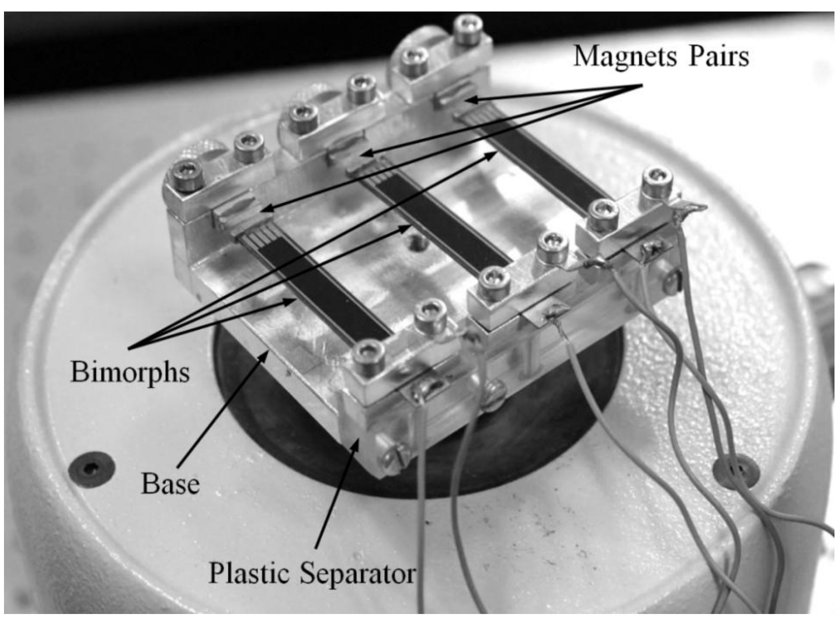

Figure 5-16 Fully assembled Magnetic-Stiffened Cantilever Array (HMSC)

Here, the instruments and setup used in the experimental investigation are similar to those used in Chapter 4. Two piezoelectric harvesters were investigated: a harvester with single piezoelectric bimorph (PB) and a HMSC with three piezoelectric bimorphs (PBs). This HMSC was investigated under different electrical connections and frequency tuning scenarios. In all cases, the harvester was excited with a harmonic acceleration equal to 5.5 $\mathrm{m/s^2}$.

The HMSC was investigated for direct and indirect connections of the piezoelectric bimorphs. In the direct series connection, all of the piezoelectric cantilevers were connected to bridge full-wave rectifiers consisting of four Schottky diodes. Referring to SGS microelectronics [2009], one such diode has a barrier voltage $U_d = 0.49$ V and a bulk resistance $R_d = 1.9\ \Omega$.

The used resistive load is equal to $R_l = 360$ kΩ, which is equivalent to the total impedance of a temperature sensor (Kat. Nr. 30.2018 from TFA Dostmann GmbH). This sensor requires voltage $U_{dc} = 1.5\,\mathrm{V}$ DC (powered originally by battery type LR44). Therefore, the required size of the reservoir capacitor was calculated as $C_R =$ 47 μF. For an indirect connection, three full-wave rectifiers, as stated above, were used. Thus, three reservoir capacitors are also used.

The first part of the experiment is to study the performance of the HMSC when its three bimorphs were connected in direct series or in indirect series. These three bimorphs were tuned all to have the same optimal frequency (250.0 Hz). A comparison between the output DC voltages obtained for the investigated cases is shown in Figure 5-17.

Figure 5-17 shows that the direct series connection of the bimorphs with the same optimal frequency generates the greater DC voltage; this voltage is in fact more than that required for the operation of the temperature sensor. Therefore, this connection can be recommended if the excitation level is too small. For example, the implemented HMSC could be excited with an amplitude of acceleration equal to $1.9\,\mathrm{m/s^2}$ in order to generate the $1.5\,\mathrm{V}$ DC voltage required for the operation of the temperature sensor.

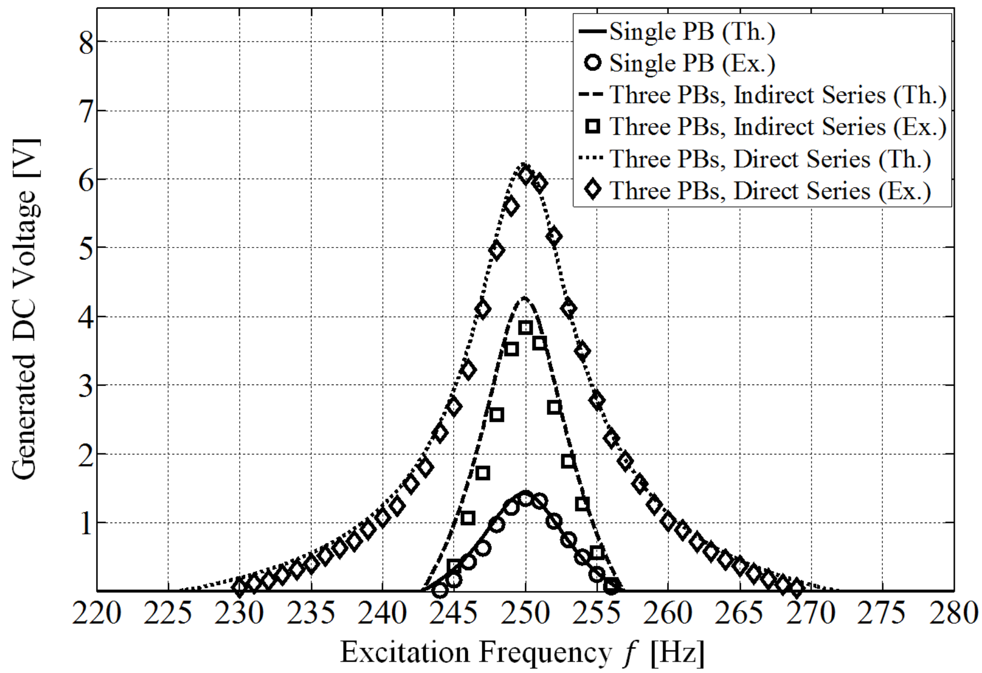

Figure 5-17 Voltage generation of different harvesters, all connected to a resistive load equal to 360 kΩ

The direct series connection is also recommended if it is desirable to minimize the harvester deflection. The HMSC can be adjusted to operate at a frequency other than its optimal frequency, resulting in, considerable reductions in the deflections of the bimorphs. For example an experiment showed that if a harvester with a single bimorph is excited with an acceleration of amplitude equal to $5.5\,\mathrm{m/s^2}$ and the frequency matches its optimal frequency (250 Hz), then the bimorph deflects 95.2 µm in order to generate 1.5 V DC voltage. If a HMSC with three bimorphs is used and is excited with the same acceleration amplitude and at the same frequency, but with each bimorph tuned to either 242.6 Hz or 257 Hz, then each bimorph deflected with amplitude equal to 35.7 µm and the total output DC voltage was also equal to 1.5 V.

The second part of the experiment is to expand the bandwidth of the harvester. Therefore, each bimorph of the HMSC must be tuned to a certain optimal frequency. This frequency is defined according to the tuning scenario used, as introduced previously in Section (5.1.2). Figure 5-18 shows that a single bimorph can generate

1.5 V DC voltage only at a single frequency equal to 250.0 Hz; using three bimorphs extends this single frequency to a considerable range of frequencies.

Using three bimorphs in direct series connection gives a larger range of operational frequencies, but unfortunately the difference in the generated voltage across the range of operational frequencies is larger than that obtained from indirect connection. This difference occurs due to the fact that the generated AC voltage of each bimorph has distinct characteristics (amplitude and phase). Connecting the bimorphs in indirect series offers a considerable enhancement in the harvester bandwidth from 243.0 Hz to 256.0 Hz, with a reasonable difference in the generated DC voltage across the range of excitation frequencies.

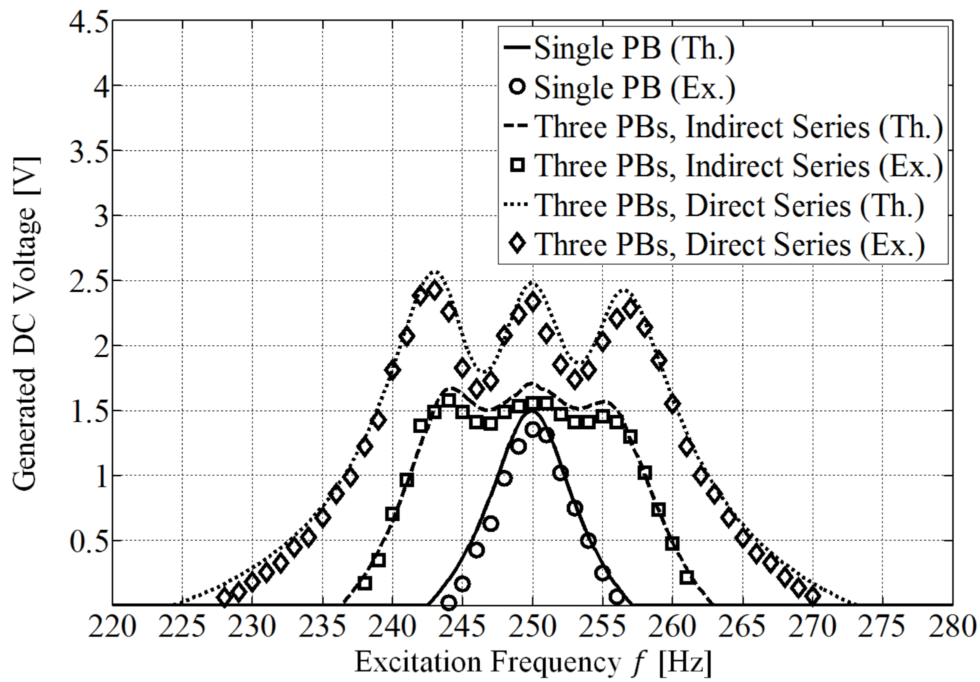

Figure 5-18 Voltage generation of different harvesters, all connected to a resistive load equal to 360 kΩ

6 Summary and Conclusions

Here, the covered topics with the obtained conclusions are reviewed. This chapter contains the conclusions which could be used to improve the performance of the autonomous systems and make them commercially viable.

6.1 Summary

In this section, a summary of the main covered topics is introduced. These topics are: piezoelectric devices, autonomous systems, magnetic stiffening method and harvester with multiple piezoelectric elements.

6.1.1 Piezoelectric Devices

Piezoelectric devices are used in a wide variety of applications nowadays. A better understanding of the influence of material properties and geometric design on the performance of these devices helps to develop piezoelectric devices specifically tailored to their application.

Generally, different equivalent circuits have been introduced in literature to investigate the behavior of piezoelectric devices. The model parameters have typically been identified from measurements. Here, an analytical model for calculating the mechanical and electrical equivalent system parameters and characteristic frequencies based on material properties and geometry was introduced. The model was validated by experimental measurements using a typical harvester containing a piezoelectric bimorph, and fits the experimental results. The model gives a full set of piezoelectric device parameters and is therefore well suited for further theoretical investigations of piezoelectric devices for different applications.

The results showed that even small manufacturing tolerances can have a considerable effect on the system parameters and characteristic frequencies. This may lead to intolerable deviations between desired and actual results, especially in dynamic applications.

6.1.2 Autonomous Systems

Energy harvesting is the process of converting ambient energy into useful electrical energy. For the last decade, the challenge has been to design autonomous systems which fulfill their task and power themselves from available ambient energy. Piezoelectric harvesters have generally received the most attention for their potential to power such systems.

The basic configuration of an autonomous system typically contains three elements in addition to the piezoelectric harvester: a full-wave rectifier, a reservoir capacitor and an electronic device which performs the primary task of the autonomous system, e.g. sensors. Throughout the literature, many publications can be found in which the DC voltage across the electronic device is calculated using different models. All models assume that the piezoelectric harvester is linear and generates a harmonic AC voltage. In real applications, these assumptions can be inaccurate because the harvester is influenced by the rectification process and by the connected capacitor and load.

In this contribution, the operation of a complete autonomous system was analyzed and modeled. The modeled system was also investigated experimentally and a good correlation was found between theoretical and experimental results. In steady-state operation, the piezoelectric harvester experiences two alternating load conditions due to the rectification process: resistive load and open-circuit conditions. These loading conditions can considerably impair the harvester operation. Additionally, they make the system to behave nonlinearly. Furthermore, the results showed that such an autonomous system works efficiently if it is connected to a high impedance load and excited by a frequency matching the anti-resonance frequency of the piezoelectric harvester.

6.1.3 Magnetic Stiffening Method

In chapter 5, the design and testing of a piezoelectric harvester with tunable frequencies was introduced; this tuning is accomplished by changing the attraction force between two permanent magnets by adjusting the distance between the magnets. This method allows the frequencies to be manipulated before and during operation of the harvester. Furthermore, a physical description of the frequency tuning effect was presented. The experimental results achieved using a harvester containing a piezoelectric bimorph fit the calculated results very well. Calculation and experimental results showed that both characteristic frequencies of the harvester can be varied across a wide range: in the experiment, the resonance frequency of the piezoelectric bimorph could be increased by more than 70%.

6.1.4 Harvester with Multiple Piezoelectric Elements

Increasing the generated voltage and expanding the bandwidth of a piezoelectric harvester are two goals that can be achieved by using a harvester with multiple piezoelectric elements.

Magnetic stiffening method was used to design a harvester with multiple piezoelectric elements. The characteristic frequencies of each element can be tuned individually. This harvester does not need a special manufacturing process, and it is not sensitive to the effects of manufacturing tolerances for either the piezoelectric elements or the harvester structure. The optimal frequency and bandwidth can be readjusted according to the vibration source and tuning scenario used. Such harvester was examined both theoretically and experimentally.

The results showed, for example, that a harvester with three piezoelectric bimorphs which all have the same optimal frequency can generate more than four times the DC voltage generated by a harvester with single bimorph when both harvesters are excited with the same acceleration.

In the proposed tuning scenario, two neighboring piezoelectric elements generate the same DC voltage at a certain excitation frequency between their individual optimal frequencies. This voltage is half the voltage generated by a single element excited at its optimal frequency. The harvester with a single piezoelectric bimorph generates sufficient DC voltage (1.5 V) only at a single frequency (250 Hz). Applying the proposed tuning scenario to a harvester including three piezoelectric elements, the bandwidth at which the harvester generates the required voltage was extended to a range of frequencies (243 Hz to 256 Hz).

6.2 Conclusions

The following observations can be taken from the work that is introduced in the previous chapters:

- Manufacturing tolerances of the piezoelectric element have a considerable effect on the electromechanical characteristics of the harvester.
- The derived lumped-parameter model of the piezoelectric harvester gives results with good accuracy, but this accuracy is decreased with increasing the amplitude of the excitation acceleration.
- For energy harvesting applications, studying the piezoelectric harvester without addressing the effect of the other electrical elements of the autonomous system can produce not appropriate results.
- In the steady-state operation of an autonomous system, the piezoelectric harvester experiences two alternating load conditions due to the rectification process. This effect can considerably impair the harvester operation and cause it to behave nonlinearly.
- For autonomous systems, the harvester operates most efficiently when the connected load is of high impedance and the frequency of excitation matches the anti-resonance frequency of the piezoelectric harvester.
- A harvester with magnetic stiffening easy to assemble and can be tuned for a considerable range of frequencies.
- For a typical harvester with magnetic tuning, when the two magnets are very close together, the generated voltage decreases due to the distortion of the mode shape.
- In a range of distances, magnetic stiffening causes increased deflection of the piezoelectric element and thus of the generated voltage.
- Using a harvester with multiple piezoelectric elements is the simplest and most practical solution for expanding the bandwidth and/or increasing the generated voltage.
- For a harvester with multiple piezoelectric elements, the element must be adjusted according to a tuning scenario in order to achieve the required goal.

- The proposed tuning scenario can be used to expand the bandwidth of the harvester into relatively wide range.

References

Alexander C and Sadiku M [2006] Fundamentals of Electric Circuits, 3rd Edition. New York: McGraw Hill.

Badel A, Guyomar D, Lefeuvre E and Richard C [2005] Efficiency Enhancement of a Piezoelectric Energy Harvesting Device in Pulsed Operation by Synchronous Charge Inversion. *Journal of Intelligent Material Systems and Structures* 16: 889–901.

Badel A, Guyomar D, Lefeuvre E and Richard C [2006] Piezoelectric Energy Harvesting Using a Synchronized Switch Technique. *Journal of Intelligent Material Systems and Structures* 17: 831–839.

Beeby S and White N [2010] Energy Harvesting for Autonomous Systems. Norwood: Artech House Inc.

Beer F P and Johnston Jr E R [1992] Mechanics of Materials, 2nd Edition. New York: McGraw-Hill.

Cady W G [1922] The Piezo-electric Resonator. *Proceedings of the Institute of Radio Engineers* 10: 83–114.

Challa V R, Prasad M G and Fisher F T [2011] Towards an Autonomous Self-Tuning Vibration Energy Harvesting Device for Wireless Sensor network Applications. *Smart Mater.* Struct 20: 025004.

Challa V R, Prasad M G, Shi Y, and Fisher F T [2008] A Vibration Energy Harvesting Device with Bidirectional Resonance Frequency Tunability. *Smart Mater. Struct* 17: 015035.

Chen S-N, Wang G-J, and Chien M-C [2006] Analytical Modeling of Piezoelectric Vibration Induced Micro Power Generator. *Mechatronics* 16: 387-397.

Cook-Chennault K A, Thambi N, and Sastry A M [2008] Powering MEMS Portable Devices - A Review of Non-Regenerative and Regenerative Power Supply Systems with Special Emphasis on Piezoelectric Energy Harvesting Systems. *Smart Mater. Struct* 17: 1–33.

Cottone F, Vocca H and Gammaitoni L [2009] Nonlinear Energy Harvesting. *Physical Review Letters* 102: 080601.

de Silva C W [2000] Vibration: Fundamentals and Practice. Boca Raton, Florida: CRC Press LLC.

Do X-D, K Y-H, Nguyen H-H, Le H-B and Lee S-G [2011] An Efficient Parallel SSHI Rectifier for Piezoelectric Energy Scavenging Systems. *International Conference on Advanced Communication Technology (ICACT)*, Feb 13–16, 2011, Gangwon-Do, Korea (South).

du Toit N E, Wardle B L, and Kim S G [2005] Design Considerations for MEMS-Scale Piezoelectric Mechanical Vibration Energy Harvesters. *Integrated Ferroelectrics* 71: 121-160.

Eichhorn C, Tchagsim R, Wilhelm N and Woias P [2011] A Smart and Self-Sufficient Frequency Tunable Vibration Energy Harvester. *J. Micromech. Microeng.* 21: 104003.

Erturk A and Inman D J [2009] Electromechanical Modeling of Cantilevered Piezoelectric Energy Harvesters for Persistent Base Motions. In: Priya S and Inman D (ed.) Energy Harvesting Technologies. New York: Springer, 41-77.

Ferrari M, Ferrari V, Guizzetti M, Marioli D and Taroni A [2008] Piezoelectric Multifrequency Energy Converter for Power Harvesting in Autonomous Microsystems. *Sensors and Actuators A* 142: 329-335.

Guyomar D, Badel A, Lefeuvre E and Richard C [2005] Toward Energy Harvesting Using Active Materials and Conversion Improvement by Nonlinear Processing. *IEEE Transaction on Ultrasonics, Ferroelectrics, and Frequency Control* 52: 584–595.

Hemsel T, Krome J W, Littmann W and Wallaschek J [1998] Modellierung piezoelektrischer Stapel- und Vielschichtaktoren für dynamischen Betrieb. 2. Polnisch-Deutscher Workshop (Werkzeuge der Mechatronik), Mai 14-15, 1998, Ilmenau, Deutschland.

Hu Y, Xue H, and Hu H [2007] A Piezoelectric Power Harvester with Adjustable Frequency through Axial Preloads. *Smart Mater. Struct* 16: 1961-1966.

IEEE [1966] *Standard Definitions and Methods of Measurement for Piezoelectric Vibrators. IEEE 177*. New York: IEEE.

IEEE [1988] *Standard on piezoelectricity. ANSI/IEEE Std 176-198*7. New York: IEEE.

Jaeger R C and Blalock T N [2011] Microelectronic Circuit Design, 4^{th} Edition. New York: McGraw-Hill.

K&J Magnetics [2013] The Original K&J Magnet Calculator. www.kjmagnetics.com/calculator.asp (accessed 2013-02-01).

Karami M and Inman D [2011] Equivalent Damping and Frequency Change for Linear and Nonlinear Hybrid Vibrational Energy Harvesting Systems. *Journal of Sound and Vibration* 330: 5583-5597.

Kim H, Tadesse Y and Priya S [2009] Piezoelectric Energy Harvesting. In: Priya S and Inman D (ed.) Energy Harvesting Technologies. New York: Springer, 41-77.

Lallart M and Guyomar D [2008] An Optimized self-Power Switching Circuit for Non-Linear Energy Harvesting with Low Voltage Output. *Smart Mater. Struct* 17: 035030.

Lallart M, Anton S R and Inmann D J [2010] Frequency Self-Tuning Scheme for Broadband Vibration Energy Harvesting. *Journal of Intelligent Material Systems and Structures* 21: 897–906.

Lee S, D Youn B, and C Jung B [2009] Robust Segment-Type Energy Harvester and Its Application to a Wireless sensor. *Smart Materials and Structures* 18: 095021.

Lefeuvre E, Badel A, Richard C and Guyomar D [2005] Piezoelectric Energy Harvesting Device Optimization by Synchronous Electric Charge Extraction. *Journal of Intelligent Material Systems and Structures* 16: 865–876.

Lefeuvre E, Badel A, Richard C, Petit L and Guyomar D [2006] A Comparison between Several Vibration-Powered Piezoelectric Generators for Standalone Systems. *Sensors and Actuators A* 126: 405-416.

Leland E S and Wright W K [2006] Resonance Tuning of Piezoelectric Vibration Energy Scavenging Generators Using Compressive Axial Preload. *Smart Mater. Struct* 15: 1413-1420.

Lenk A [1975] Elektromechanische Systeme, Band 1: Systeme mit konzentrierten Parametern. Berlin: VEB Verlag Technik.

Lesieutre G A and Davis C L [1997] Can a Coupling Coefficient of a Piezoelectric Actuator Be Higher Than those of Its Active Material?. *Journal of Intelligent Material Systems and Structures* 8: 859-867.

Liang J and Liao W-H [2012] Improvement Design and Analysis of Self-Powered Synchronized Switch Interface Circuit for Piezoelectric Energy Harvesting Systems. *IEEE Transaction on Industrial Electronics* 59(4): 1950-1960.

Lien I and Shu Y [2012] Array of Piezoelectric Energy Harvesting by the Equivalent Impedance Approach. *Smart Mater. Struct*. 21: 082001.

Lin J H, Wu X M, Ren T L, and Liu L T [2007] Modeling and Simulation of Piezoelectric MEMS Energy Harvesting Device. *Integrated Ferroelectrics* 95: 128–141.

Liu J, Fang H, Xu Z, Mao X, Shen X, Chen D, Liao H and Cai B [2008] A MEMS-Based Piezoelectric Power Generator Array for Vibration Energy Harvesting. *Microelectronics Journal* 39: 802-806.

Lu F, Lee H, and Lim S [2004] Modeling and Analysis of Micro Piezoelectric Power Generators for Micro-Electromechanical-Systems Applications. *Smart Mater. Struct* 13: 57–63.

Magnet Sales & Manufacturing Inc. [2000] Permanent magnet design guide. www.magnetsales.com/Design/DesignG.htm [accessed 2011-06-27].

Makihara K, Onoda J and Miyakawa T [2006] Low Energy Dissipation Electric Circuit for Energy Harvesting. *Smart Mater. Struct*. 15: 1493–1498.

Mason W P [1935] An Electromechanical Representation of a Piezoelectric Crystal Used as a Transducer. *Proceedings of the Institute of Radio Engineers* 23(10): 1252–1263.

Morgan Electro Ceramics [2007] Piezoelectric Ceramics–Electro Ceramic Solutions. www.morganelectroceramics.com/resources/literature (accessed 2011-03-28).

Morgan Electro Ceramics [2009] Guide to Piezoelectric & Dielectric Ceramic. www.morganelectroceramics.com/resources/guide-to-piezoelectric-dielectric-ceramic (accessed 2011-03-25).

Münch I, Krauß M, Wagner W and Kamlah M [2012] Ferroelectric Nanogenerator Coupled to an Electric Circuit for Energy Harvesting. *Smart Mater. Struct*. 21: 115026.

Neubauer M, Krack M, and Wallaschek J [2009] Parametric Studies on the Harvested Energy of Piezoelectric Switching Techniques. *Smart Mater. Struct* 19(2): 025001.

Ó Mathúna C, O' Donnell T, Martinez-Catala R, Rohan J and O' Flynn B [2008] Energy Scavenging for Long-Term Deployable Wireless Sensor Network. *Talanta* 33: 613-623.

Ottman G K, Hofmann H F, Bhatt A C and Lesieutre G A [2002] Adaptive Piezoelectric Energy Harvesting Circuit for Wireless Remote Power Supply. *IEEE Trans. Power Electron.*17: 669–76.

Priya S [2007] Advances in Energy Harvesting Using Low Profile Piezoelectric Transducers. *J. Electroceramics* 19: 165-182.

Rabaey J M, Ammer M J, da Silva Jr J L, Patel D and Roundy S [2000] PicoRadio Supports Ad Hoc Ultra-Low Power Wireless Networking. *Computer* 33:42-48.

Reilly E K, Burghardt F, Fain R, and Wright P [2011] Powering a Wireless Sensor Node with a Vibration-Driven Piezoelectric Energy Harvester. *Smart Materials and Structures* 20: 125006.

Richter B, Twiefel J, Hemsel T and Wallaschek J [2006] Model Based Design of Piezoelectric Generators Utilizing Geometrical and Material Properties. *ASME International Mechanical Engineering Congress and Exposition*, November 05-10, 2006, Chicago, Illinois, USA.

Richter B, Twiefel J and Wallaschek J [2009] Piezoelectric Equivalent Circuit Models. In: Priya S and Inman D (ed.) Energy Harvesting Technologies. New York: Springer, 79-104.

Richter B [2010] Modellbasierter Entwurf resonant betriebener, piezoelektrischer Biegeschwinger in Energy Harvesting Generatoren. Aachen: Shaker Verlag.

Roundy S, Wright P K, and Rabaey J [2003] A study of Low Level Vibrations as a Power Source for Wireless Sensor Nodes. *Computer Communications* 26: 1131–114.

SGS Thomson Microelectronics [1999] Datasheet of Schottky Diodes 1N5711. www.datasheetcatalog.org/datasheet/SGSThomsonMicroelectronics/mXtwxqw.pdf (accessed 2013-02-25).

Shahruz S M [2006] Design of Mechanical Band-Pass Filters for Energy Scavenging. *J. Sound and Vibration* 292: 987-998.

Shu Y and Lien I [2009] Performance Evaluation of Vibration-Based Piezoelectric Energy Scavengers. In: Priya S and Inman D (ed.) Energy Harvesting Technologies. New York: Springer, 79-104.

Sodano H A, Park G, and Inman D J [2004] Estimation of Electric Charge Output for Piezoelectric Energy Harvesting. *Strain* 40: 49–58.

Stanton S C, McGehee C C, and Mann B P [2010] Nonlinear Dynamics for Broadband Energy Harvesting: Investigation of a Bistable Piezoelectric Inertial Generator. *Physica D* 239: 640-653.

Tang L, Yang Y and Soh C K [2010] Toward Broadband Vibration-Based Energy Harvesting. *J. Intelligent Material Systems and Structures* 21: 1867-1896.

Tichý J, Erhart J, Kittinger E and Prívratská [2010] Fundamentals of Piezoelectric Sensorics: Mechanical, Dielectric, and Thermodynamical Properties of Piezoelectric Materials. Springer-Verlag.

Timoshenko S [1937] Vibration Problems In Engineering. New York: D Van Nostrand Company, Inc.

Twiefel J, Richter B, Sattel T and Wallaschek J [2007] Power Output Estimation and Experimental Validation for Piezoelectric Energy Harvesting Systems. *Electroceramics* 20 (3-4): 203-208.

van Dyke K S [1925] The Electric Network Equivalents of a Piezoelectric Resonator. *Physical Review* 25: 895.

Wang Q and Cross L [1998] Performance Analysis of Piezoelectric Cantilever Bending actuators. *Ferroelectrics* 215: 187-213.

Williams C B and Yates R B [1996] Analysis of a micro-electric generator for microsystems. *Sensors and Actuators* A 52: 8-11.

Xue H, Hu Y and Wang Q [2008] Broadband Piezoelectric Energy Harvesting Devices Using Multiple Bimorphs with Different Operating Frequencies. *IEEE Transactions on Ultrasonics, Ferroelectrics and Frequency Control* 55: 2104-2108.

Zhu D, Roberts S, Tudor M J, and Beeby S P [2010a] Strategies for increasing the operating frequency range of vibration energy harvesters: a review. *Measurement*

Science and Technology 21: 022001.

Zhu D, Roberts S, Tudor M J, and Beeby S P [2010b] Design and Experimental Characterization of a Tuneable Vibration-Based Electromagnetic Micro-Generator. *Sensors and Actuators A* 158: 284-293.

Zickgraf B [1996] Ermüdungsverhalten von Multilayer-Aktoren aus Piezokeramik. *Fortschritt-Berichte VDI, Reihe 18,* Nr. 191. Düsseldorf: VDI Verlag GmbH.

Appendix A: Curriculum Vitae

Name	:	Waleed Al-Ashtari
Date of Birth	:	25^{th} October 1979
Place of Birth	:	Baghdad, Iraq
1994 - 1997	:	Baccalaureate Student, Secondary School, Baghdad, Iraq Degree: Baccalaureate
1997 - 2000	:	B.Sc. Student Mechanical Engineering, College of Engineering, Al-Nahrain University, Iraq Degree: Bachelor of Science in Mechanical Engineering
2002 - 2003	:	M.Sc. Student (Applied Mechanics) Mechanical Engineering, College of Engineering, Al-Nahrain University, Iraq Degree: Master of Science in Mechanical Engineering
2003 - 2006	:	Senior Engineer Al-Itkan/Siemens agent in Iraq
Since 2006	:	Faculty Member Mechanical Engineering Department, College of Engineering, University of Baghdad, Iraq
Since 2009	:	Scholarship holder (DAAD/MoHESR Scholarship Program) for getting a Doctorate in Engineering, working at the chair of Mechatronics and Dynamics, Faculty of Mechanical Engineering, University of Paderborn, Germany